Kaunas University of Technology

Faculty of Mechanical Engineering and Design

The Development of Integral Unified Flight Dynamics Model for a Thrust-Vectoring VTOL Aircraft

Master's Final Degree Project

Carlos Sosa Henríquez

Project author

Assoc. Prof. Dr. Saulius Japertas

Supervisor

Kaunas, 2024

Kaunas University of Technology
Faculty of Mechanical Engineering and Design

The Development of Integral Unified Flight Dynamics Model for a Thrust-Vectoring VTOL Aircraft

Masters's Final Degree Project

Aeronautical Engineering (6211EX024)

Carlos Sosa Henríquez
Project author

Assoc. Prof. Dr. Saulius Japertas
Supervisor

Assoc. Prof. Linas Paukštaitis
Reviewer

Kaunas, 2024

Kaunas University of Technology

Faculty of Mechanical Engineering and Design

Carlos Sosa Henríquez

The Development of Integral Unified Flight Dynamics Model for a Thrust-Vectoring VTOL Aircraft

Declaration of Academic Integrity

I confirm the following:

1. I have prepared the final degree project independently and honestly without any violations of the copyrights or other rights of others, following the provisions of the Law on Copyrights and Related Rights of the Republic of Lithuania, the Regulations on the Management and Transfer of Intellectual Property of Kaunas University of Technology (hereinafter – University) and the ethical requirements stipulated by the Code of Academic Ethics of the University;

2. All the data and research results provided in the final degree project are correct and obtained legally; none of the parts of this project are plagiarised from any printed or electronic sources; all the quotations and references provided in the text of the final degree project are indicated in the list of references;
I have not paid anyone any monetary funds for the final degree project or the parts thereof unless required by the law;

3. I understand that in the case of any discovery of the fact of dishonesty or violation of any rights of others, the academic penalties will be imposed on me under the procedure applied at the University; I will be expelled from the University and my final degree project can be submitted to the Office of the Ombudsperson for Academic Ethics and Procedures in the examination of a possible violation of academic ethics.

Carlos Sosa Henríquez

Confirmed electronically

Kaunas University of Technology

Faculty of Mechanical Engineering and Design

Task of the Master's Final Degree Project

Given to the student – Carlos Sosa Henríquez

1. Topic of the project

The Development of Integral Unified Flight Dynamics Model for a Thrust-Vectoring VTOL Aircraft

(In English)

Integruoto vieningo skrydžio dinamikos modelio sukūrimas VTOL orlaiviui su traukos valdymu

(In Lithuanian)

2. Aim and tasks of the project

Aim: To develop an integral unified flight dynamic model for advance proprotor aircraft

Tasks:

1. To analyze the flight dynamics and controls algorithms of tilt-wing, tilt-rotor, and relevant thrust vectoring aircraft configurations

2. To develop, evaluate, and validate an analytical-numerical-based algorithm for the performance analysis of proprotors, with allowance for large inflow angles

3. To integrate the results of the proprotor performance algorithm into a longitudinal rigid-body flight dynamic model at various flight conditions and validate it against experimental data

4. To develop an optimization control system for proprotor trimming at the most aerodynamic-efficiency setting or maximum thrust capabilities at various flight conditions by variations in the RPM and collective or feathering

5. To integrate the developed optimization control system into the longitudinal flight dynamic model and evaluate the optimized trimming settings with respect to experimental data at the OEM configuration

3. Main requirements and conditions

1. To conduct a comprehensive analytic of proprotor thrust vectoring aircraft configurations by literature review and understanding of the research and industry standards

2. To develop an analytical-numerical algorithm for proprotor performance, allowing large inflow angles and validating it against other modeling approaches and experimental data

3. To integrate the results of the proprotor performance algorithm into a longitudinal rigid-body flight dynamic model, covering various flight conditions and validating against experimental data

4. To develop an optimization control system for proprotor trimming, optimizing settings for maximum aerodynamic efficiency or maximum thrust capabilities at various flight conditions through RPM and collective or feathering adjustments

5. To integrate the optimization control system into the longitudinal flight dynamic model and evaluate the optimized trimming settings against reference OEM experimental configurations

4. Additional requirements and conditions for the project, report, and appendices

"Not applicable"

Project author	Carlos, Sosa Henríquez		2023-02-15
	(Name, Surname)	*(Signature)*	*(Date)*
Supervisor	Assoc. Prof. Saulius Japertas		
	(Name, Surname)	*(Signature)*	*(Date)*
Head of study field programs	Prof. Artūras Keršys		
	(Name, Surname)	*(Signature)*	*(Date)*

Sosa Henríquez, Carlos. The Development of Integral Unified Flight Dynamics Model for a Thrust-Vectoring VTOL Aircraft. Master's Final Degree Project / supervisor Assoc. Prof. Saulius Japertas; Faculty of Mechanical Engineering and Design, Kaunas University of Technology.

Study field and area: Aeronautical Engineering (E14), Engineering Science.

Keywords: aircraft, performance, handling qualities, proprotor, flight dynamic model

Kaunas, 2024. 87 p.

Summary

In the evolving landscape of proprotor aircraft, especially those equipped with thrust vectoring capabilities, a transformative shift in performance and stability analysis is underway. This project focuses on developing performance analytical and numerical algorithms and introducing novel methodologies to reassess the potential and limitations of these modeling approaches against conventional ones. The central issue addressed is the standard limitation in analytical-numerical proprotor performance models, which traditionally assume small inflow angles. The project's innovation lies in developing a generic and validated tool that transcends these limitations, accommodating large inflow angles and paving the way for more accurate modeling.

The project's primary objective is to advance the understanding and application of proprotor performance modeling and control systems, developing an integral unified flight dynamic model for advanced proprotor aircraft. The project unfolds through multiple sections, starting with a literature review of current modeling approaches and aircraft configurations. The following sections detail the architecture, scope, and analysis capabilities of an analytical-numerical algorithm for proprotor performance analysis with allowance for large inflow angles. This algorithm's results are then integrated into a comprehensive longitudinal rigid-body flight dynamic model, validated against experimental data, and optimized for trimming at the most aerodynamic-efficient setting. The developed proprotor optimization control system couples the RPM and collective feeding through a single input. The input proposed to be used by the algorithm or pilots in manned operations is referred to as the Power Control Stick (PCS). The control system is integrated into the longitudinal flight dynamic model, and the overall performance is evaluated against experimental data.

The proposed proprotor algorithm demonstrates a significant potential improvement over conventional low-to-medium computation cost approaches, leading to remarkable error margins between -3 and 4% for the variation of power consumed versus thrust obtained. The increased accuracy enables using analytical-numerical methods in proprotor-equipped aircraft until the fine-tuning development phases are completed. This results in lower computational costs and the ease of implementing optimization cycles compared to established high computational cost approaches such as Computational Fluid Dynamics (CFD). This undertaking challenges established paradigms and establishes the groundwork for thoroughly reevaluating the methodologies employed in the analysis of proprotors' performance.

Integrating the proprotor performance results into the longitudinal flight dynamic model yields error margins between 1.6% and 2.8% for hovering scenarios and 0.9% to 1.4% for the maximum speed scenarios at various pressure altitudes. Challenges arise in modeling the proprotor wake interference

in hovering scenarios, particularly for tiltrotor configurations. The longitudinal flight dynamic model results are presented regarding the leading aircraft trimming parameters, stability analysis, and overall performance indicators such as the maximum speeds, ceiling, and Rate of Climb (ROC).

The optimized PCS control system is designed to trim RPM and collective or feathering for maximum aerodynamic efficiency or to maximize the thrust capabilities limited by the powerplant characteristics. Comparisons with the Bell XV-15's original flight test data showcase improvements of approximately 7-8% and 2-7% for power minimization configurations in hovering and maximum speed scenarios, respectively. Configurations maximizing thrust achieve an average payload increase of 220 kg and a velocity increase of 2 m/s for hovering and maximum speed scenarios. Further exploration is recommended to assess the system's robustness and potential adaptability to varying proprotor configurations. Continued validation is crucial to solidify the practical applicability of these advancements within the broader spectrum of proprotor aircraft development.

Sosa Henríquez, Carlos. Integruoto vieningo skrydžio dinamikos modelio sukūrimas VTOL orlaiviui su traukos valdymu. Magistro baigiamasis projektas / vadovas Doc. Saulius Japertas; Kauno technologijos universitetas, Mechanikos inžinerijos ir dizaino fakultetas.

Studijų kryptis ir sritis: Aeronautikos inžinerija (E14), Inžinerijos mokslai.

Reikšminiai žodžiai: orlaivis, skrydžio charakteristikos, valdymo charakteristikos, proprotorius, skrydžio dinaminis modelis.

Kaunas, 2024. 87 p.

Santrauka

Proprotorių tyrimai, susiję su šių orlaivių naudojimu, valdymu ir stabilumu tampa vis labiau svarbūs. Šie tyrimai bus ypač svarbūs orlaiviuose, kuriuose įdiegtos traukos krypties valdymo sistemos. Šiame darbe aptariami analitiniai ir skaitiniai metodai, pristatant naujus proprotoriaus skaičiavimo metodus. Analizuojami šių metodų privalumai ir trūkumai, lyginant juos su tradiciniais metodais. Pateiktas metodas sprendžia pagrindinę klasikinio metodo problemą, kai srauto įtekėjimo kampai yra laikomi mažais. Darbe pristatomas ir patikrinamas bendrinis metodo algoritmas, kuris įvertina galimus didelius srauto įtekėjimo kampus, taip pagerinant skaičiavimo tikslumą.

Pagrindinis projekto tikslas yra tobulinti metodų taikymą ir efektyvumą proprotoriaus veikimo modeliavimo bei valdymo sistemose, sukuriant vieningą skrydžio valdymo dinaminį modelį. Darbo pradžioje aprašomi dabartinių modeliavimo metodų ir orlaivių konfigūracijos. Tolesniuose skyriuose išsamiai aprašoma analitinio - skaitinio algoritmo, skirto proprotoriaus veikimo analizei, architektūra, kryptis ir analizės galimybės, atsižvelgiant į didelius srauto įtekėjimo kampus. Tada šio algoritmo rezultatai integruojami į išilginį standaus kūno skrydžio dinaminį modelį, patvirtintą pagal esamus eksperimentinius duomenis. Sukurta proprotoriaus valdymo sistema apjungia apsukų ir pokrypio automato valdymą. Valdymo sistema integruojama į išilginio skrydžio dinaminį modelį, o modelio veikimas yra patikrinamas su eksperimentiniais duomenimis.

Pateiktas proprotoriaus skaičiavimo algoritmas yra tikslesnis nei įprastiniai metodai: apskaičiuotos galios priklausomybės nuo traukos paklaidos svyruoja nuo -3 iki 4%. Tai leidžia jau projektavimo pradžioje naudoti didesnio tikslumo analitinius-skaitinius metodus, kurie nereikalauja ženkliai didesnių skaičiavimo resursų lyginant su skaičiuojamosios fluidų dinamikos (CFD) metodais. Tai lemia mažesnes skaičiavimo sąnaudas, bei lengvesnį ir paprastesnį optimizavimą.

Integravus proprotoriaus skaičiavimo metodiką į išilginio skrydžio dinaminį modelį, gautos paklaidos svyruoja nuo 1,6% iki 2,8% kabėjimo režime ir nuo 0,9% iki 1,4% didžiausio skrydžio greičio režime, įvairiuose skrydžio aukščiuose. Iššūkių kyla modeliuojant proprotoriaus valktį kabėjimo režime, ypač naudojant pasukamo rotoriaus sistemą. Pateikiami dinaminio modelio rezultatai, susiję su orlaivio pagrindiniais reguliavimo parametrais, stabilumo analize ir bendrais veikimo rodikliais, įskaitant maksimalų greitį, skrydžio lubas ir kilimo spartą.

Optimizuota valdymo sistema sukurta siekiant pagerinti aerodinaminį efektyvumą, kartu reguliuojant rotoriaus apsukas ir rotoriaus žingsnį pokrypio automatu. Atlikus palyginamąją analizę su eksperimentiniais duomenimis iš orlaivio Bell XV-15 skrydžio bandymų, optimizavus energijos sąnaudos kabėjimo režime jos sumažėjo 7–8 %, o maksimalaus skrydžio režimu – 2–7 %.

Konfigūracijos, kuriomis maksimaliai padidinama trauka, leidžia pasiekti vidutinį naudingosios apkrovos padidėjimą 220 kg, o skrydžio greitį padidinti 2 m/s. Norint įvertinti sistemos patvarumą ir galimybę prisitaikyti prie įvairių proprotorių konfigūracijų, būtina atlikti išsamesnį tyrimą. Papildomi empiriniai bandymai yra itin svarbūs siekiant patikrinti sistemos veikimą ir užtikrinti praktinį pritaikomumą platesniame proprotorinių orlaivių kūrimo kontekste.

Table of contents

List of figures

List of tables

List of abbreviations and terms

ASD: Aircraft Specific Data

BET: Blade Element Theory

BEMT: Blade Element Momentum Theory

CFD: Computational Fluid Dynamics

CLAWS: Flight Control Laws

CP: Power Coefficient

CT: Thrust Coefficient

CVT: Continuously Variable Transmission

DOF: Degree of Freedom

DSRA: RPM in Dual Speed RGB for Airplane Mode

DSRH: RPM in Dual Speed RGB for Helicopter Mode

FADEC: Full Authority Digital Engine Control

FM: Figure of Merit

FCS: Flight Control System

FPT: Free Power Turbine

FVW: Free Vortex Wake

GPR: Gaussian Process Regression

IMC: Instrumental Meteorological Conditions

MITL: Man in the Loop

OEM: Original Equipment Manufacturer

PCS: Power Control Stick

PDD: Probability Density Distribution

ROC: Rate of Climb

RPM: Revolutions Per Minute

RGB: Reduction Gear Box

SFC: Specific Fuel Consumption

STOL: Short Take off and Landing

TMM: Turbo Machine Module

UAM: Urban Air Mobility

VFE: Maximum Extended Flaps Speed

VTOL: Vertical Take off and Landing

VS1G: Stall Speed at 1G

Introduction

Aircraft configurations, such as those with thrust vectoring capabilities and generally proprotors, have been evolving their design and optimization assessment, with traditional assumptions reassessed and novel methodologies emerging. This project aims to reevaluate the potential and limitations of analytical and numerical modeling and control systems by developing a generic and validated tool that can be adapted to any aircraft of this category.

The literature review of §1 discusses about the appearance that there are multiple topics in the frame of proprotor aircraft that have not been modeled, analyzed, and validated. The primary research opportunities are categorized as:

- Analytical-numerical methods for proprotor performance models are often constrained by the assumptions of small inflow angles. This presents a unique opportunity to develop a model allowing large inflow angles, which can be compared against the conventional small-angle assumption and experimental data. It is considered that the most promising results of this new methodology might be encountered when validating the performance of blades that have significant pitch differences throughout the span.
- Another research opportunity on proprotor trimming optimization has been found, precisely adjusting RPM and collective/feathering settings for maximum aerodynamic efficiency or thrust capabilities. Similar studies to this approach have focused on trimming the powerplant itself rather than on the proprotor. Addressing this gap could lead to the development of the proposed Power Control Stick (PCS) system, enabling dynamic optimization and potentially improving propulsion efficiency.
- A notable research opportunity involves integrating the results of the optimized proprotor model into an analytical-numerical flight dynamic model, circumventing the common reliance on private models found in current literature. The scarcity of studies validating results against flight test data further emphasizes the need for developing an in-house numerical low-to-medium computational cost flight dynamic structure.

Analytical-numerical proprotor analysis methods are commonly limited by the assumptions of small inflow angles, which demonstrate a potential that exceeds common assumptions. This departure presents an opportunity to significantly improve the modeling accuracy, offering a shift towards low-to-medium computational cost tools in the development process of proprotors. The implications of these advancements extend to lower computational costs and a more simplified geometrical definition of proprotors compared to established theories such as the Free Vortex Method (FVM) or Computational Fluid Dynamics (CFD).

This project aims to develop an integral unified flight dynamic model for advanced proprotor aircraft. The tasks that are accomplished through the multiple sections of the project to satisfy the aim are:

1. To analyse the flight dynamics and controls algorithms of tilt-wing, tilt-rotor, and relevant thrust vectoring aircraft configurations.
2. To develop, evaluate, and validate an analytical-numerical-based algorithm for the performance analysis of proprotors, with allowance for large inflow angles.
3. To integrate the results of the proprotor performance algorithm into a longitudinal rigid-body flight dynamic model at various flight conditions and validate the model against experimental data.

4. To develop an optimization control system for proprotor trimming at the most aerodynamic-efficiency setting or maximum thrust capabilities at various flight conditions by variations in the RPM and collective or feathering.
5. To integrate the developed optimization control system into the longitudinal flight dynamic model and evaluate the optimized trimming settings with respect to experimental data at the OEM configuration.

The main focus is to advance the understanding and application of proprotor performance modeling and control systems, which are then integrated into an aircraft-level longitudinal flight dynamic model. The performed tasks include the development of the analytical-numerical proprotor performance tool with an allowance for large inflow angles, the development of algorithms that ease the validation of the results against experimental data, the development of an algorithm to analyze in-depth the results between different theories, and at different operating condition, construction of a generic longitudinal flight dynamic model based on a solid-rigid body, the integration of proprotor performance results into the flight dynamic model, in-depth analysis of its influence on overall aircraft performance, and the development and evaluation of an optimized control system, which has been referred as the Power Control Stick (PCS), to streamline proprotor controls and reduce pilot workload.

The integration of proprotor performance data into a comprehensive longitudinal flight dynamic model involves careful consideration of aerodynamic coefficients for the main aerodynamic aircraft surfaces, powerplant modules that fed the system from the available power at each flight condition, interactions of the proprotor wake with the aircraft and its effects on performance, and the aircraft geometrical definitions for assessing the transference of forces and moments along the aircraft body. Using recent methodologies and challenging established norms, this research project aims to redefine the landscape of performance, stability, and control systems assessment of proprotorcrafts, with the particular implementation of thrust vectoring capabilities.

1. Literature Review

1.1. Advanced Rotorcraft Features Examination

1.1.1. Preface

The aviation industry has witnessed remarkable advancements, leading to the development of various types of aircraft tailored to specific operational requirements. Vertical Takeoff and Landing (VTOL) and Short Takeoff and Landing (STOL) have shown superior performance results among these types. The main attractiveness of these aircraft types is the reduced size of runways compared to conventional Horizontal Takeoff and Landing (HTOL) aircraft and the increase in range, speed, and payload capabilities compared to conventional helicopters. This study emphasizes VTOL aircraft, which might be used as well under STOL scenarios, depending on the aircraft performance limitations, such as substantially high TOWs [1], high-pressure altitudes, or derated takeoff procedures, which can increase the lifespan of the propulsion systems and structural components [2].

In the literature, there are different ways to characterize VTOL aircraft. While some authors prefer to differentiate these in terms of the rotor type used (mono-rotor, multi-rotor, Coanda-effect, etc.) [3], other authors differentiate the categories more towards degrees of freedom, distribution, and mechanisms of the aerodynamic and propulsion systems [4]. Following the second philosophy of characterization and adapting it to the frame of work of this study, VTOL aircraft is defined in the following sections. Attending to the similarities in some of the definitions, it is worth mentioning that the concept of thrust-vectoring might be used in a future section of this project to refer to tilting rotors and tilting-wing mechanisms as actually inducing a change in the thrust vector direction.

Current advanced rotorcraft configurations tend to couple different conventional design configurations such as tilting-rotors, tilting-wings, and distributed propulsion mechanisms. Some aircraft configurations show considerable changes in the inertial matrix during operation and even asymmetrical mass properties around the X-Y-body (lateral) plane due to, for example, independent tilting of the wing or rotors in one of the lateral sides. Moreover, hybrid and electric propulsion units are experiencing a surge in demand, especially in short-range operations, which introduces the possibility of changing the power rating of each engine faster than with combustion engines. These observations lead to the need to develop modular flight dynamic models that can adapt to different aircraft configurations from structural, aerodynamic, and propulsive domains. The different design configurations are further explained in the following subsections.

1.1.2. Definition of Generic Configurations

The term proprotor system is designated because it aims to operate as rotors during VTOL mode, transforming into propellers when the aircraft is in airplane mode. The rotors change their orientation, usually with the engine nacelle, to change between helicopter and airplane mode, while the fuselage and the wing stay as per a conventional airplane. Later sections of this project discuss the most well-known tilt-rotor aircraft and their properties.

The tilting of the rotor/nacelle can be performed with relatively good maneuverability [5] inside the conversion corridor, which tends to be more flexible than tilting wings [6]. The standard side-by-

side rotor distribution partially avoids the aerodynamic interference phenomena found in other configurations, such as the tandem. Additionally, this rotor configuration may benefit in forward flight from an apparent doubling of the blade aspect ratio [7]. Typical helicopter blade twists are on the order of 10°, while propeller blades are in the order of 60º or more at the root. Hence, prop-rotor twists compromise the ability to hover and fly at high speeds in airplane mode.

Among the primary disadvantages of tiltrotors is the dynamic interplay between the rotor wake and the wing surface, mainly at the hovering and even transition phases. This phenomenon results in downward forces, turbulent airflow separation over the lifting surfaces, and vibrations [8]. Consequently, the downforce is alleviated during operations by deflecting the surrounding control surfaces downwards [5] (usually flaperons), partially reducing the wing's exposure to the rotor wake. Extensive research has been focused on quantifying these parameters experimentally on wind tunnels but presents a great tendency to use CFD simulations [9]. Flight testing research significantly contributes during the tuning of highly complex ground effect models, which might surpass the practical capabilities of simulated analysis.

Posterior to the first successful tilting-rotor projects, the tilting-wings aircraft were considered as an alternative solution in which the whole wing rotates instead of just the engine nacelle. The tilt-wing concept was first tested in the Boeing Vertol VZ-2 and later with the Bell X-22 with successful results [12], even though the project was canceled later.

Considering that the downwash of the rotors lies parallel to the main chord line of the wing, the control surfaces can still be used during hover and early transition phases [9], which is an advantage against the tilt-rotors. Additionally, the fixed position of the engines' nacelles with respect to the attachment to the wing leads to more streamlined and aerodynamic efficient structures.

On the other hand, the large exposed surface area of the wing during the hovering and transitions, as per in tail-sitters, generates accentuated forces when wind gusts are present, potentially leading to significant instabilities and increased power consumption [10].

Fig. 1. Bell V-247 rendered model [13]

Nowadays, tilting wings are evaluated as the most prominent architecture for distributed propulsion aircraft, such as the Lilium Jet with Ducted Electric Vectored Thrust (DEVT) for UAM operations [11]. Combinations of tilting-rotor/wings have been proposed recently with projects such as the Bell V-247, represented in Fig. 1, where the wing section from rotors to the wingtip tilts with the engine nacelle. In contrast, the inwards section remains fixed with respect to the fuselage. In contrast, the

inwards section of the wing does not rotate with respect to the fuselage, thus alleviating the rotation mechanism from the bending moments generated by the lift forces.

Alternatively to the conventional wing-tilting around the span-wise direction, promising proposals such as the "Transwing" from Pterodynamics intend to decrease the excessive exposure of the wing to wind gusts by adopting a dihedral motion of the wing, as represented in Fig. 2.

Observing recently officially published videos from flight testing [12] – exactly not the same model as represented here - the aircraft shows some "herky-jerky motion" during the transition phase, which might be smoothened during the development of its flight controls, aerodynamics, and folding mechanism.

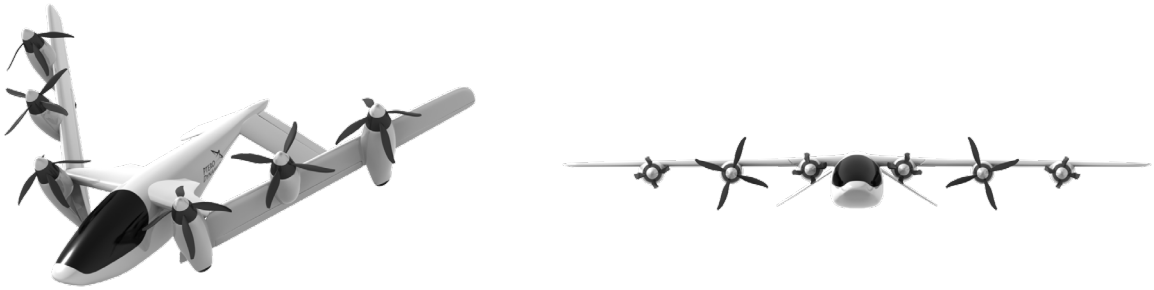

Fig. 2. Pterodynamics Transwing conceptual model [12]

Compound aircraft combine the vertical lift capability of a traditional helicopter with the additional thrust provided by the rear rotor or other propulsion systems, achieving higher speeds than conventional aircraft. However, it is usually limited up to 195-240 knots during cruise due to transonic speeds in the advancing blade of the main rotor [13]. Potential high maneuverability characteristics have been reported [14], while the development process is still upon step-improvements. The most popularized model is attributed to the Sikorsky S-97, which comprises two coaxial-counter-rotating main rotors and a push-propeller located at the tail, as represented in Fig. 3.

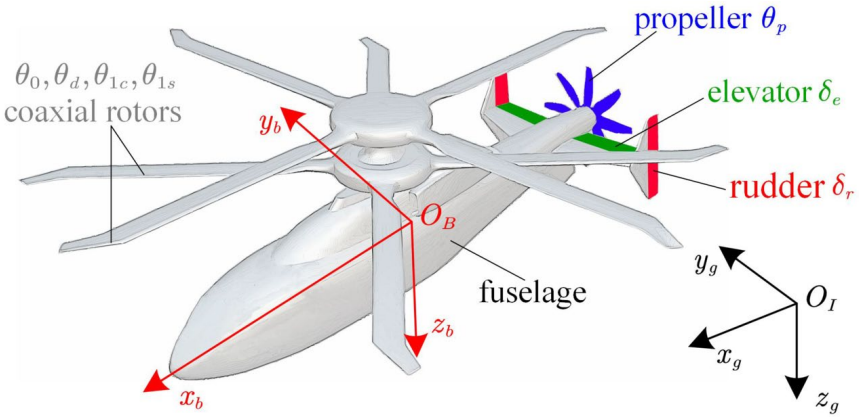

Fig. 3. Compound aircraft generic representation, including tail-control surfaces [17]

Tail-sitters takeoff and land on their tail, employing their pitch control surfaces to reorient their axial body axis component parallel to the wind [15]. In some cases, thrust vectoring might be used, but commonly, the propulsion system is non-orientable with respect to the aircraft. The highly complex flight control methods needed, leading to low safety values, and the lack of ergonomics

associated with its drastic changes in attitude imply that this type of aircraft remains being used for unmanned operations [16]. The Ryan X-13 Vertijet is reported to be the first tail-sitter, which successfully performed all the flight modes and transitions as early as the 1950s [17].

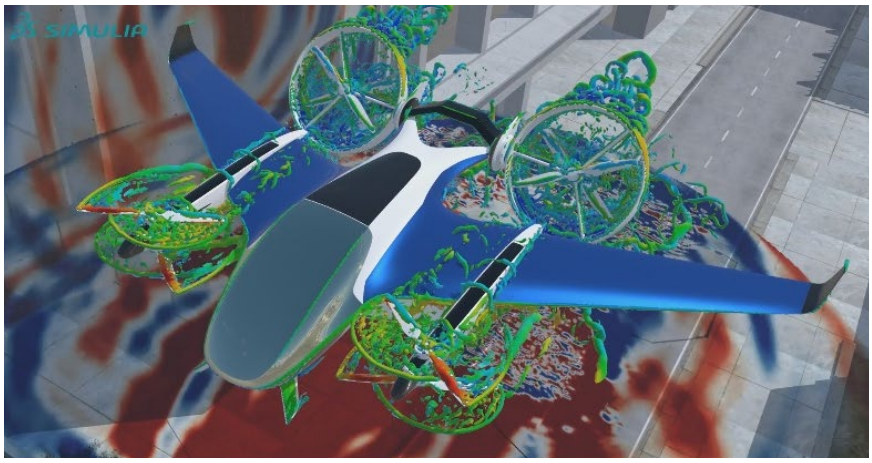

Fig. 4. Dassault Systèmes UAM model in their in-house 3DEXPERIENCE platform [23]

Lifting-dedicated rotors appeared in the early 1960s to give VTOL capabilities to fighter jets. The USSR and Western nations considered this type of system on aircraft such as the Su-24 and Yak-38, with no evident success due to large dead weights and volume consumption [4]. The US military later implemented these lifting systems in aircraft such as the F-35B for navy missions, with appropriate performance results [18]. Currently, propulsive systems dedicated to vertical motion have gained protagonism again for Urban Air Mobility (UAM) vehicles for activation during the low-speed flight phases. Fig. 4 shows two pairs of lifting-dedicated rotors at the front of the wing's leading edge.

1.1.3. Iconic Programs and Industry Challenges

Numerous organizations have been involved in developing tilt-rotor aircraft since the mid-twentieth century, including NASA, Boeing, Bell, and the US Army Engineering teams. The XV-3 served as a proof-of-concept in 1953, while the XV-15 research plane was researched thoroughly in wind-tunnel and flight-test environments, yielding vast amounts of data [19]. Today, extensive public models and flight data are available for the XV-15, allowing engineers to inspire the design procedures considered during its development. More modern aircraft partially derived from the previously mentioned ones are the Bell XV-22, V247, and the civil version AW609, currently under certification phases. All the previous aircraft models have been developed in the U.S. environment, except the AW609, which was developed under the EU environment by Leonardo S.p.A.

The ERICA (Enhanced Rotorcraft Innovative Concept Achievement) [20] project was proposed at the beginning of the 2000s as part of a European initiative to create an advanced tilt-wing/rotor configuration. The project utilized a partial tilt-wing concept to address issues associated with traditional tiltrotors. Even though the configuration was analyzed by in-depth research centers such as ONERA [21], a complete or high characterization of the aerodynamic behavior of the partial wing solution has not been reported to be solved, at least publicly. The aerodynamic database and experimental data gathered during the project are not publicly available for the ERICA analysis, thus not a viable option as numerical inputs and validation scenarios for third-party studies.

Various research and development European-based institutions and companies are currently active on various VTOL configurations. Two main focal points are detected: UAM and medium-long-range civil and military VTOL operations. Some other active programs, others than as per the previously commented, are:

- Airbus Helicopters, a division of the Airbus Group, is developing a UAM aircraft called the CityAirbus NextGen. The CityAirbus is designed to be a zero-emission electric UAM, carrying up to four passengers [22] and propulsed by several tilting and lifting dedicated rotors. A previous model proposal comprised four significant pairs of counter-rotating-coaxial rotors attached to the fuselage, i.e., without a wing base. However, this last model seems to have lost prominence for the final application, and it has been used more in the concept of a flight-lab.
- The European Defense Agency (EDA) is funding a research program called the Next Generation Rotorcraft Capability (NGRC) program. The NGRC program is focused on developing advanced rotorcraft technologies, including tilt-rotor and tilting-wing concepts, to meet the evolving needs of European military forces [23].
- The ATTILA project aimed to design, manufacture, and test an advanced testbed for aeroelastic wind tunnel testing of tilt-rotor aircraft, a partnership of various Netherlands-based research centers and the University of Politecnico Di Milano. The project funding is expected to be finished on the 31st of December, 2023 [24]. This project has released several papers, mainly focused on the aeroelasticity phenomena.

1.2. Actual Rotorcraft and Flight Dynamics Modelling Strategies

1.2.1. Preliminary Requirements

As the VTOLs are multi-body systems, their flight dynamic models should be constructed attending to the coupling effects of motion, inertia, structure, and aerodynamics, including unsteadiness and nonlinearities processing. Key components to include in the modeling process are the rotor (with its degrees of freedom), fuselage, horizontal and vertical tails, and the coupled rotor/engine/fuel control systems. Although some studies may overlook it, it is necessary to consider the inertia parameters of the aircraft and its subsystems. The code organizing the aircraft model should be structured as a driver code that sequentially calls upon the elemental models. The desired output of this driver code is the time derivatives of the dynamic states in the model.

The simulation setup must determine whether the model operates in non-real-time or is part of a man-in-the-loop effort with hardware interfaces. In cases where the same code is used for batch and real-time processing, the code must be designed to receive control inputs through hardware interfaces or from input files containing control input time histories. For real-time simulations, the ability to trim at arbitrary points, reset to those trim points, and execute the equations of motion normally or freeze execution is desirable.

In terms of trimming the aircraft, the flight dynamic model should be able to achieve steady-state flight conditions, allowing to specify the trim assignment, considering factors such as the degrees of freedom to be trimmed, constraints on dependent variables, candidate variables (controls) for achieving the trim, bounds on candidate variables, and initial guesses. Identification of algebraic loops and necessary integrations to determine the number of initial conditions and distinguishing user-defined constants and variables from those derived from user-defined data.

The aircraft flight dynamics model is the basis for the Handling Qualifications assessment and definition of the FCS. The evolving rotorcraft configurations require more sophisticated modeling techniques than traditional rotorcrafts or airplanes. This complexity is necessary to meet the increased demands for diverse flight modes and control of the multiple DOFs.

1.2.2. Challenges of Proprotors Modelling

Proprotors must exhibit superior aerodynamic performance across a broader spectrum of flight conditions than helicopter rotors or propellers. Consequently, their net performance faces compromises between their primary modes of operation. For instance, a proprotor in hover is generally less efficient than a helicopter rotor, having a lower power loading and figure of merit. In forward flight, a proprotor tends to be less efficient than a propeller, exhibiting lower propulsive efficiency. In hover, proprotors generate thrust to counteract the vehicle's weight, plus any airframe download, necessitating generous blade areas and higher tip speeds. Conversely, in cruise mode, where thrust only opposes aircraft drag, achieving good propulsive efficiency requires minimizing profile losses and adverse compressibility effects, leading to less blade area and lower tip speeds on the proprotor.

Rotor blades are susceptible to various non-linear flow phenomena, including separated flow and shock waves, particularly at the advancing blade. In addition, disturbed and turbulent flow conditions arise near the wingtips and rotor tips due to the formation of wake vortices. These wake vortices rapidly roll up and create highly non-linear and turbulent flow patterns, imposing challenges for rotor aerodynamics modeling. These complex flow phenomena significantly affect the accuracy of pure analytical models in predicting the performance, stability, and control of rotor systems. The prediction of airframe download is complex and better suited to physics-rich methods due to the three-dimensional flow fields of the problem [25].

Blade twist is a delicate compromise between the two primary modes of flight operation, requiring significantly less twist in hover to prevent inboard blade stall. Proprotors must maintain generous stall margins to ensure sufficient control capability and maneuverability at low airspeeds. Consequently, designing a proprotor for high cruise speeds, demanding excellent static thrust and efficiency, unlike a propeller, proves challenging and may lead to compromised performance levels. Another critical aspect of proprotor design is the necessity for robustness in off-design operations, which involves designing sufficient stall margins into the proprotor to accommodate maneuvers, gusts, altitude effects, and inevitable empty weight growth due to operational demands and future upgrades [26].

The interaction between the rotor system and other aircraft components is crucial in developing accurate flight dynamics models. These interactions can be classified as lateral or axial interactions. Lateral interaction has a more significant impact on rotor performance as the angle of attack increases. At low angles of attack, small tip gaps (around 1-2% of the rotor diameter) result in time-averaged penalties, but at high angles of attack (75-90°), these penalties can escalate to 5-15% [27]. Lateral interaction also induces unsteady blade loading caused by inflow perturbations, leading to vibrations, decreased efficiency, and increased noise emissions. Axial interactions, on the other hand, significantly affect time-averaged rotor performance, with downstream rotors experiencing up to 30% higher power consumption for a given thrust [28]. These interactions result in unsteady blade loading due to periodic interactions with blade wakes and tip vortices. The challenge of rotor

dynamic -modeling is amplified in the case of UAM aircraft, where axial rotor interactions are more prevalent than in conventional rotorcrafts.

The rotor wake model shows how crucial it is for accurate rotor dynamic modeling, with the incorporation of multi-rotor aircraft. Existing rotor wake models face issues of numerical instability and inefficient calculations, being accentuated when integrating the flight dynamics model with the discrete rotor wake model. Several published studies have explored the integrated approach between wake and flight dynamics models, revealing the potential of rotor wake models to enhance accuracy and computational efficiency in flight dynamics modeling [29].

1.2.3. Integration of Modelling Theories

Proprotor performance evaluations can be tackled through various methods, from low-fidelity and low-computational costs to the opposite side of the spectrum. One straightforward method of employing the Blade Element Momentum Theory (BEMT) is a fusion of the Blade Element Theory (BET) and the Momentum Theory, introduced by William Froude in 1878 and is commonly employed nowadays. BEMT was born as one of the first modeling theories of proprotors, providing a practical framework for evaluating the performance of propellers and rotors, especially at hover and axial flow conditions [30]. More sophisticated techniques involve inviscid surface methods like panel methods coupled with a free vortex wake model (FVW), offering a better resolution of the overall flow field. Solutions from viscous CFD methods provide high-fidelity results but have a substantial computational cost, limiting the number of computation loops launched under standard limits. A representation of the benefits of these methodologies is given in Fig. 5.

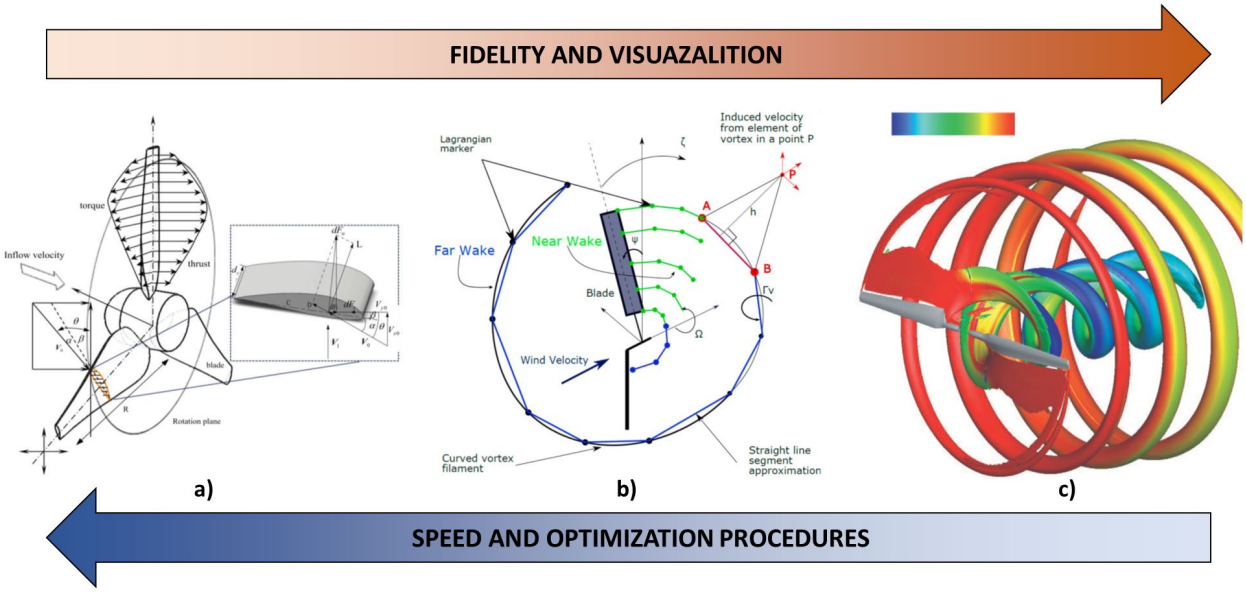

Fig. 5. a) Velocity triangle and force analysis of conventional BEMT [31], b) Free Vortex filament Method (FVM) with Lagrangian markers [32], c) CFD Aerodynamic wake at iso-surface of Q-criterion [33]

Authors have proposed BEMT models, with the UH-60 Black Hawk helicopter as a test-bed reference [34]. These models determine central rotor speed values to minimize helicopter power for different advancing speeds, subsequently calculating fuel flow variations using a turboshaft engine model. Recent research has integrated algorithms into these models, suggesting that minimizing main rotor power at intermediate advancing speeds is equivalent to minimizing fuel consumption.

However, at high and low forward speeds, the decrease in Free Power Turbine (FPT) efficiency due to main rotor speed variation outweighs the benefits of overall power reduction, which aligns with the limitation that a fixed transmission ratio is considered.

The absence of a direct correlation between minimizing power requirements for specific flight conditions and minimizing Specific Fuel Consumption (SFC) originates from the fact that the turboshaft engine Free Power Turbine (FPT) operates optimally at a speed generally distinct from the main rotor's optimal speed. In helicopters with fixed-ratio transmission, utilizing a variable RPM rotor demands careful consideration of the interaction between the main rotor and the FPT. The main rotor's optimal speed depends on advancing speed, weight, flight path angle, and ambient conditions. Rotor blade designs tailored for variable rotor speed must maintain a broad Mach range rather than a wide angle of attack range, potentially leading to vibrations, stability, and controllability issues. Low RPM settings on high-speed flights are a topic that should be evaluated due to reduced autorotation in case of engine failure.

As technology progresses, the relevance of BEMT persists, showcasing its adaptability in the face of evolving computational capabilities and modeling challenges. The ongoing integration of BEMT with higher fidelity theories as a preconditioner for fine-tuning the proprotor development process phases. Various modifications have extended BEMT to non-zero incidence angles, accounting for nonuniform inflow around the azimuth [35]. Another approach, allowing BEMT to consider large inflow angles, has been recently proposed by Stahlhut [26], further discussed in §3. Other approaches like BET with dynamic inflow models [30] yield accurate aerodynamic predictions for edgewise flight, providing off-body flow-field information away from the propulsor disk. The capability to evaluate various operational scenarios and consider geometric factors allows the system to generate internal optimization loops for determined performance parameters by altering the trimming of the system or modifying the geometrical characteristics of the proprotor.

1.2.4. Main Proprotor Performance Parameters

The performance parameters of proprotor blades are generally derived from the lift (dL) and drag (dD) at each blade section or element, according to Formulas (1.2.4.1) and (1.2.4.2) respectively. Each blade element's lift and drag are computed classically by reading the air density (ρ), total velocity (dV_T), section chord (dc), and the corresponding aerodynamic coefficient. The sectional lift (dC_L) and drag (dC_D) coefficients, from Formula (1.2.4.3) are a function of the airfoil polar ($dPolar$), the Reynolds number in the section (dRe), and the local angle of attack ($d\alpha$). The span of each blade element, dy, is implemented to account for the width of each blade element section. Further information about the signs convention and the physical meaning of the parameters is given in §3.1.

$$dL = \frac{1}{2}\,\rho\, dV_T^2\, dc\, dC_L\, dy \tag{1.2.4.1}$$

$$dD = \frac{1}{2}\,\rho\, dV_T^2\, dc\, dC_D\, dy \tag{1.2.4.2}$$

$$dC_{L,D} = f(dPolar, dRe, d\alpha) \tag{1.2.4.3}$$

The trigonometrical relation between each section's lift, drag, and inflow angle (ϕ) characterizes each blade element's thrust (dT) and torque (dQ). The number of blades in the proprotor (N_b) is multiplied for each aerodynamic load.

$$dT = N_b\ (dL\ cos(\phi) - dD\ sin(\phi)) \tag{1.2.4.4}$$

$$dQ = N_b\ (dL\ sin(\phi) + dD\ sin(\phi))\ Y \tag{1.2.4.5}$$

The absolute position of the blade elements (Y) can also be defined in the following mathematical or computationally-wise expressions. In this occasion, the blade root cut-out (r_0) and the infinitesimal blade section position (dy) are evaluated.

$$Y = \left\{r_0 + \frac{dy}{2}, r_0 + \frac{3dy}{2}, \dots, r_0 - \frac{dy}{2}\right\} = r_0 + \frac{dy}{2} : dy : r_0 - \frac{dy}{2} \tag{1.2.4.6}$$

The sum of the parasite ($dP_{parasite}$) and induced power ($dP_{induced}$) components gives the total power required at each section, by considering the proprotor angular speed (Ω). The induced power is associated with the lift generation and overcomes the induced drag associated with producing lift. On the other hand, the parasite power is associated with the form and skin friction drag.

$$dP = dP_{parasite} + dP_{induced} \tag{1.2.4.7}$$

$$dP_{parasite} = N_b\ (dL\ sin(\phi)\ Y\ \Omega) \tag{1.2.4.8}$$

$$dP_{induced} = N_b\ (dD\ cos(\phi)\ Y\ \Omega) \tag{1.2.4.9}$$

The thrust, power, and torque coefficients (C_T, C_P, C_Q) are directly proportional to the gross thrust (T) and the power (P) and torque (Q) required by the system. These are likely the most iconic parameters on a rotorcraft performance model since they translate directly to the power demands and the thrust generated by the system. Authors, at their preference, would generally choose C_P or C_Q to illustrate their system's energy consumption-related parameters. The rotor disk area *(A)* is defined as $\pi\ R^2$.

$$dC_T = \frac{T}{\rho\ A\ (\Omega R)^2}, \quad dC_P = \frac{P}{\rho\ A\ (\Omega R)^3}, \quad dC_Q = \frac{Q}{\rho\ A\ R\ (\Omega R)^2} \tag{1.2.4.10}$$

$$C_{T,P,Q} = \sum_{1}^{elements} dC_{T,P,Q} \tag{1.2.4.11}$$

The figure of merit (FM) measures the rotor's efficiency in converting engine power into useful thrust to stay airborne. Once integrated with a rotorcraft performance model, it is commonly used as an efficiency metric at a given disk loading C_T/σ.

$$FM = \frac{1}{\sqrt{2}}\ \frac{C_T^{3/2}}{C_P} \tag{1.2.4.12}$$

The propulsive efficiency (η) indicates how effectively the power available at the shaft is converted into useful power for maintaining flight at a specific free-stream speed. The η might not be used to give the efficiency of the proprotor system in some cases since at hover, i.e., at zero free-stream speed (V_∞), it drops to a null value.

$$\eta = \frac{T\ P}{V_\infty} \tag{1.2.4.13}$$

The advance ratio (J) is the ratio of the free-stream fluid speed to the tip speed, providing a dimensionless measure of the forward speed, rotational speed, and proprotor diameter. As the advance ratio increases, the relative velocity of the retreating blade decreases, reaching zero velocity at an advance ratio of one.

$$J = \frac{V_\infty}{\Omega R} \tag{1.2.4.14}$$

Following the definition and description of the main proprotor performance parameters, it has been considered that for this project, the reference parameter for evaluating the trimming of the proprotor efficiency is the FM. However, the propulsive efficiency and the advance ratio calculations are integrated into the proprotor performance algorithm, which are explained in later sections of this project.

1.2.5. Potential Proprotor Trimming Solutions

Robust design is particularly crucial for proprotors, given the less-established performance characteristics than helicopters or airplanes. To address uncertainties, proprotors should be designed to minimize losses in efficiency and operating margins in case of overestimated aircraft performance. Balancing design parameters such as disk loading, solidity, blade pitch, and rotational speed is essential to meet the performance requirements of hovering and high-speed forward flight while ensuring overall robustness.

Reducing the tip speed in forward flight can improve propulsive efficiency by allowing proprotor blade sections to operate at higher lift-to-drag ratios. Recent studies suggest that varying the helicopter main rotor speed significantly reduces required power, necessitating suitable drive train technology for variable rotor speed. However, this technology has drawbacks, including increased weight and reduced efficiency [36]. Variable rotor speed optimizes rotorcraft across the operational design range rather than a specific point.

Modern helicopters typically feature turboshaft engines with a constant speed-free power turbine (FPT), which is located in the Turbo-Machine Module (TMM), and a constant-ratio Reduction Gear Box (RGB). A generic representation of a turboshaft engine coupled with the RGB and the proprotor itself is given in Fig. 6. The FPT's rotational speed is regulated by Full Authority Digital Engine Control (FADEC), adjusting fuel injection to maintain rotor speed as consistently as possible. Allowable speed variations for the FPT generally do not exceed 15%. Choosing a constant rotational speed for the FPT is driven by two main factors:

- TMM efficiency regime: Turboshaft engines operate efficiently within a narrow RPM range, particularly affecting the FPT by variable speed. Breaking the interdependence between FPT speed and main rotor RPM or enhancing FPT design can address this issue without significant thermodynamic losses. Another potential solution is to improve the design of the FPT stages to extend the efficiency interval of the turbine, which has also been reported to be a feasible option [34].
- Resonant frequencies in the airframe: Variations in rotor speed can induce resonant frequencies, affecting both shaft critical speeds and the airframe. Advances in materials science enable accommodating varying rotor speeds without encountering resonant frequencies. Rotor blade design typically avoids matching flap, lag, and torsional Eigenfrequencies with rotor harmonics at nominal rotor speed to mitigate vibratory loads on the helicopter.

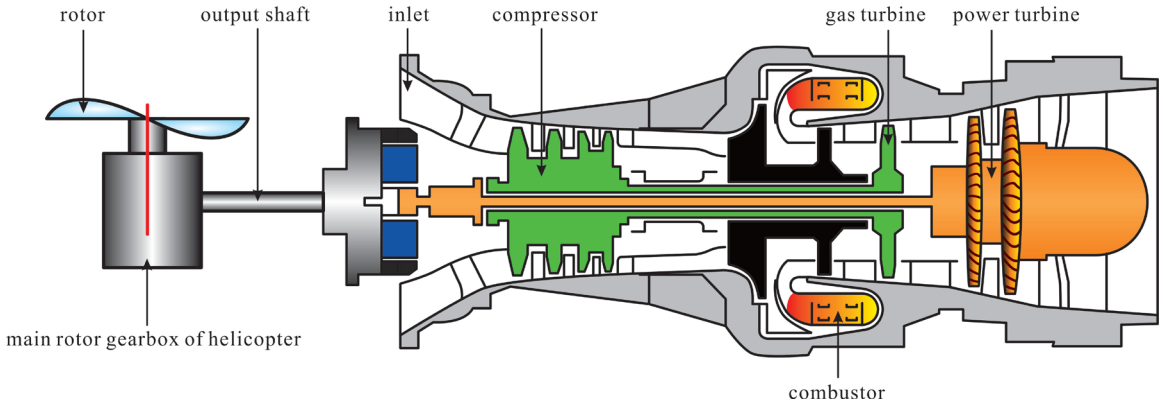

Fig. 6. Turboshaft engine and proprotor system structure [37]

The more diverse the mission-type segments get, the more appealing Continuously Variable Transmission (CVT) systems become. A configuration with this feature can be tailored to specific missions, unlike configurations limited to one segment. The primary constraint is the gearbox due to increased torque and power loss in attached auxiliary units with decreasing RPM. Using variable gearboxes close to the rotor can address these challenges, even though the weight increase for the speed variation unit is higher due to higher torque. Dual-speed transmission systems suit configurations with two distinct working areas, like tiltrotors. Additional turbine-driven continuous speed variation, as seen in the Airbus VARTOMS system, can minimize Specific Fuel Consumption (SFC). The VARTOMS system, represented in Fig. 7, achieves a 96.5-103.5% speed range of the nominal RPM based on air density and flight speed [38]. NASA's Heavy Lift Rotorcraft System has introduced three types of CVT transmissions with a speed range of up to 50% [39].

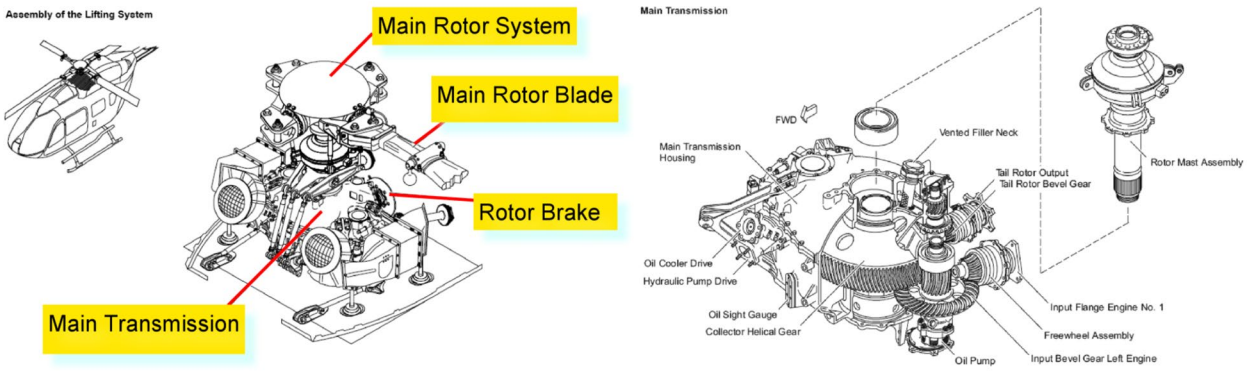

Fig. 7. Airbus VARTOMS CVT system [38]

Calculating the weight increase and maintainability requirements due to the complexity of variable rotor and transmission systems is to be considered under the operational frame of each mission. The U.S. Future Vertical Lift (FVL) program assumes a 10% weight addition for a variable transmission gearbox while underscoring the need to keep the increase below 30% [40]. CVT solutions offer smooth speed ratio adjustments without friction-based elements like clutches, though predicting additional weight remains challenging due to configuration variability and torque load dependence.

The manipulation of blade pitch is critical for controlling thrust and its relationship with the power required. Generally, rotorcrafts or helicopters achieve blade pitch changes through collective control. The collective alters the rotor blades' pitch angle simultaneously by a swashplate. Higher collective angles are desired when higher thrust is desired. In the case of propeller aircraft, a similar principle is applied through feathering, as given in Fig. 8. The propeller is said to be feathered when the blade chord is aligned with the incoming airflow, i.e., the leading edge is towards the front, which is usually used in cases of power failure. On the other hand, once the blade chord is aligned with the rotational plane, the blade is on fine pitch, which is used for low-speed regimes. In cases of high-speed flight, the blade is feathered in an intermediate position.

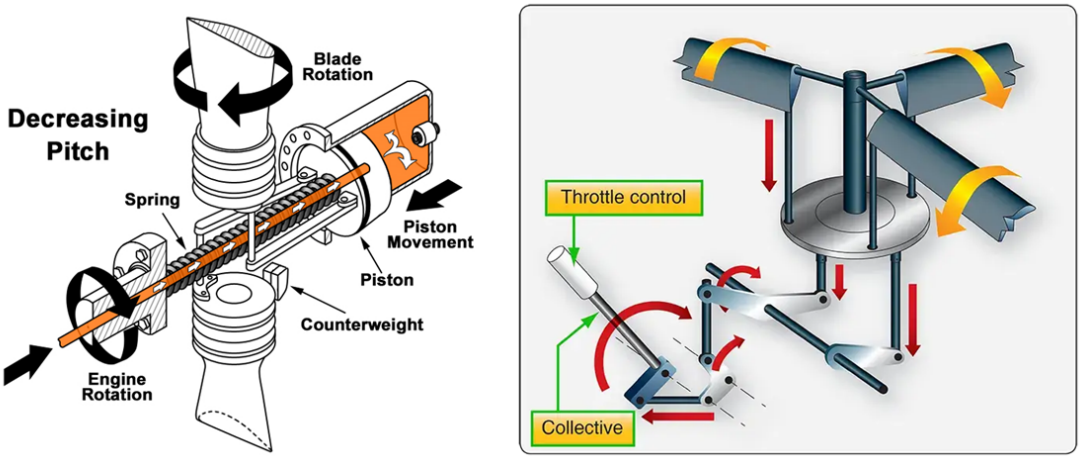

Fig. 8. Feathering and collective/throttle controls, respectively [41]

By increasing the collective pitch, the blades generate a steeper angle of attack, effectively increasing the amount of thrust produced at the expense of increasing the power required. Feathering, however, is oriented to rotate the blades parallel to the airflow, reducing their angle of attack and minimizing drag in high-speed flight. A hybrid mechanism between collective and

feathering might be found in the case of VTOL aircraft, which operate from hovering to high-speed flight inside the limits of a propeller envelope. The collective, with the highest response rate, would be associated with the low-speed regimes and the feathering with a higher rotation range for high-speed flight.

2. Modeling Aircraft Input Data for the Flight Dynamic Model

2.1. Preliminary Characterization

The Aircraft Specific Data (ASD) is the data necessary to feed the flight dynamic model with the characteristic properties of the studied aircraft. The ASD was constructed for the Bell XV-15, one of the first successful tilt-rotor aircraft, for which a vast amount of data is available. The XV-15 is an advanced high-wing tilt-rotor aircraft with dual tandem proprotors near the wingtips, enabling vertical takeoff and landing capabilities, as shown in Fig. 9. The empennage consists of an H-tail, where the rudders and the elevator are located. Each proprotor system comprises three blades and is mounted on a gimbaled hub, employing control mechanisms similar to conventional rotorcraft, such as collective and cyclic inputs.

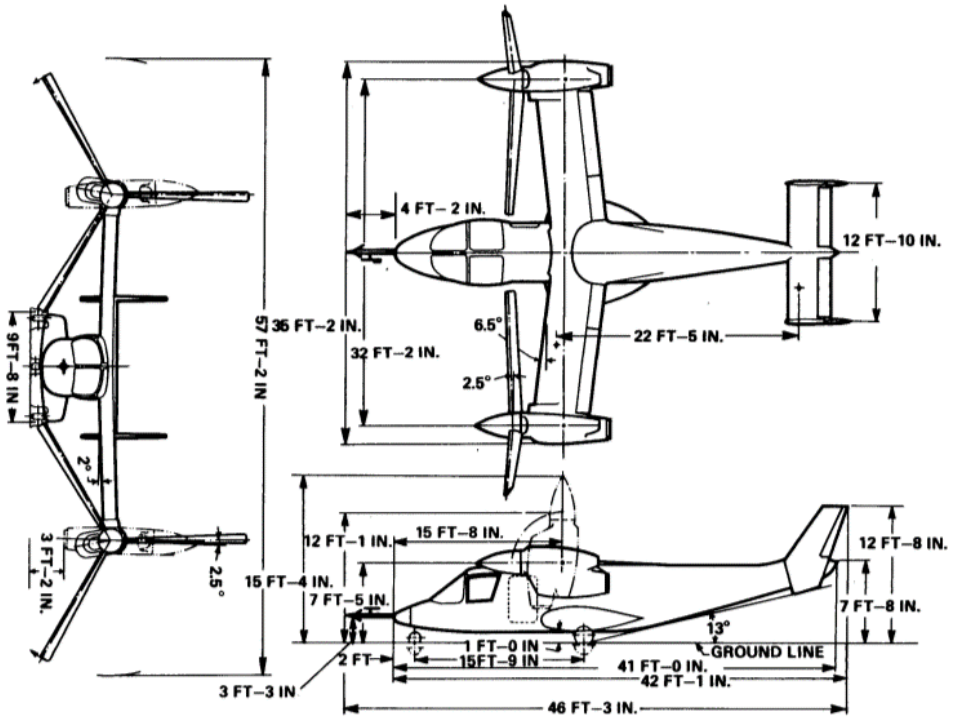

Fig. 9. General dimensional characterization of the XV-15 [42]

The data used in this study is obtained from the XV-15 Generic Tilt Rotor Simulation (GTRS) model, which is a validated aeromechanics model [43]. The GTRS results serve as a means to validate the flight dynamic model and analyze the effects of interactions between aircraft components for the specific characteristics of the mentioned aircraft. In situations where flight test data is not available, like the current state of this study, the GTRS data stands as the only publicly accessible source for trim and performance information specifically for tilt-rotor aircraft. The GTRS favored employing table lookups and correction factors to improve flight correlation rather than relying solely on basic physical equations for aircraft modeling.

During the initial stages of the transition phase, the various tilting angles of the wing tend to produce differing levels of propulsive forces [8], as the lift generated by the outward wing is significantly smaller than the total aircraft's lift. The independent rotation of the more external wing region with respect to nacelle rotation enables the mechanism to minimize the downwash in the higher degrees of the nacelle rotation. To achieve high-fidelity flight dynamic modeling, projects such as the XV-15s demonstrated how careful attention to the mathematical model and issues

related to usual simulation problems such as motion and visual systems, as well as correlated with the actual flight characteristics of the aircraft, is crucial [44]. The control dynamics in the transition phase can be considered a mixture of the rotor and airplane surface forces and moments. The different flight modes can be defined depending on the rotor hub angle (RHA). The rotor hub angle is defined as 0° when in "pure" airplane mode and 90° for "pure" helicopter mode.

The rotor hub angle changes cause pitch attitude transients and shifts in the overall CG. The other tilt-degree freedom creates an additional dimension in the flight envelope that the airspeed and the rotor tilt angle variables can represent. The corridor shows the safe transition range from the helicopter to airplane mode, representing the viable trim region within the aircraft's performance limits with thrust vectoring capabilities.

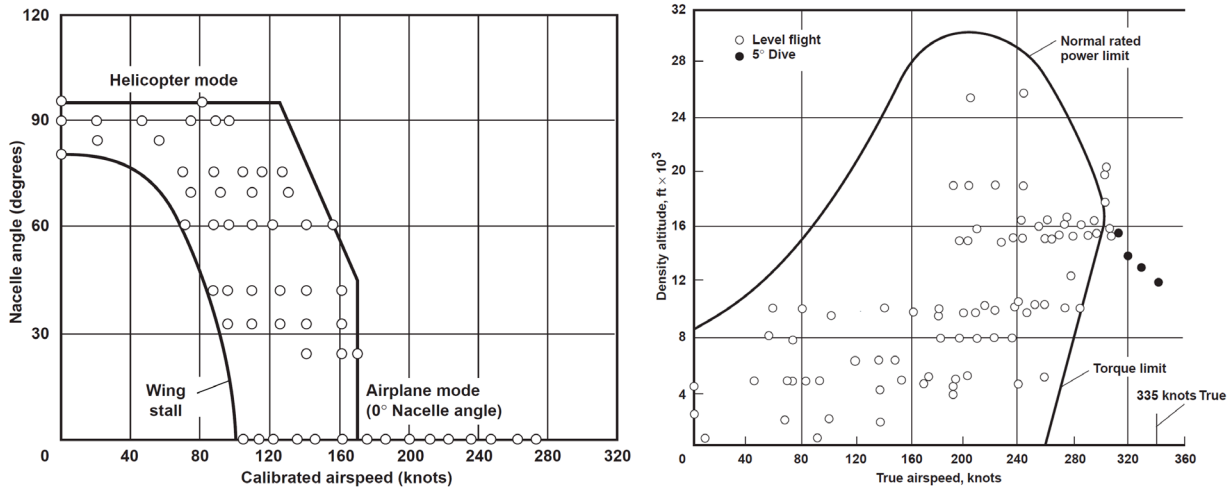

(a) (b)

Fig. 10. XV-15 conversion corridor (a) and flight envelope (b) [45]

General performance capabilities are represented in the height-velocity flight envelope, as adapted by [45] from [44]. Fig. 10 represents the flight envelope, including hover, transition, and airplane modes for the XV-15. No distinguishment has been given by any published source about the limits of the flight envelope depending on the rotor hub angles. Additional performance and limitation charts from the aircraft at different flight modes, power and propulsion units, rotors, and pilot controls are referred to in [42].

2.2. Flight Controls

During the development phase, it was generally agreed that the tiltrotor, required to perform helicopter-like takeoffs and landings, should use helicopter control mechanisms like a cyclic stick, collective stick, and pedals. However, due to the significant time spent in airplane mode, there was a growing belief that airplane control mechanisms like a yoke or stick, throttle, and pedals would be more appropriate.

As the control surfaces, such as the elevator, flaperons, and rudders, are limited directly by the relative wind velocity, they can be considered to be activated with full authority despite the rotor hub angle. Specifically by axis, the DOFs are directly controlled, as given in Fig. 11. The controlled systems are highlighted in red as mostly related to the airplane mode or high-speed regime and in blue as those related to the helicopter mode or low-speed regime. The dashed lines correspond to

those elements of the state vector that are excited by coupling the other state vector element accelerations.

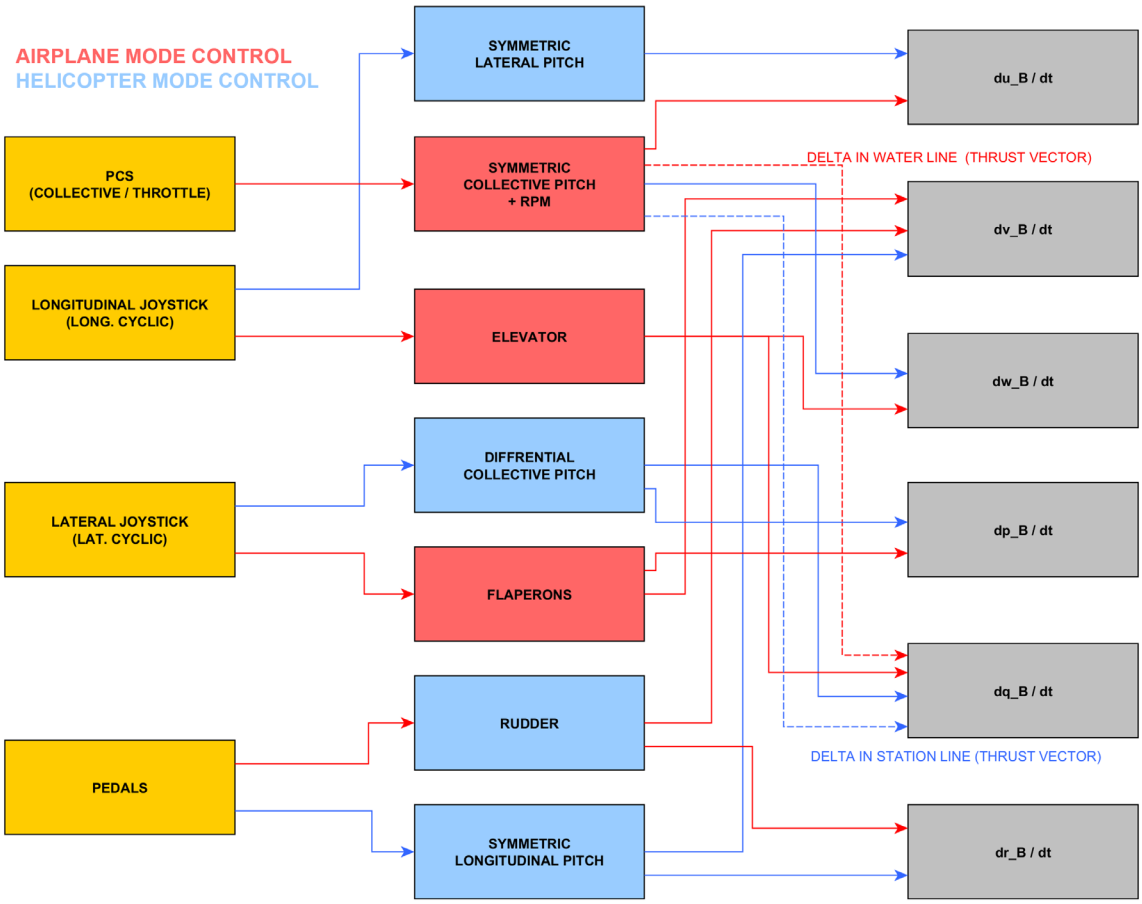

Fig. 11. Diagram of Principal DOFs of the Bell XV-15

From Fig. 11, the following observations are highlighted:

- The $\dot{r}_b$ only generates, by coupling, a $\dot{w}_b$, if the total vertical component of the thrust is not equal to the aircraft's weight.
- The rotors' RPM regime can be changed in helicopter mode, with a similar effect as an increase in rotors collective. The RPM for helicopter and conversion mode is 589 RPM, whereas it is 517 RPM for airplane mode.
- The maximum differential collective pitch is limited to 60° of the rotor hub.
- Lateral Swashplate Gearing (LSG), or lateral pitch, phases out to zero from 80 to 75 ° rotor hub. LSG also depends on airspeed, decreasing from the maximum values at velocities of 40 knots to zero for airspeeds greater than 60 knots.

Creating a control effectiveness map might help find a trim for a specific number of DOFs. This method pairs the various DOFs with the trim variable most effective at controlling them, as the previous table represents. However, in rotorcrafts and significantly for advanced architectures, the convergence of the correct solution might not be achieved, at least in an effective manner. Usually, the Jacobian method is the preferred one. A greater detail level about the adopted trimming strategy in the flight dynamic model is discussed in later sections of this project.

2.3. Mass Properties

In terms of mass properties, the fact that the XV-15 has the engines located proximately to the wingtips, it has a relatively high roll moment of inertia (I_{XX}). The values of I_{XX}, result to be considerably more significant than the pitch moment of inertia (I_{YY}). This effect can increase the tendency for Dutch roll, with a slower rolling motion but a faster yawing motion. It is to be noted that the inertia coefficients I_{XY} and I_{YZ} are not considered as the aircraft is supposed to always stay symmetric along the y-body-axis.

A collection of linear equations can be used to estimate the changes in the center of gravity (CG) in relation to the orientation of the rotor hub. This approximation consists of a variation of the original inertia value (I_{XX90}, I_{YY90} ...) referred to as the inertia for the pure helicopter mode. The variation applies an inertia coefficient (K_{IXX}, K_{IYY} ...) times the rotor hub angle (β_{RH}), which alters the total inertia value. The proposed set of equations, derived from the original OEM data, can take the following structure.

$$I_* = I_{*90} - K_{I*}\,(90 - \beta_{RH}) \tag{2.3.1}$$

The general aircraft mass properties are defined as given in Table 1, including the most representative aircraft mass and inertia values. After implementing the values and equations in the developed script, the inertial values for each rotor hub angle take the form represented in Fig. 11. For the particular example of this project, only the pitching moment inertia is represented, as the developed model is longitudinal. Further information about the mass properties related to fuel consumption is defined in §2.4.

Table 1. General Aircraft Mass Properties [19]

Definition	Parameter	Value	Units
Design Gross Weight	$MTOW_{VTO}$	5897	kg
Maximum Gross Weight	$MTOW_{STO}$	6804	kg
Minimum Flight Weight	MFW	4881	kg
Empty mass	MEW	4341	kg
Pitching inertia moment (helicopter mode)	I_{YY90}	21360	kg m^2
Inertia coefficient for pitching moment	K_{IYY}	11.24	kg m^{2}deg^{-1}

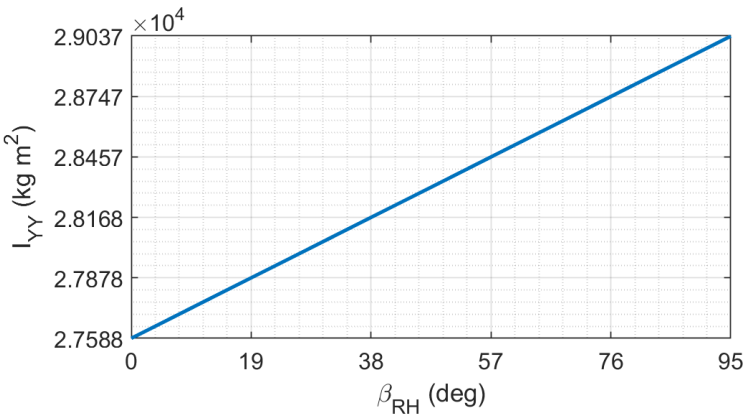

Fig. 12. Modeled pitching inertia coefficient at different rotor hub angles

The inertia moments are the same between the afterward and forward CG positions. These values are established for the Design Gross Weight of 5897 kg.

2.4. Powerplant Characteristics

The powerplant-heart of the XV-15 is two T-53-L-13B turbopropeller engines, which were later upgraded to the Lycoming LTC1K-4K, both fueled by conventional aviation jet fuel. Both engines are connected through a shaft across the wing, which permits power transfer from side to side in the case of an engine failure [42], as represented in Fig. 13. Thus, in the case of an engine failure, the total power available would be approximately divided by two and penalized by the transmission losses through the interconnection driveshaft and the center gearbox. The fuel is supplied to each engine by four separate fuel tanks in the wing. The total fuel capacity is 1509 lb (684.5 kg), of which 19 lb (8.5 kg) are unusable [42], thus leading to a usable fuel capacity of 676 kg.

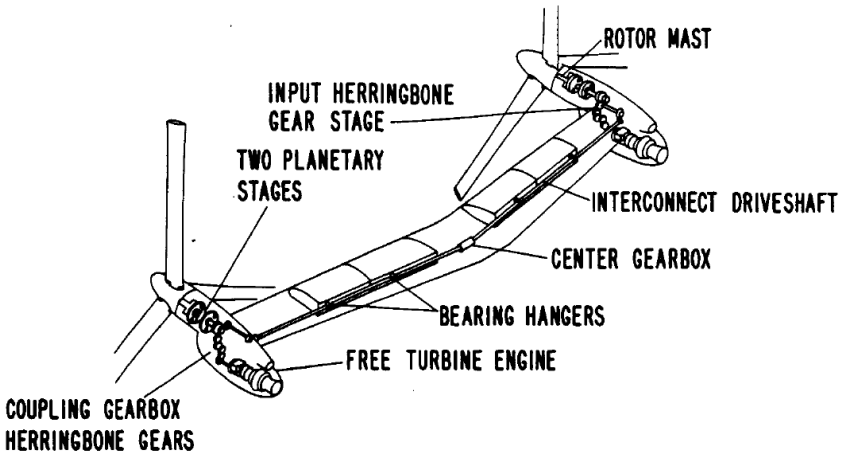

Fig. 13. XV-15 propulsion system schema [42]

Considering that the OEM performance charts provide the power characteristics for any engine and that analytical modeling of the propulsion system is out of this thesis's scope, the power available is extracted from the original charts and not by a general analytical approach. A data frame defining the available power function of the pressure altitude is created, as presented in Fig. 14. It is to be remarked that the pressure altitude is presented in feet units instead of meters, according to common units used in the industry.

Due to simplification purposes, the effect of speed is not implemented. It has been reported in the OEM references that at velocities higher than 150 kt, or approximately 77 m/s, higher power available is found. Another limitation is that temperatures different from the standard-day (ISA conditions) on the power available are not considered. The effects of humidity have not been declared in the performance charts.

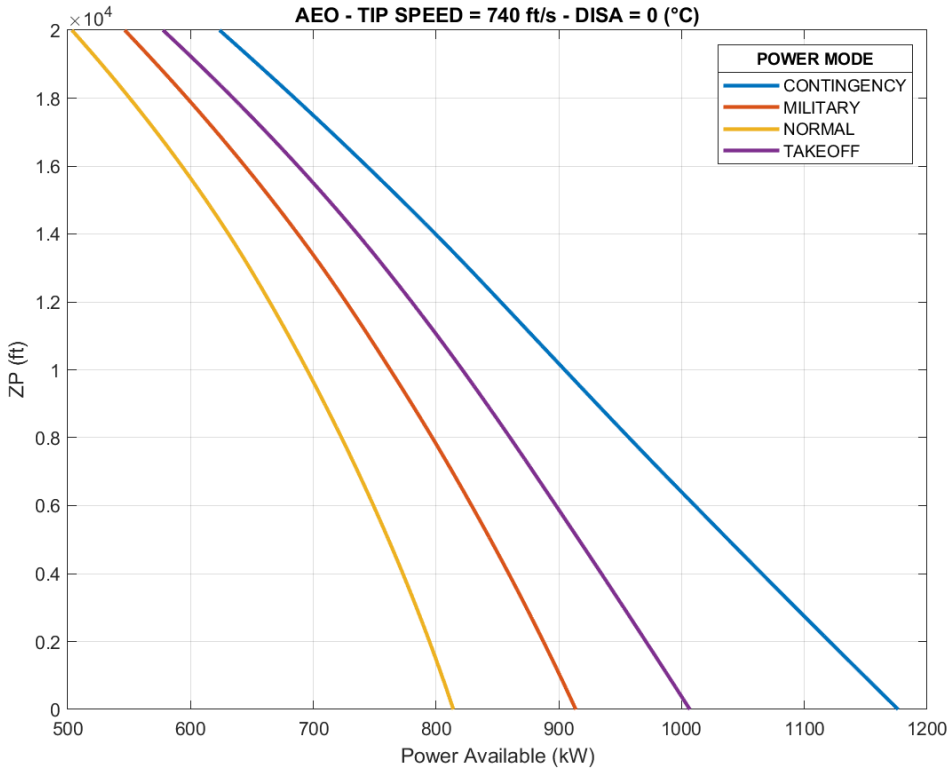

Fig. 14. Modeled power available characteristics

Besides the power limits from the powerplant itself, the transmission system limits the maximum power transmitted throughout the system due to structural requirements. According to the reported OEM data, the transmission system of the proprotor hub from the XV-15 has a maximum capacity of 705432 W during airplane mode [42]. No specific time limits or further information about whether this power would be equivalent to yield, or ultimate stress are reported.

Additional engine parameter characteristics, such as the SFC and the time limit at which the engines can operate at each power mode, are referred to in Table 2. The fuel consumption rate ($\dot{m}_{fuel}$) can be quantified by the product of the power required ($P_{required}$) and the SFC, as shown in the following equation. The power required is modeled in the following sections of this thesis.

$$\dot{m}_{fuel} = (SFC)\, P_{required} \tag{2.3.2}$$

Table 2. Powerplant time limits and fuel consumption characteristics [42]

Power mode	SFC (kg (kW hr)$^{-1}$)	Time limit (min)
NORMAL	0.3783	N/A
MILITARY	0.3656	30
TAKEOFF	0.3552	10
CONTINGENCY	0.3431	2

2.5. Aerodynamic Coefficients

The parametric OEM source [19] presents tabulated lift and drag coefficients for the wing with engine nacelles and the horizontal stabilizer included. Aerodynamic coefficients for other aircraft sections, such as the fuselage, are unavailable. The data is given for ranges of Mach from 0 to 0.2 and at the specific values of 0.4, 0.5, and 0. Considering that the aerodynamic coefficients do not

show a prominent change between Mach numbers, the lack of tabulated data at higher Mach, and the scope of work of this project for the low-speed phases, the aerodynamic coefficients are considered for the range of Mach 0 to 0.4.

The lift and drag coefficients are given for the rotor hub angles of 0 and 90 degrees and different flap settings. The different flap settings are denominated as $X_{FL1} = 0/0$, $X_{FL2} = 20/12.5$, $X_{FL3} = 40/25$ and $X_{FL4} = 75/47$ in the OEM data source. The numbers represent the downward deflection, in degrees, of the external/internal flaperons located in the wing. Following actual common practices on the denomination of the aerodynamic configurations, the previously represented flap settings configurations might be denominated as CONF0X0, CONF20X12P5, CONF40X25, and CONF75X47, respectively. The aerodynamic coefficients for airplane and helicopter modes are presented in Fig. 15 and Fig. 16.

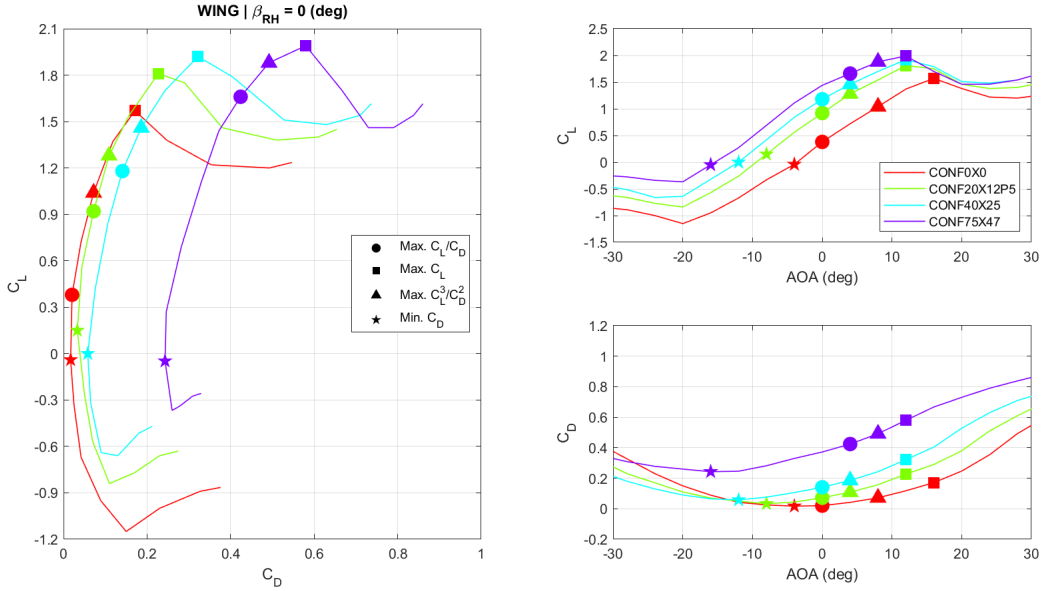

Fig. 15. Wing aerodynamic coefficients in airplane mode processed from OEM data [19]

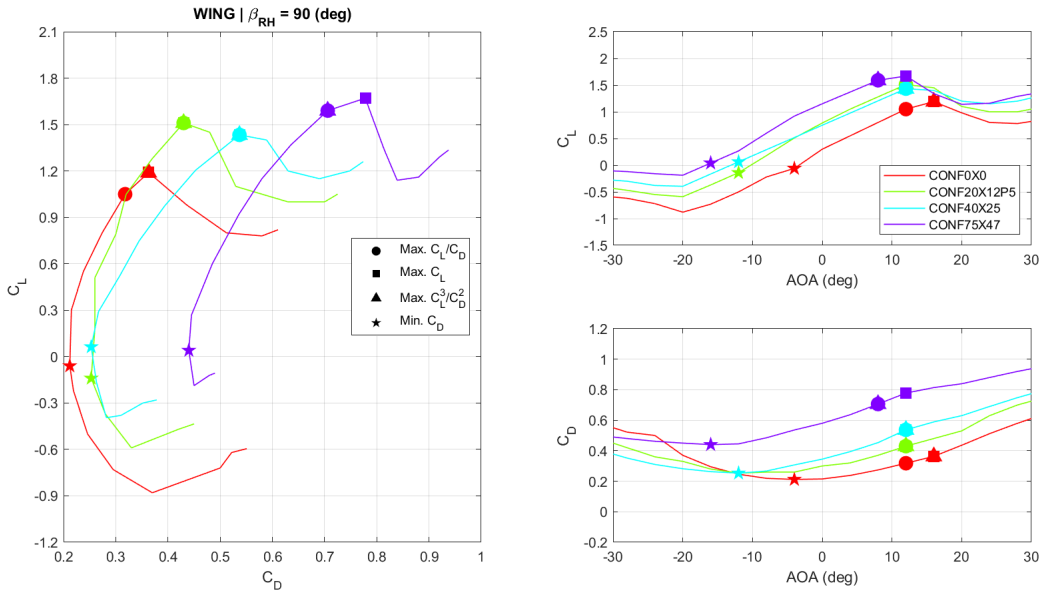

Fig. 16. Wing aerodynamic coefficients in helicopter mode processed from OEM data [19]

Since no data exists for intermediate rotor hub angles between 0 and 90 degrees, different strategies have been considered to obtain values at intermediate points. This practice is known in advance not to be strictly accurate, as the physical progression of the aerodynamic coefficients between maximum and minimum rotor hub angles is not linear and coupling between the rotor hub angle and the angle of attack couples for the aerodynamic coefficients.

The horizontal stabilizer data is presented for elevator angles between -20 (ELV_N20) and +20 degrees (ELV_20). The angle of attack of the horizontal stabilizer would be the same as both surfaces are fixed and attached to the fuselage. However, the downwash affects the nominal angle of attack of the tail, especially at low values of β_{RH}. The operational range of the angle of attack is considered to be more reduced than that of conventional fixed-wing aircraft since advanced rotorcraft configurations combine the angle of attack and thrust vectoring mechanisms to modify the propulsive forces on the different axes.

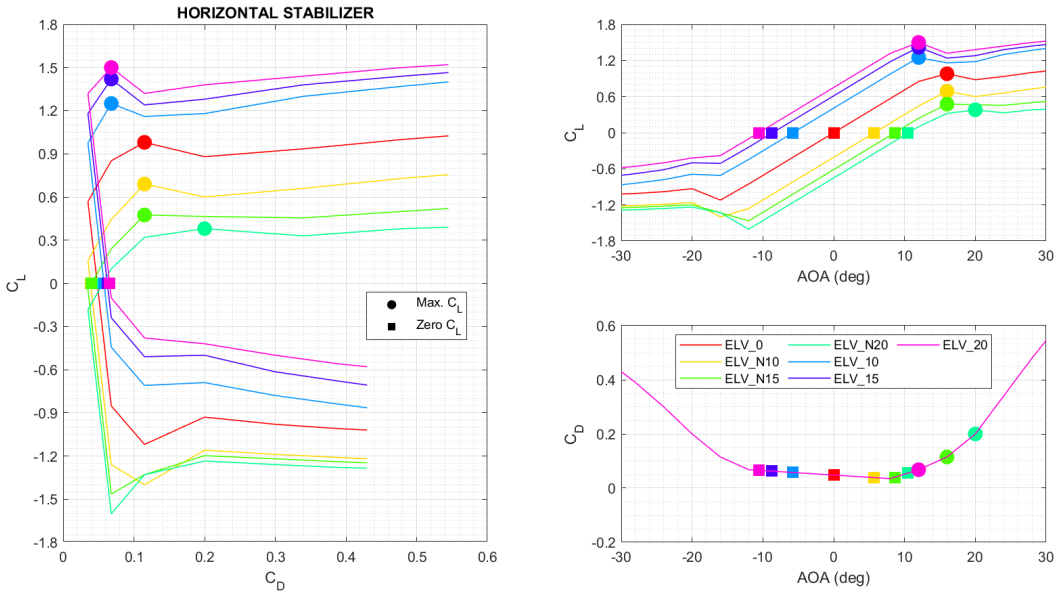

Fig. 17. Horizontal stabilizer aerodynamic coefficients processed from OEM data [19]

Extension of the represented data might be performed in future updates of this project, including the coefficients data for the vertical stabilizer and an evaluation of the yawing coefficients. This section has not been developed since the project was developed in the frame of a longitudinal flight dynamic model, which does not use these coefficients.

2.6. Proprotor Wake Interference

When the nacelle angle is at a high inclination, the proprotor wash impinges the fuselage and wing surface area underneath the rotor, which creates a force opposing the lift, denominated as a download. A graphical representation of this behavior over the whole wingspan is given in Fig. 18. This proprotor wake interference with the wing can lead to thrust losses between 10 and 15%, considerably reducing vertical lift capability. Current design strategies aim to mitigate this issue by deflecting the full-span wing flaperons to high angles, typically ranging from 60 to 70 degrees. This setup correlates with the standard practices of fixed-wing aircraft, especially during landing, to deflect their flaps and slats at or near the maximum.

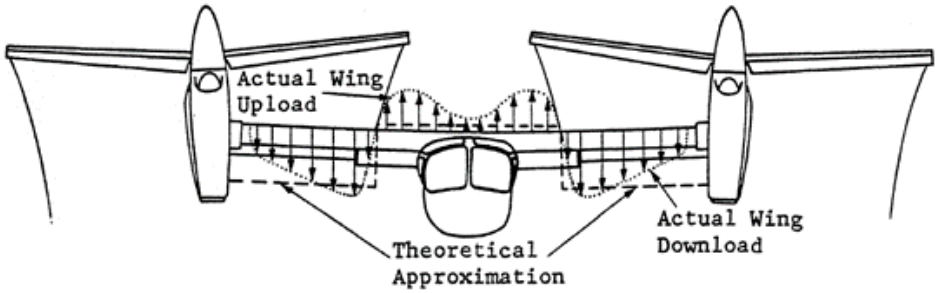

Fig. 18. Proprotor wake interference representation [19]

Experimental analysis of the XV-15 throughout flight tests and wind tunnel experiments determines that the main parameters affecting the download are the flaperon configuration, engine nacelle rotation, and the velocity of the X-body axis. The numerical values used for Fig. 19 are all retrieved from OEM data [46]. The near distance to the ground, i.e., ground effect conditions, have not been associated with calculations of the download in previously reported documentation. Even though short periods are spent in this condition, the effect on vertical lift capabilities might be a determining factor in landing and take-off performance.

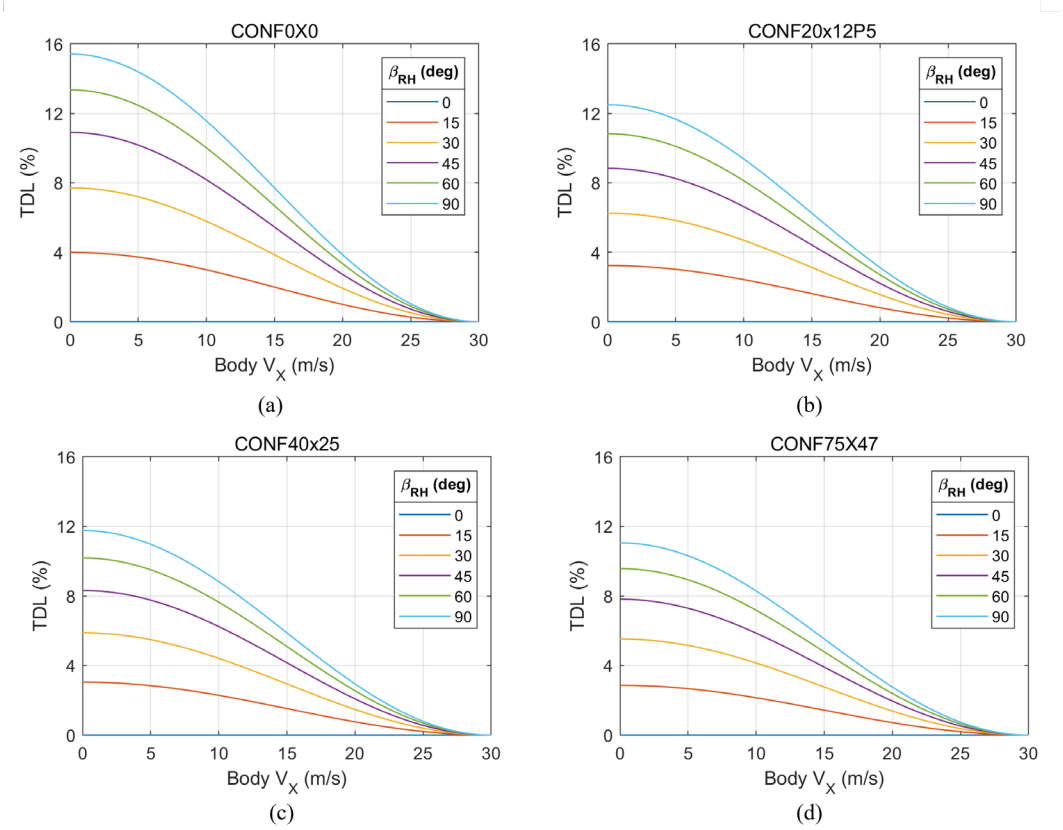

Fig. 19. Modelled wake interference at CONF0X0 (a), CONF20X12P5 (b), CONF40X25 (c), and CONF75X47 (d)

The semi-empirical equation proposed by ONERA [47] is implemented into the developed aircraft performance model. The equation is determined throughout a reference value of download at hover condition (TDL_{hover}), i.e., without any aircraft or wind speed, the current speed, the angular position of the rotor hub (β_{RH}), and an additional factor denominated in this document as the limit download speed (V_{lim}).

$$TDL = TDL_{hover}\left(1 - sin^2\left(\frac{\pi\, V}{2\, V_{lim}}\right)\right) sin\,(\beta_{RH}) \tag{2.6.3}$$

The download at hover conditions would need to be previously calculated through high-fidelity computations such as CFD methods or experimental techniques. The limit download speed is defined as the speed at which the proprotor wake does not impact the wing itself and, therefore, does not generate any wake interference against it. The reference value of 30 m/s is considered in the particular case of the XV-15.

2.7. Other Parameters

Besides the trim characteristics, performance limitations can be imposed on the velocity range: the stall speed at 1G acceleration (VS1G) and the maximum extended flaps speed (VFE). The VS1G refers to the straight-and-level stall speed of the wing. VS1G is the lowest airspeed at which the wing is on the verge of losing lift while maintaining a constant altitude. This phenomenon is not to be directly associated with the aircraft loss of altitude, as in the case of cases in which the maximum T/W ratios are superior to the unity, which might be coupled with a reorientation of the thrust vector.

Therefore, the VS1G is defined according to the following formula. For the particular case of the presented ASD, the stall speed is dependent on the constant wing surface area (S_{wing}) and the gravity acceleration (g). The variables presented are the m, ρ, and $C_{L,max}$. The $C_{L,max}$ and its corresponding angle of attack is dependent on the selected CONF.

$$V_{S_{1G}} = \sqrt{\frac{2\, m\, g}{\rho\, S_{wing}\, C_{L_{max,wing}}}} \tag{2.7.1}$$

The VFE is the maximum speed at which the aircraft can extend the flaps and slats at a particular CONF. In the case of CONF clean (0X0), the VFE is not defined since the flaps and slats are extended. Above each limiting speed and CONF, the stresses originating from the aerodynamic forces might lead to stresses beyond those allowed for the flaps' and slats' attachments.

The rest of the parameters that characterize the XV-15 are not represented in this study section for simplification reasons. An extensive characterization of parameters such as the mass properties (CG and inertial data), rotor aerodynamics, rotor-induced velocities, fuselage aerodynamics, wing-pylon aerodynamics, horizontal stabilizer aerodynamics, vertical fin aerodynamics, flight controls and SCAS, engines and energy storage units, landing gear, and drive systems is referred on supportive files, gathered by the global wrapper. The global wrapper takes protagonism in these study cases, where extensive tabulated data is found, establishing standardized interfaces and protocols for data retrieval and manipulation.

2.8.Reported Improvements During Flight Tests

The advanced proprotorcraft configurations, such as tiltwings and tiltrotors, still have a significant development margin improvement in terms of operational characteristics. In the case of the Bell V-22, the successor of the XV-15, some crucial topics have been declared to be of tremendous

development interest. These topics have not yet been solved, at least publicly, so they have been considered of interest to be documented in this study.

- The complexity of control laws might cause unforeseen stability problems and reduce the bandwidth and phase margin of the aircraft response. Consistent control strategies might be helpful in the Instrumental Meteorological Conditions (IMC) environments, unlike the Bell V-22 CLAWS, which does not incorporate this [5]. Conventionally, tilt-rotor aircraft face the requirements of changing the control strategies as the flight mode is changed from VTOL, transition, and airplane modes. It is to be checked if consistent control strategies can result in optimal control strategies for non-fixed environments such as shipboards.
- Some aircraft, such as the Bell V-22, have been reported to exhibit longitudinal accelerations when turning flight because of the inherent centrifugal accelerations, causing false indications and misconceptions about the steady state of the aircraft when turning [5]. It is considered that filtering centrifugal acceleration components would provide accurate longitudinal acceleration measurements.
- The transition phase leads to some of the highest handling qualities workloads from manned VTOL mechanisms. Auto-rotor-hub tilting can be automatically programmed to chase the ideal angles corresponding to airspeed and desired aircraft state. It has been disclosed that this system started to be developed during the operational life of the V-22, and flight tests have already been performed [5].

3. Performance Evaluation and Tuning of Proprotors

3.1. Analytical-Numerical Procedure

The relevant parameters of operation need to be identified to understand propeller performance. These parameters are the advancing speed, the proprotor rotational speed, and the Mach number at the blade tip. In addition, several geometrical quantities depend on the propeller: the number of blades, the diameter, the pitch, the airfoil at each section, the chord distribution, the tip geometry, and the hub geometry. An analytical-numerical medium-fidelity tool is presented, based on conventional BEMT models, nevertheless, without some limitations of this one generally employed due to mathematical complexity. The flowchart of the modules from the proposed tool is represented in Fig. 20.

At its core, BEMT offers a simplified framework for understanding the complex dynamics of fluid-structure interaction. This involves a dual decomposition: radial decomposition of blades and the fluid column and a conceptual separation between a macroscopic part, as per the Momentum Theory, and a local planar part, as per the Blade Element Theory. Essentially, BEMT relies on extracting 2D static data, particularly the lift and drag of each blade element considered. Typically, airfoil polar coefficients are provided as tabulated data, directly sourced from tools such as XFOIL [48], tabulated data of airfoils, or more precise methods such as in-plane CFD computations. The lift and drag of each element can be derived using these known aerodynamic coefficients, coupled with dynamic pressure and the element's chord. Generally, all the proprotor analytical-numerical 2D methods contain the following limitations:

- The flow is incompressible, inviscid, irrotational, and uniform
- There is a continuous flow velocity and pressure, except at the disk
- The airfoils through the blade do not interact between them, nor do the blades between them.

Conventional BEMT models, prevalent in literature and low-to-medium fidelity tools, are constrained by simplifications of the numerical process, typically addressed through iterative methods. These constraints involve the assumption that the out-of-plane velocity is significantly smaller than the in-plane, the presence of small, induced angles, and the drag coefficient is much smaller than the lift coefficient. In contrast, Stahlhut [26] proposed an alternative approach that abandons small angle assumptions, formally incorporates in-plane velocity components, and does not assume negligible drag compared to lift, thus avoiding linearized simplifications and iterative processes. Stahlhut's proposed method has not been validated against the conventional BEMT methodology nor validated against experimental data.

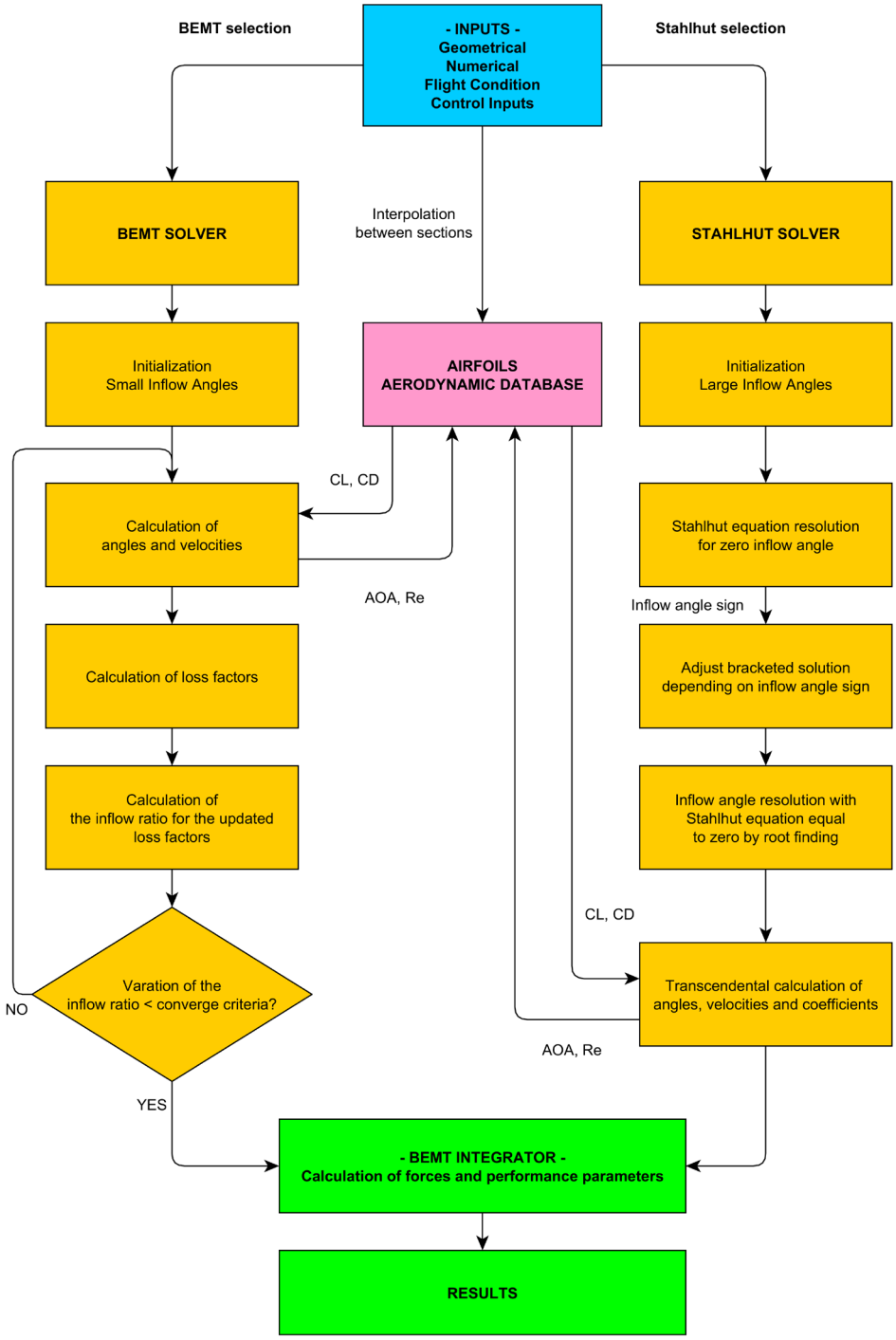

Fig. 20. Flowchart of the proprotor performance model

A set of non-dimensionalized parameters is defined and used to evaluate the proprotor system's performance results during the intermediate calculation process. The graphical determination of the convention is given in Fig. 21. These parameters ease the comparison of different geometrical proprotor configurations and define its behavior throughout multiple atmospheric conditions.

The relative position element (r), as given in (3.1.1.), is a parameter that defines the position of each blade section. r is hence used for integrating the performance parameters throughout the blade span. The parameter y defines the absolute position of the section, which is then normalized with the blade radius R. The root cutout is denominated as r_0.

$$r = \frac{y}{R} \tag{3.1.1}$$

The solidity (σ) is the ratio between the blade area projected on the rotor disk and the total rotor disk area. It serves as a crucial design parameter, with rotor coefficients frequently normalized by solidity to illustrate the concept of effective disk loading. N_b and c refer to the number of blades in the proprotor and the mean chord of the blade, respectively.

$$\sigma = \frac{N_b\, c}{\pi\, R} \tag{3.1.2}$$

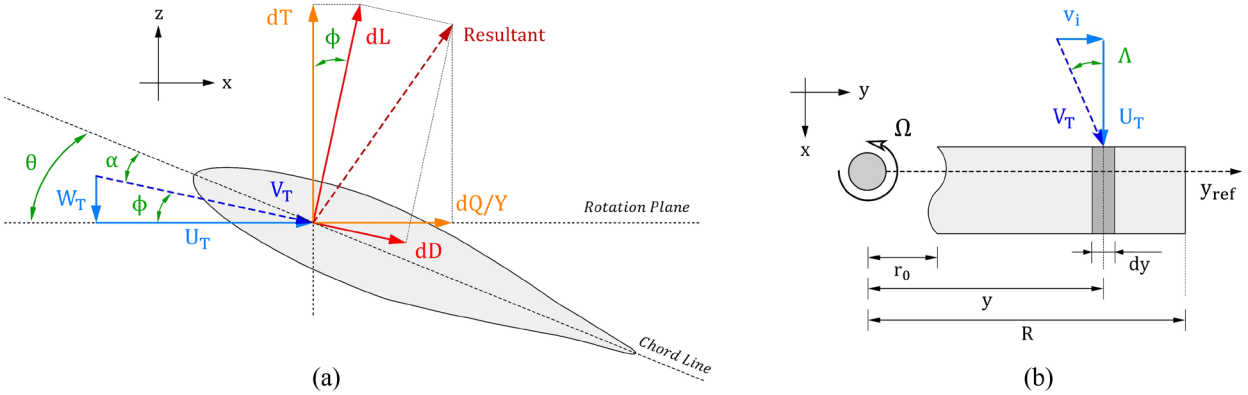

Fig. 21. Blade element convention for the numerical analysis from the lateral (a) and top view (b)

The in-plane or swirl velocity ratio (ξ) evaluates the flow speed parallel to the rotor. Orthogonally, the inflow ratio is defined as the ratio of the flow speed in the rotor-disk-plane (U_T) with respect to the blade tip speed (ΩR). This parameter is often not considered in conventional BEMT methodologies, as they neglect the in-plane velocities.

$$BEMT: \xi = \frac{U_T}{\Omega R} = \frac{\Omega y - u_i}{\Omega R} \tag{3.1.3}$$

$$STAHLHUT: \xi = r\frac{cos\,(\phi)}{g\,(\phi)} \tag{3.1.4}$$

The inflow ratio (λ) evaluates the flow speed normal to the proprotor disk. It is defined as the ratio of the normal flow speed to the rotor with respect to the blade tip speed. λ tends to increase with rotor disk angles of attack for helicopter configurations. It is one of the main parameters used in the iterative calculation process of conventional BEMT codes. The span-wise velocity (v_i) and its associated angle (Λ) is considered zero due to the assumption of non-interactions between blade elements.

$$BEMT: \lambda = \frac{W_T}{\Omega\, R} = \frac{V_\infty + w_i}{\Omega\, R} \tag{3.1.5}$$

$$STAHLHUT: \lambda = \xi\, tan\,(\phi) \tag{3.1.6}$$

The Stahlhut system cannot be solved analytically; hence, it must be solved numerically. The convergence of the system is not guaranteed due to the presence of nonlinear, transcendental equations. Two methods are recommended to solve the system:

- A fixed-point iteration scheme with a shallow relaxation factor to calculate the values of λ and ξ iteratively.
- To express the system in terms of ϕ and solve it using a bracketed method such as the bisection method, realizing that a single solution is located within a range between two points.

Defining that $\gamma = C_D/C_L$, and applying trigonometrical identities, two functions $B_1(\phi)$ and $B_2(\phi)$ are defined:

$$B_1(\phi) = \frac{V_\infty}{U} = sin(\phi) - \frac{1}{8\,K_T}\,\sigma\,\frac{1}{r}\,C_L\,sec(\gamma)\,csc|\phi|\,cos\,(\phi + \gamma) \tag{3.1.7}$$

$$B_2(\phi) = \frac{\Omega\,y}{U} = cos(\phi) + \frac{1}{8\,K_P}\,\sigma\,\frac{1}{r}\,C_L\,sec(\gamma)\,csc|\phi|\,sin\,(\phi + \gamma) \tag{3.1.8}$$

In this context, "γ" should not be confused with the aircraft flight path angle, which uses the same notation. The previous equations can be combined into a single transcendental equation, which is referred to as the Stahlhut equation:

$$g(\phi) = [B_1(\phi)\,\Omega\,y - B_2(\phi)\,V_\infty]\,sin(\phi) = 0 \tag{3.1.9}$$

$$g(\phi) = \left(\Omega y sin(\phi) - V_\infty cos(\phi)\right)sin(\phi) - sgn(\phi)\frac{\sigma C_L\,sec(\gamma)}{8r}\left[\frac{\Omega y}{K_T}cos(\phi+\gamma) + \frac{V_\infty}{K_P}sin(\phi+\gamma)\right] \tag{3.1.10}$$

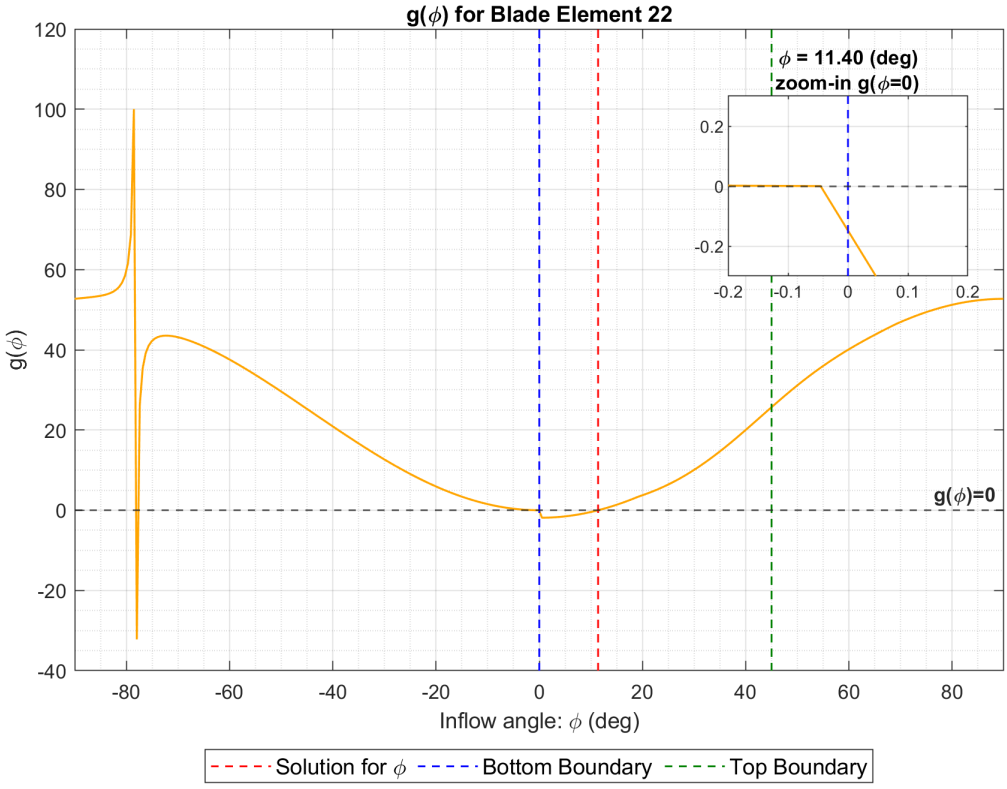

Fig. 22. Calculation of the inflow angle through the bisection method for a particular blade element

The sharp oscillation of $g(\phi)$ with respect to ϕ during its calculation, as given in Fig. 22, is due to the reach of a singularity section. In cases with an extensive range of inflow angles, multiple solutions to ϕ, one positive and another negative, might be found. To determine the correction solution, $g(\phi)$ is first calculated for $\phi = 0$. If $g(\phi) > 0$, then the ϕ is negative, whereas $g(\phi) \leq 0$, the ϕ is positive. The boundaries for the bracketed solution are adjusted accordingly.

The total velocity can be calculated in two different ways, depending on whether the conventional BEMT method or the Stahlhut-based methodology has been chosen. It can be observed how the differences rely on the in-plane velocity implementations, whereas the velocity normal to the rotor disk remains the same.

$$BEMT: dV_T = \sqrt{(V_\infty + dw_i)^2 + (\Omega\, dy)^2} = \sqrt{(d\lambda\, \Omega\, R)^2 + (\Omega\, dy)^2} \tag{3.1.11}$$

$$STAHLHUT: dV_T = \sqrt{(V_\infty + dw_i)^2 + (d\xi\, \Omega\, R)^2} = \sqrt{(d\lambda\, \Omega\, R)^2 + (d\xi\, \Omega\, R)^2} \tag{3.1.12}$$

Once the total velocities have been calculated, they are integrated into the main proprotor performance parameters. The equations governing the performance parameters are referred to in §1.2.4.

3.2. Corrections for the BEMT Numerical Process

Over the years, corrections have been introduced to address limitations and enhance predictive accuracy. Compressibility correction, Prandtl's tip-loss approach, and considerations for rotational effects have been added to ensure BEMT remains a reliable tool by accounting for real-world phenomena that might be oversimplified in the original theory. A graphical representation of these is given in Fig. 23.

- Compressibility correction becomes more relevant as the blades operate at high rotational speeds, making near-tip sections approach velocities near the sound speed. Lift and drag coefficients are corrected using the Karman-Tsien correction to account for the compressibility phenomenon.
- Rotational effects on the blade, associated with the three-dimensionality of the phenomena and radial airflow, are not considered in the original BEMT. Chaviaropoulos and Hansen proposed a semi-empirical method to address rotational effects, initially developed for wind turbines but also applicable to propellers.
- Prandtl's tip-loss approach addresses performance variations near the blade tip. This factor penalizes the performance of blade sections, especially those near the tip, ensuring a more accurate representation of real-world conditions.

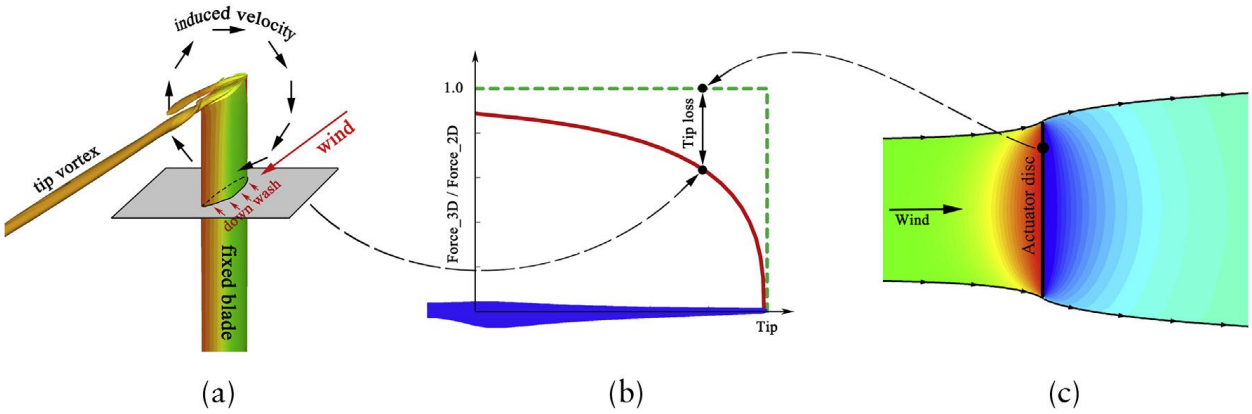

Fig. 23. (a) Downwash generated by the tip vortex, (b) aerodynamic force ratio 3D/2D, and (c) flow field of an actuator disc contoured by pressure [49]

High local inflow at the tip of the blades due to trailing vortices leads to the reduction of lift in the tip. This phenomenon accentuates the need to account for these 3D effects based on a 2D method. The correction factor is denominated as F.

$$F = \left(\frac{2}{\pi}\right) cos^{-1}\left[exp\left(\frac{N_b(r-1)}{2\,r\,sin\,(\phi)}\right)\right] \tag{3.2.1}$$

The tip-loss correction factor for the small angle approach is incorporated into the conventional BEMT methodology as:

$$dC_T = 4\,F\,\lambda\,(\lambda - \lambda_c)\,r\,dr \tag{3.2.2}$$

The inflow velocity becomes affected by the introduction of the previously defined loss factor F:

$$\lambda(r,\lambda_c) = \sqrt{\left(\frac{\sigma\,C_{L_\alpha}}{16\,F} - \frac{\lambda_c}{2}\right)^2 + \frac{\sigma C_{L_\alpha}}{8F}\theta r} - \left(\frac{\sigma\,C_{L_\alpha}}{16\,F} - \frac{\lambda_c}{2}\right) \tag{3.2.3}$$

An iterative process starts until the loop satisfies the predetermined requirements. A maximum number of loops and convergence criteria should be established as a general computational approach.

$$F = f(\phi) = f(\lambda) \tag{3.2.4}$$

The methodology for the large-angle approach remains the same as that of BEMT, but the system is more complex mathematically. The thrust and the power coefficient equations take the following form.

$$dC_T = \frac{1}{2}\,\sigma\,\sqrt{\xi^2 + \lambda^2}\,(C_L\,\xi - C_D\,\lambda)\,dr = 4\,K_T\,|\lambda|\,\lambda_i\,r\,dr \tag{3.2.5}$$

$$dC_P = \frac{1}{2}\,\sigma\,\sqrt{\xi^2 + \lambda^2}\,(C_L\,\lambda + C_D\,\xi)\,r\,dr = 4\,K_P\,|\lambda|\,\xi\,r^2\,dr \tag{3.2.6}$$

Where K_T and K_P are the in-plane and out-of-plane loss factors, respectively.

$$K_T = 1 - (1 - F)\, cos\, (\phi) \tag{3.2.7}$$

$$K_P = 1 - (1 - F)\, sin\, (\phi) \tag{3.2.8}$$

The loss factor is taken from the previously defined equation of the loss factor for the large angle of approach, which is a function of input systems and the inflow angle. Therefore, an iterative process, unlike the BEMT approach, is unnecessary.

4. System Configuration and Analysis of Capabilities

4.1. Computational Modules

Intending to have a full view of how the flight dynamic model is structured and how the objective and task take form, a top-level view of the model is represented in Fig. 24. The inputs of the flight dynamic model are the MITL / Batch Execution, Aircraft Specific Data, and the Initial States. The Frame of Work encompasses flight mechanisms and system modeling, equations of motion integration, and the atmospheric model. The frame of work is constructed to integrate with potential future development of the sensor models and flight control system, which can be integrated with current studies at KTU and the aircraft-specific data characteristics. The results of the flight dynamic model, considered as the interaction between the initial and updated states vectors, are evaluated in terms of aircraft performance and handling qualities.

The study is performed on a computer simulation frame of work without specifically doing the author's field tests or laboratory experiments. This decision is considered to use existing field and laboratory data and concentrate the working load on the flight dynamic model itself.

The MATLAB programming environment is used as the root modeling software. In constructing the model, careful consideration is given to the possibility of future transfer to other commonly used languages in the industry, such as Python. The utilization of specific software tools is minimized to the greatest extent possible to facilitate translations to different languages.

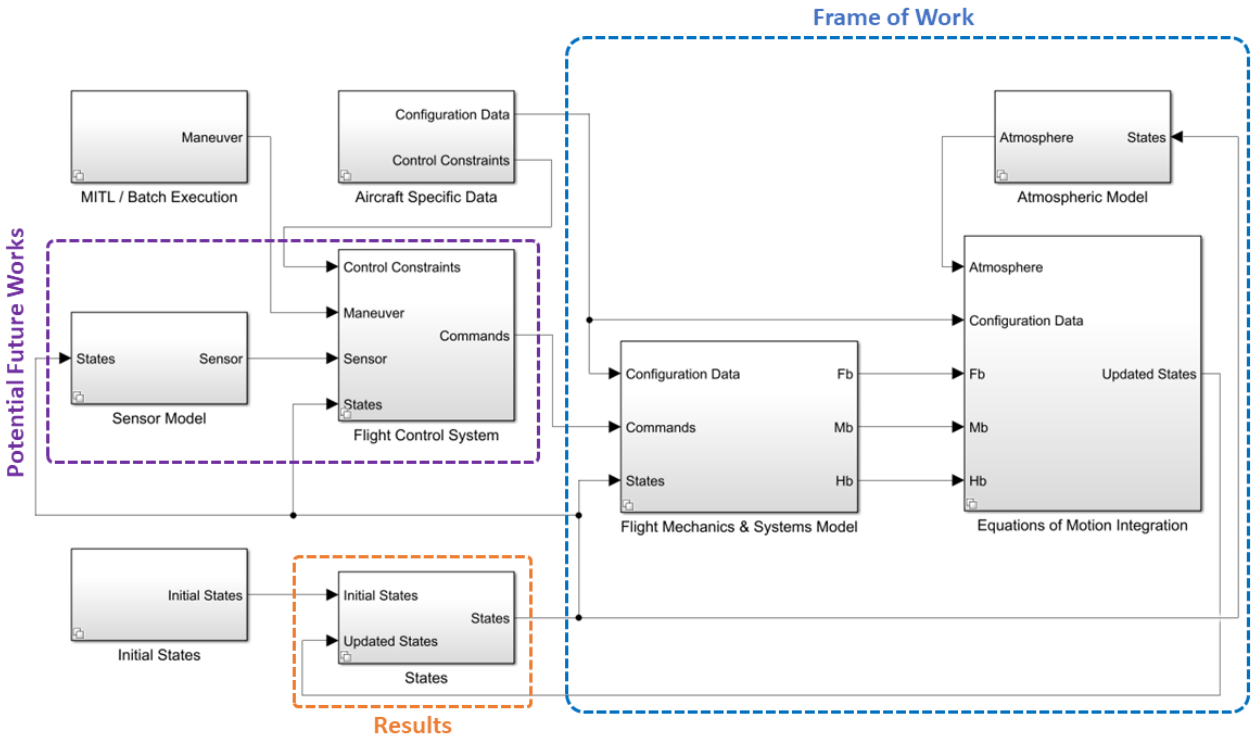

Fig. 24. Top-level flight dynamic model

Additional detail level of each model block from Fig. 24 is detailed next:

- **MITL / Batch Execution**: The maneuvers to be executed are considered in terms of Man In the Loop (MITL), the live-simulation method, or in Batch Execution, which is the mode where a maneuver is defined through an algorithm. Usually, the MITL mode takes action on

the aircraft's power and control surfaces, while Batch executions can proceed in that way or by defining a trajectory. The action frame of this project is to work in batch execution, which should be modeled before a generally more complex MITL system. Additionally, Batch Execution might be applicable as the final maneuver model for unmanned aircraft.

- **Aircraft Specific Data**: The primary information about which aircraft is evaluated is stored in the Aircraft Specific Data block. This block considers information such as aerodynamic coefficients, powerplant characteristics, landing gear properties, and mass properties as configuration data. Even though the results from the flight dynamic model might affect the configuration data of the aircraft, it is not shown in the represented diagram for simplification purposes. The control laws, flight envelope and corridors, and configuration data limitations are considered the Control Constraints. Limitations from the configuration data are considered inside the Control Constraints, such as the maximum time at which a maximum thrust can be demanded. The aircraft-specific data is retrieved through a global wrapper, which takes the information needed for the consecutive blocks.
- **Initial States**: Since the simulation might not always be desired to start with the aircraft on the ground at zero speed and an altitude such as sea level (SL), some initial states are considered inputs for the simulation. Inside of the initial states, the 12 states variables are considered: three positions with respect to the earth-fixed system, three linear velocities, three Euler angles, and three Euler rates.
- **Flight Mechanics & Systems Model**: this block considers the propulsion, ground-reaction, and actuator models, among other preliminary calculations. This block outputs the general aircraft's net forces and momentum and the rotating systems' angular momentum. In other words, this block models the characteristics of each system in an isolated manner, which are then delivered to the equations of motion integration block for coupling and translation to the aircraft body axis.
- **Equations of Motion Integration**: the preliminary calculations from the Flight Mechanics & Systems Model block are integrated and transferred to the body axis system. The atmospheric model feeds the block to tune the calculations from the static perspective, as a pressure altitude difference can be dynamic due to the wind gusts and turbulence models. This block outputs the updated state vector throughout and at the end of the imposed maneuver, which is then used to analyze the results of the flight dynamic model. Modifications and transients from the aircraft configuration data, such as time derivatives from the inertial matrix, are considered.
- **Atmospheric Model**: The atmospheric model encompasses the atmospheric characteristics in the frame of the International Standard Atmosphere, wind, gusts, and turbulence models.
- **Sensor Model**: the sensor model block intends to deliver further information regarding state vectors to the flight control system. Examples of usage are the positioning of the aircraft by a radar, accelerations through accelerometers, and failure of systems, among others.
- **Flight Control System**: the FCS block englobes the CLAWS, fed by the specific aircraft control constraints, the maneuver inputs, the sensor feedback information, and the current state vector. The FCS then outputs a corrected or manipulated version of the maneuver, depending on the inputs previously mentioned. This block's implementation invokes the figure of a closed-loop control system, which is undoubtedly necessary for successful operations.

The model is fed with inputs through a global wrapper, commonly denominated as simulation executive (SE). The SE acts as the conductor of the simulation, with goals such as organizing model execution, linking peripheral devices, ensuring hardware compatibility for MITL simulations, portability across platforms, and ride-along capability. During batch mode, the SE supports data storage, retrieval, and manipulation for analysis. However, during the MITL simulation, the SE aims to create a realistic flight experience through real-time aircraft and its subsystems' responses, which can store the information for post-simulation analysis.

4.2. Definition of the Proprotor System

The proprotor system is defined primarily by the number of blades, the radius, root cutout, the chord and twist vector, and the airfoil determinations throughout the blade span. This section's classical representation of these parameters is adapted to the reference ASD in Fig. 25. The geometrical twist, also called the chord line angle, is defined as the pitch measured from the chord line to the rotational plane. The collective is neglected in the definition of the geometrical twist, which would normally be considered the rest position. The chord has been presented in absolute values, even though some authors might represent it as the ratio between the chord value and the radius of the rotor blade. The root cutout is the position at which the blade is considered to start, measured from the center of rotation. It aims to mitigate potential reverse flow effects near the root since the region is over the hull.

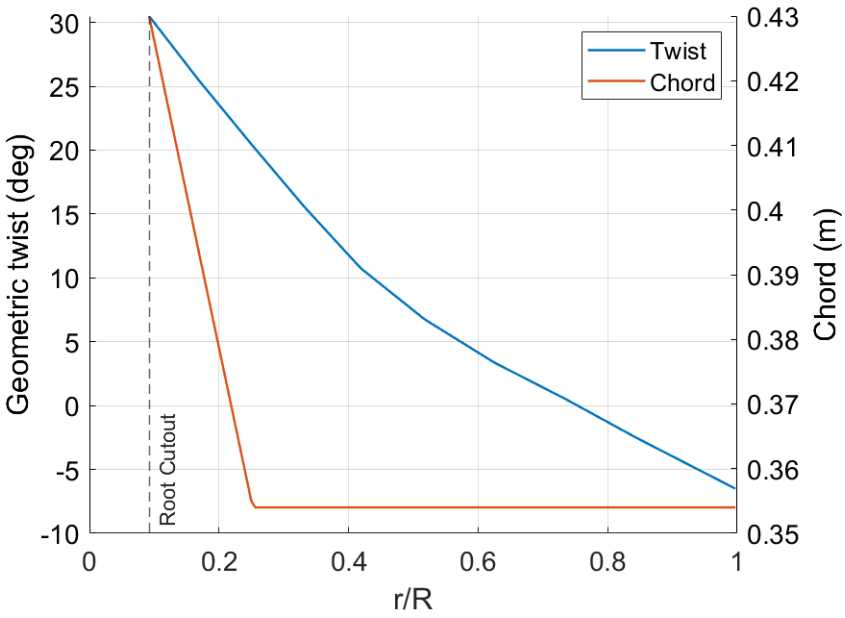

Fig. 25. Geometric twist and chord of the blade

The coordinates of NACA profiles and other normalized airfoils can be generated with relatively simple codes. The blade span, as well as other non-rotary wings, are generally composed of multiple airfoils. In the case of rotary wings, higher thickness-to-chord ratios are found closer to the root since the total velocity at the section is considerably lower than at the tip. Additionally, higher bending moments appear closer to the root, hence the need to increase the inertia modulus to compensate for these mechanical loads. The representation of the airfoil profiles for the reference ASD and their relative position is given in Fig. 27.

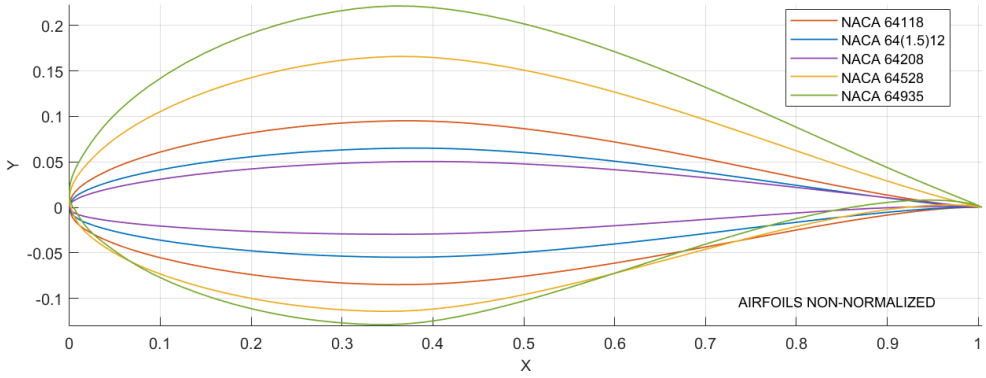

Fig. 26. Blade's airfoils representation

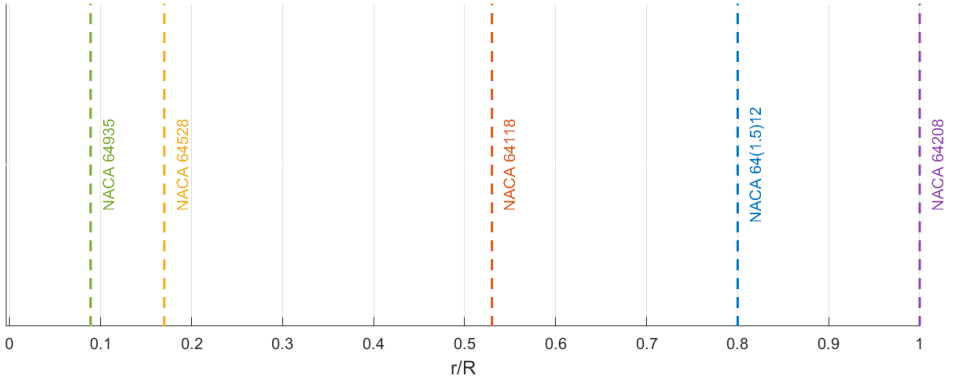

Fig. 27. Airfoils' relative positions throughout the blade span

Linear interpolation between the airfoil aerodynamic coefficients at sections between the exact positions for each might be performed. In this way, blade section polars are taken directly from the original database of each airfoil for those blade elements that contain the r/R position inside of its domain. This methodology would give each blade section a unique polar data frame, considering there are no identical consecutive airfoils. In the tool's current development version, just one airfoil at a time can be considered for the whole blade span. For simplification purposes, only the airfoil polars for the profiles NACA 64(1.5)12 are presented in Fig. 28.

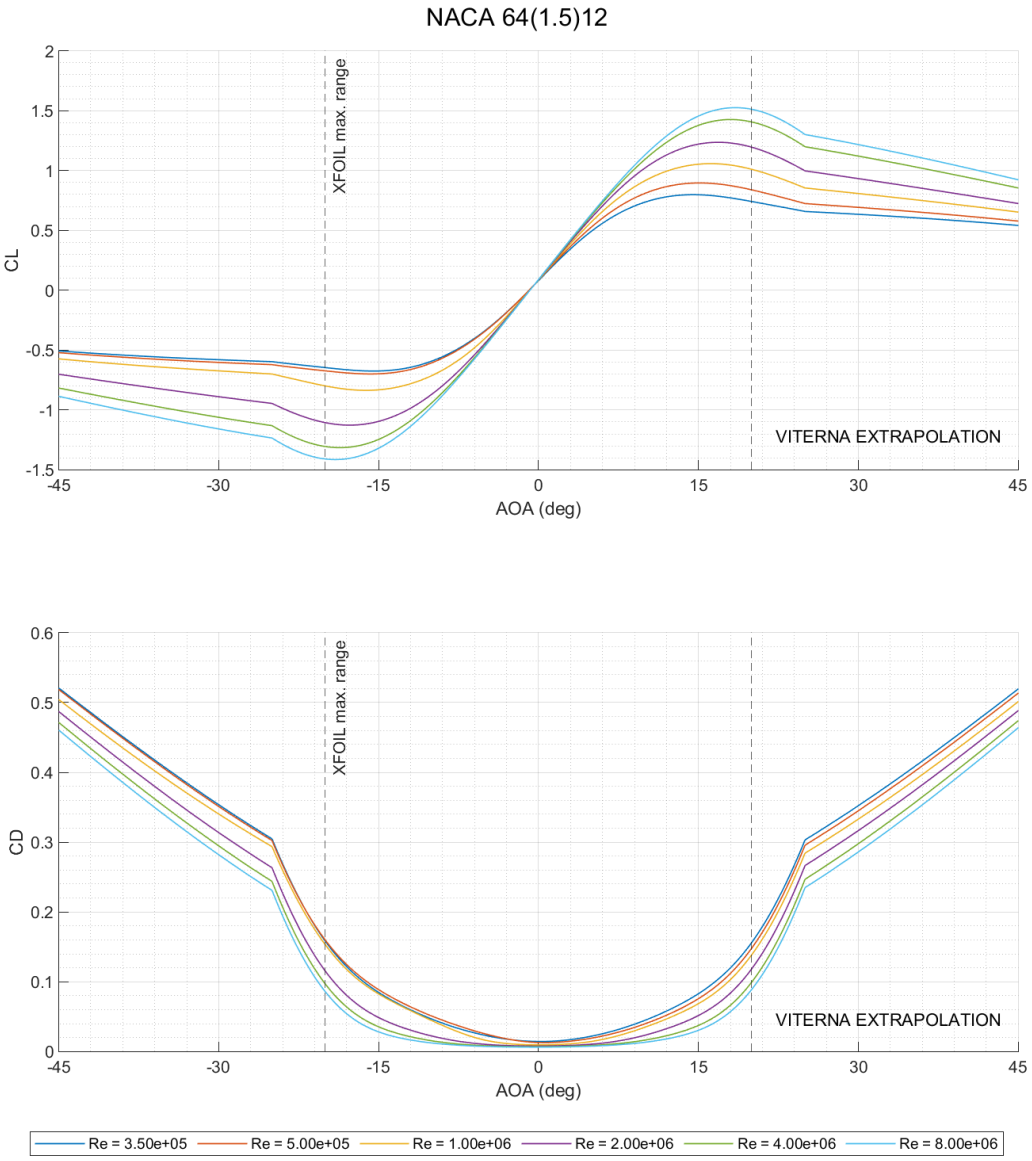

Fig. 28. NACA 64(1.5)12 aerodynamic coefficients at multiple Re and AOA

The airfoil aerodynamic coefficients, considering attached flow conditions and various other limitations, are recommended to be generated by the free-use XFOIL [48] program. The profiles with higher thickness-to-chord ratios present difficulties using this program to achieve the aerodynamic coefficients. Additionally, these airfoils are placed at the blade's lower speed region, accentuating the deattached flow phenomena. A smoothing method is recommended to compensate for some of the inaccuracies of the polar generation. During the creation of the presented tool, two smoothing functions are introduced, the "sgolay" and the "lowess". The Savitzky-Golay function removes noise by fitting polynomials over a sliding window, while the "lowess" adapts to local variations using weighted polynomials. Both functions are available in MATLAB and Python through different libraries.

The airfoil aerodynamic coefficients have been extrapolated beyond the XFOIL limits to account for high angles of attack, which might be found close to the root and a high-speed flight. There are several stall delay models to take the dynamic stall effects into account, among the most used ones are the Viterna-Corrigan post-stall model [50] and the Corrigan-Schilling [51] stall delay model. The first of the extrapolation models is available in the free-use QBLADE program, which was used

to perform this particular task. The empirical Viterna-Corrigan model takes as inputs the lift and drag coefficient at the stall, the angle of attack that initiates the stall, and an imposed maximum drag coefficient in the fully stalled regime, generally defined at 90 degrees. Without additional data, a value of 1.8 shall be imposed on the drag coefficient at 90 degrees.

4.3.Static Thrust Evaluation and Sensitivity Analysis

The static thrust is defined as zero forward speed related to the hovering or take-off phases. Hover performance is critical to analyze since it usually determines the aircraft's maximum payload, especially in vertical flight operations. Additionally, the maximum thrust available in the case of proprotors is generally encountered for the flight condition of zero velocity. Further details about this last statement are described in later sections of this project.

The results of this section are compared with the bench tests performed by NASA at the Ames Research Center in the frame of the XV-15 Research Program, Technical Memorandum 86-833 [52]. The proprotor physical definition is the one described in §4.2. The tests were conducted outdoors, without aerodynamic interference from other elements, and out of ground effect. The test rig and its supporting structure provide negligible blockage of the rotor wake, as given in Fig. 29. It has been reported that the proprotor is sufficiently separated from the ground to be considered out-of-ground effect (OGE).

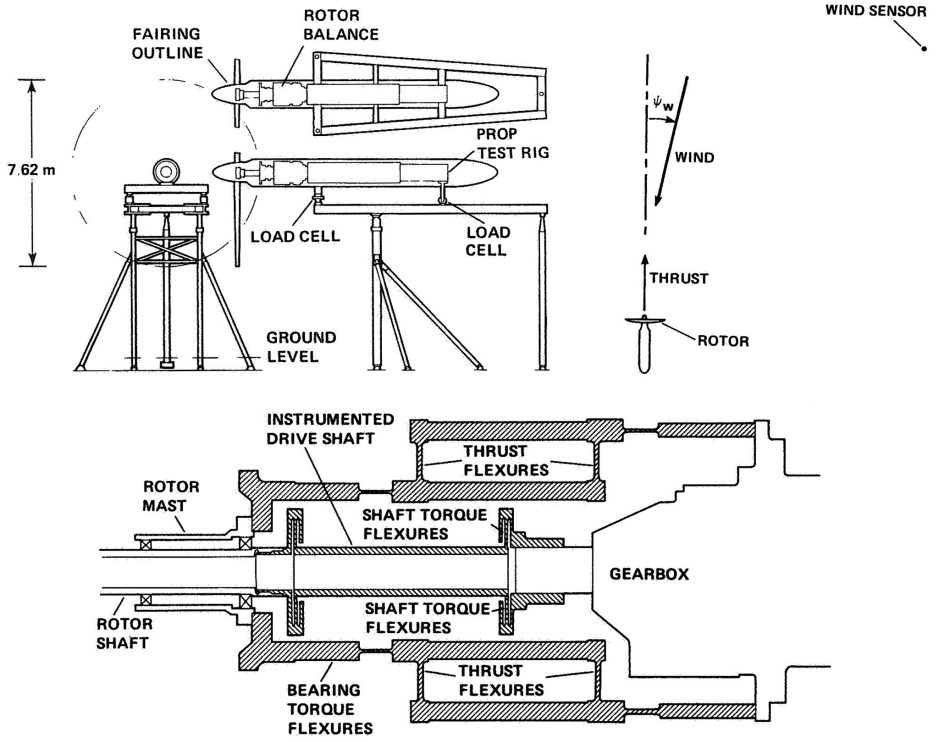

Fig. 29. Experimental proprotor bench test rig, wind sensor location, and loads balance system [52]

The thrust balance is accurate within $\pm 0.1\%$ error up to $50\ kN$, with no significant interactions caused by other forces or moments. The instrumented drive shaft torque is accurate to within $\pm 0.3\%$ error up to the maximum capacity of $28.5\ kNm$. The tests have been performed with winds equal to or less than $1.5\ m/s$. The measured rotor torque has been corrected for the effect of wind using an empirical momentum theory-based correction procedure, for which further detail is available in the referred Technical Note. The magnitude of the correction during the performed

tests, at less than 1.5 m/s, is below 3%. This correction percentage is denominated in this document as WACP: Wind Adjusted Power Coefficient.

The tests have been grouped into RPM sets with values of 511, 553, 565, 586, and 624. The data has been grouped so that the maximum deviation is 4 revolutions, which is considered to have a negligible effect on the results. The number of data points for each set of RPMs is 7, 4, 4, 168, and 8, respectively. Therefore, the population is considered enough for statistical analysis, just for the RPM set 586. The results of the validation loop are given for the BEMT and the Stahlhut solvers in Fig. 30 and Fig. 31, respectively.

Considering an average air density value of 1.235 $\mathrm{kg/m^3}$, an equivalent pressure altitude (ZP) of -80 m has been configured for all the model computations. The progression of C_T and C_P is achieved by increases in the collective, which is aligned between the experimental and the model configuration in the case of the Stahlhut solver. For the BEMT solver, higher collective angles have been needed to match the C_P values.

A second-order polynomial equation, graphically represented by the name "Fitting Curve", adjusts the error of ΔC_T throughout the C_P range. Fitting the error of ΔC_T with such a methodology, might not capture the physical meaning of the errors between the model and the experiments. However, this fitting curve is considered useful for a smooth adjustment of the model results once the experimental data is known. General parameters, such as the absolute average, standard deviation, and variance, are automatically calculated for the statistical evaluation purposes of these deviations.

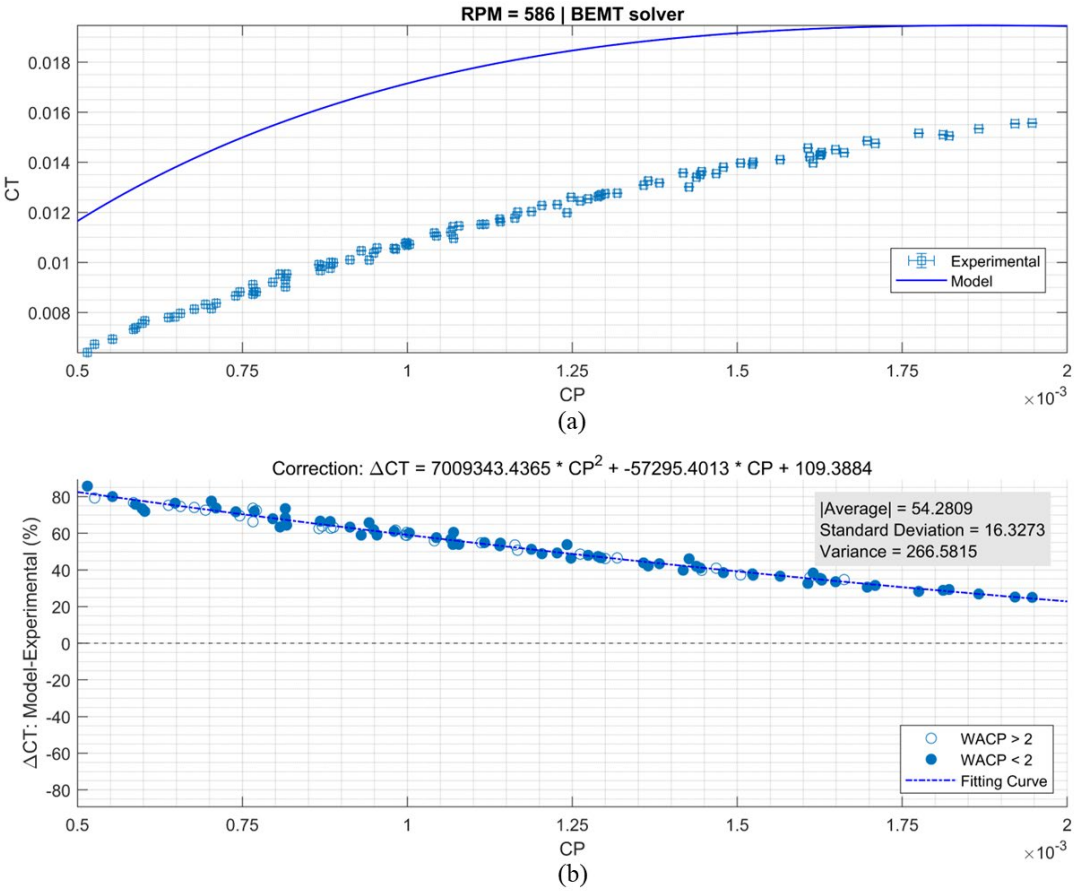

Fig. 30. Model and experimental C_T versus C_P absolute (a) and difference (b) results for the BEMT solver

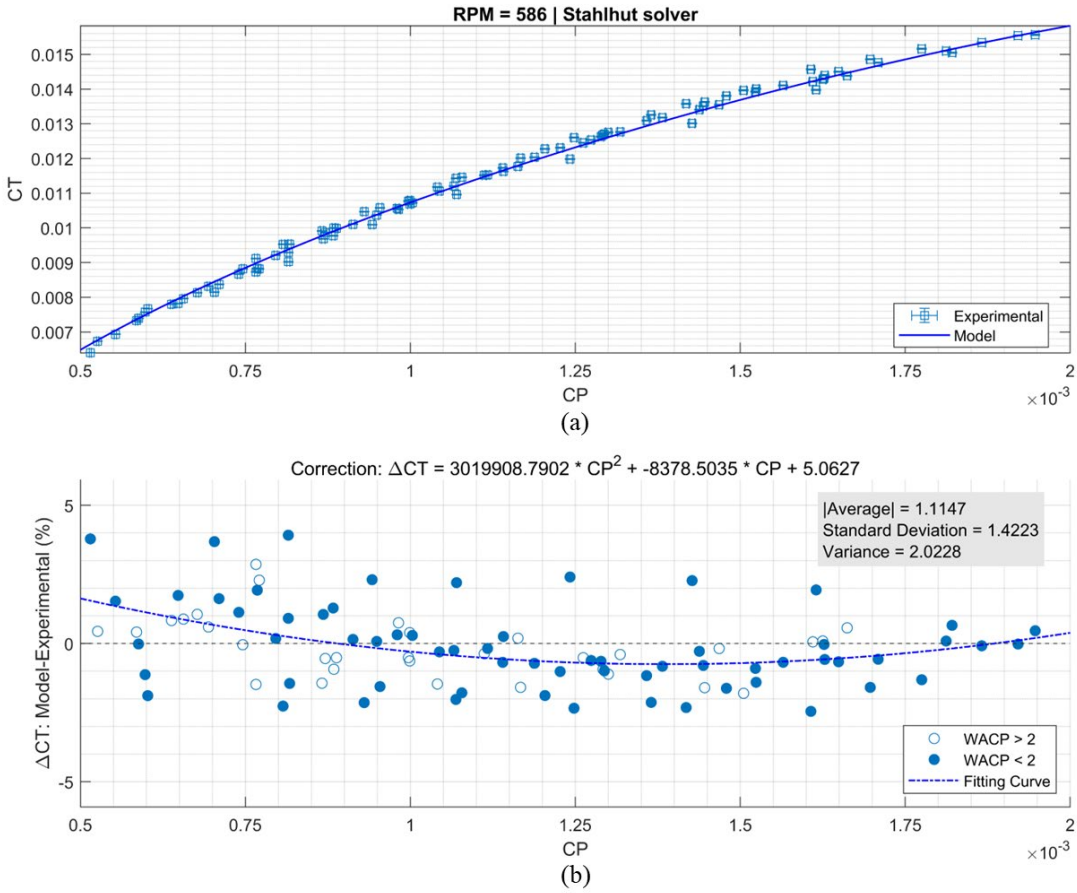

Fig. 31. Model and experimental C_T versus C_P absolute (a) and difference (b) results for the Stahlhut solver

The probability density distribution (PDD) becomes a valuable method to analyze the likelihood of a particular ΔC_T, to be found at each RPM setting. The area enclosed by each probability density curve, the maximum values, and the relative position with respect to ΔC_T are presented in Fig. 32 and Fig. 33 for the BEMT and the Stahlhut solver, respectively.

The similarity in the shape of the PDD curves for the BEMT solver suggests that the performance of this solver is relatively consistent across different RPM settings. The wider range of ΔC_T values for the BEMT solver, from 20 to 88%, compared to the Stahlhut solver, from -3 to 4%, clearly represent the error ranges between the small and the large inflow angle modeling approaches. The deviations' order of magnitude is similar to previous studies, also based on the Stahlhut methodology, for the same proprotor, with RMS errors of 6.16% between the C_T and C_P for tip-Mach 0.6 (RPM = 586) [53]. The previously mentioned reference has not validated the other RPM settings. Additionally, the algorithm configuration was not disclosed, making it difficult to compare the approach of this project and the mentioned reference.

The results suggest that the BEMT solver tends to be more precise than the Stahlhut solver, but this second one is notoriously more accurate. Looking toward the implementations of these numerical-analytical methodologies, BEMT could be recommended to analyze trends in the design changes of proprotors. In contrast, the Stahlhut solver could be more suitable for quantifying the performance values of each design in the subsequent design validation loops.

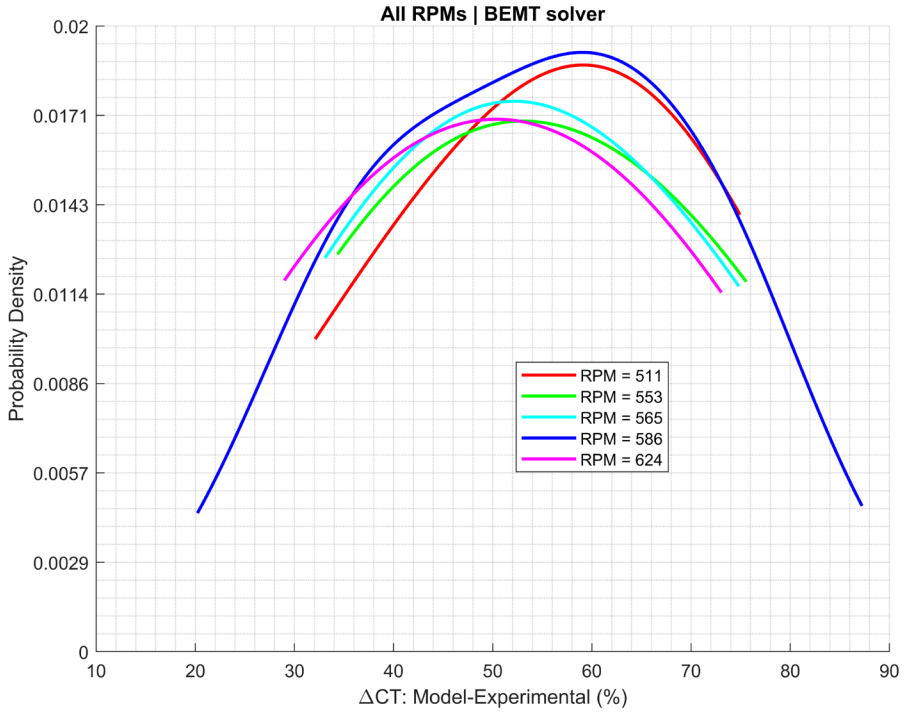

Fig. 32. PDD compilation between the model and experimental results for the BEMT solver

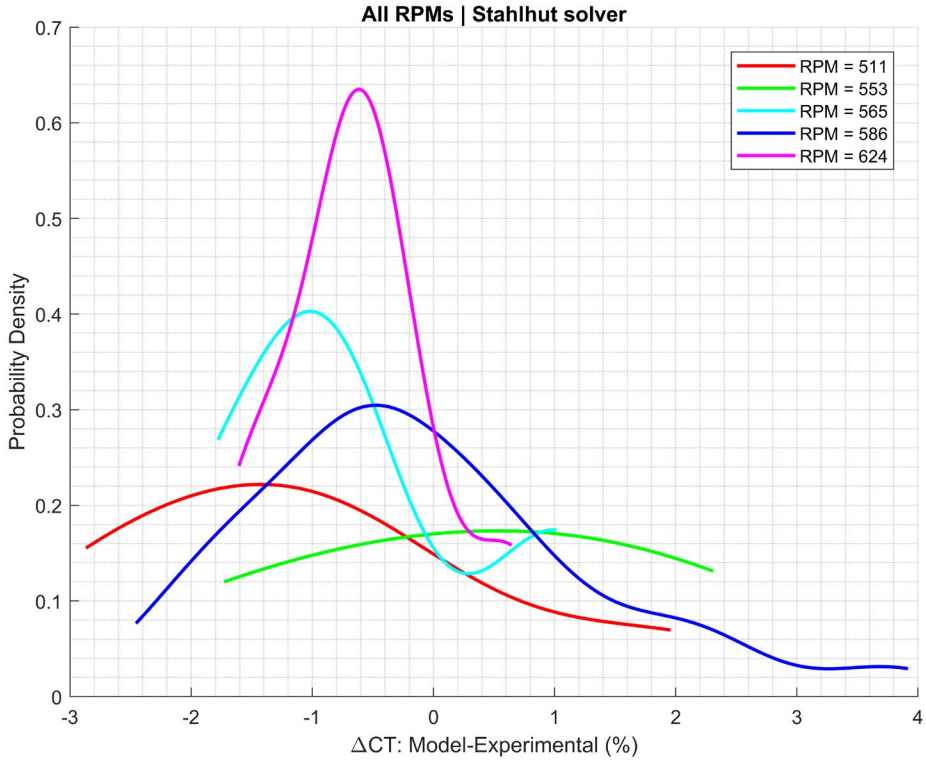

Fig. 33. PDD compilation between the model and experimental results for the Stahlhut solver

A detailed analysis is performed throughout the relative positions of the blade span for some of the most characteristic aerodynamic and performance parameters in Fig. 54, which is available in the appendix. The analysis is done between the Stahlhut and the BEMT solvers at RPM 586 for collective angles of 5 and 21º. These collective angles are selected because they correspond approximately to $\Delta C_T = 0$ for the fitting line between the Stahlhut solver and the experimental data.

The progression of the parameters is consistent between both collective angles: a tendency for higher effective angles of attack, lift, drag, thrust, and power coefficients throughout the blade span. However and as previously commented, higher collectives are needed in the BEMT solver to achieve the same C_P value as in the Stahlhut, especially at the highest values.

Overall, the Stahlhut solver is more conservative than the conventional BEMT, especially closer to the tip and at higher collective angles. In other words, higher C_P and lower C_T tend to be found when considering the allowance for the large inflow angles approach. Except for the induced velocity, the rest of the parameters tend to maintain a certain parallelism between the BEMT and the Stahlhut results. The Reynolds throughout the blade span for both solvers and collective angles remain practically unchanged, as the primary contributor to this parameter is the angular velocity, which is fixed for this analysis.

The trade of proprotor design to comply with the characteristics of helicopter and airplane mode can be observed by attending to the overshoot of the dC_D closer to the center of rotation. Large angles of attack are found in this region, which represents the desire to have relatively constant light throughout the blade to avoid undesired deformation profiles and maximize the trade of average C_T/C_P values for the low and high-speed regimes. Additionally, a variable-speed gearbox would reduce power requirements by lowering blade dynamic pressure and a non-uniform thrust distribution, enhancing aerodynamic improvements.

Conventional BEMT solvers tend to have a linear progression of deltas between experimental and model results. These models are not recommended in the case of tiltrotor configurations, which possess great twist and speed gradients from root to blade tip. These conventional methodologies might be considered interesting if low computational costs are desired and analysis of trends-differences between different proprotor geometrical configurations and operational conditions are desired. The absolute values of the proprotor performance would lead to misleading conclusions in the case of proprotor configurations such as the ones considered in this study.

4.4. Aircraft Flight Dynamics Modelling

4.4.1. Structure of the Model

The developed algorithm tool for finding the trimming parameters for each desired flight state has been constructed on the longitudinal dynamics frame. The lateral and rolling dynamics are neglected, i.e., no rolling or yawing motion. As a result, the effects of control surfaces, such as the rudder and ailerons, are not implemented. The algorithm is controlled by changes in the magnitude (T) and direction (β_{RH}) of the thrust vector, as well as the deflection of the elevator (δ_{ELEV}).

The free-body diagram representing the loads on the longitudinal solid-rigid aircraft is presented in Fig. 34. The earth axis is presented with the vectors of North (N) and Down ($-D$), according to the standards convention. The aircraft axis system is presented by the axial (X_B) and the vertical (Z_B) vectors. The lateral vector (Y_B) is not presented in the diagram, but it is considered to point to the right, as viewed from top-to-bottom of the airplane. The angles of attack, pitch, and flight path angles are represented by the letters α, θ, γ, respectively, following standard conventions.

The distance between the wing aerodynamic center (AC) and the CG is given by the parameter "L_{CGAC}". This distance is considered constant and defines the aircraft's Static Margin (SM). The

distance between the HRST AC and the CG, also known as the tail arm, is also considered constant, and it is given by the sum of the L_{CGAC} and L_{HRWN}. Minor simplifications are considered, such as imposing that the vertical distance from the horizontal stabilizer (HRST) to the wing (WING) and from the WING to the Center of Gravity (CG) be zero. The incidence angle of the horizontal stabilizer total plane (i_{HRST}) is considered zero, as it would be generally used to trim the airplane at an equivalent deflection of δ_{ELEV}.

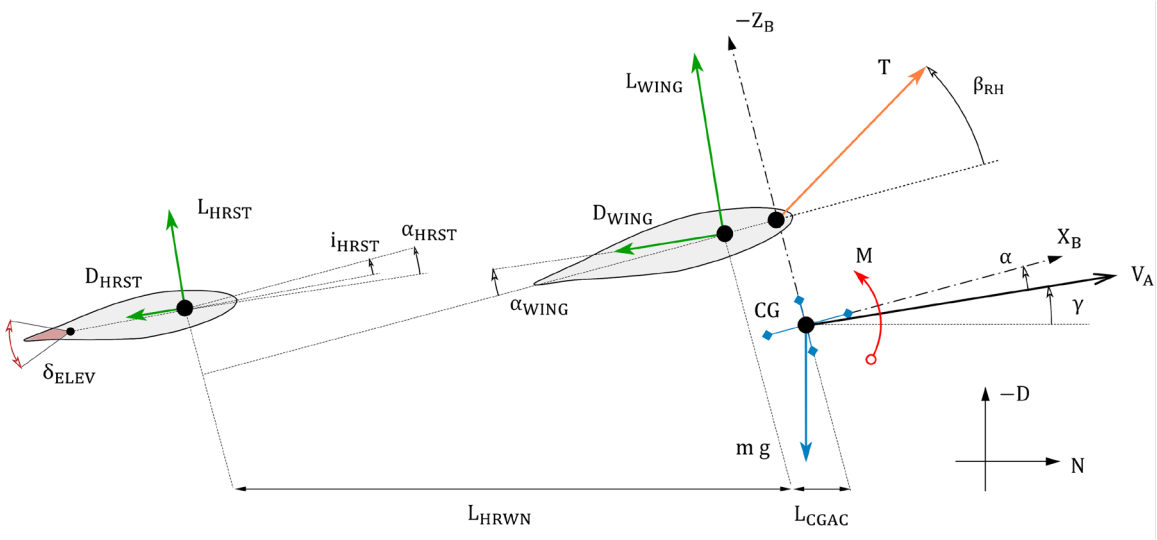

Fig. 34. Free Body Diagram in the aircraft body XZ plane

The "lsqnonlin" function, pre-configured with the Levenberg-Marquardt algorithm, seeks to minimize the sum of squares of the differences between computed and desired state derivatives. The "fsolve" function then refines the initial guess for trim parameters iteratively until a solution is found. Both mentioned functions are MATLAB built-in optimization algorithms, which can be associated with functions available in programming languages such as Python throughout the usage of libraries. The final values of the objective function are limited by predefined tolerances, which trigger warnings for potential unconvergence issues. Once the computation loop is successfully converged, a particular set of resulting trim control variables characterize the flight state condition.

The lift and drag equations are calculated for each aerodynamic surface generating loads on the body axis. Each of these surfaces is referred to as an item. For each of the evaluated items, some data frames store the aerodynamic coefficients. Other necessary parameters, such as the reference surface of the item (S_{ITEM}), or the distances from the aerodynamic center of each item to the aircraft CG are defined.

$$L_{ITEM} = \frac{1}{2}\,\rho\, S_{ITEM}\, V_{A_{ITEM}}^2\, C_{L_{ITEM}} \tag{4.4.1.1}$$

$$D_{ITEM} = \frac{1}{2}\,\rho\, S_{ITEM}\, V_{A_{ITEM}}^2\, C_{D_{ITEM}} \tag{4.4.1.2}$$

$$L_{TOTAL} = L_{ITEM_1} + L_{ITEM_2} + \cdots + L_{ITEM_n} \tag{4.4.1.3}$$

$$D_{TOTAL} = D_{ITEM_1} + D_{ITEM_2} + \cdots + D_{ITEM_n} \tag{4.4.1.4}$$

Four main aerodynamic surfaces are considered: the wing, the horizontal stabilizer, the vertical stabilizer, and the fuselage. Due to the absence of further reported OEM data for the ASD, the following simplifications are performed:

- The fuselage does not provide any lift. This assumption is considered not to impact the performance results significantly, as the main contributors to the lift are the wing and the horizontal stabilizer.
- The fuselage drag is considered equal to 45% of the wing drag. Conventional fixed-wing airplanes would have a fuselage drag of around 30% with respect to the wing. However, tiltrotor aircraft, such as the case of the studied ASD, have a fuselage frontal area considerably bigger than the wing. Additionally, the fuselage is not as streamlined as conventional airplanes due to a bulky and exposed belly fairing for storing the landing gear.
- The vertical stabilizer does not provide any lift. This assumption does not impact the performance results since no rolling or sideslip angles are considered.
- The vertical stabilizer drag coefficient is considered constant. This assumption is considered not to impact the performance results, as this parameter is generally not dependent on the angle of attack. Additionally, no rolling or sideslip angles are considered.

The longitudinal linearization coefficients are derived from the equations representing the force and moments on the body axis system. These coefficients capture the sensitivity of these forces and moments to deviations from the trim state. The forces are represented due to the effect of horizontal velocity (u), vertical velocity (w), pitch rate (q), elevator control input (δ_e) and thrust control input (δ_T). The input parameters are described as follows.

If: S − Wing reference area (m^2);

c − Wing MAC (m);

C_{x_0} − Aircraft drag coefficient at zero AOA;

C_{x_α} − Rate of change of aircraft drag coefficient (rad^{-1});

T_{max} − Maximum thrust available (N);

C_{z_0} − Aircraft lift coefficient at zero AOA;

C_{z_α} − Rate of change of aircraft lift coefficient (rad^{-1});

C_{m_0} − Aircraft pitch moment coefficient at zero AOA;

C_{m_α} − Rate of change of aircraft pitch moment coefficient (rad^{-1});

C_{m_δ} − Rate of change of aircraft pitch moment coefficient, with respect to elevator deflection (rad^{-1}).

The linearization of loads on the body X-axis (X_B), are evaluated according to:

$$X_u = \frac{u_{trim}\,\rho\,S}{mass}\left(C_{x_0} + C_{x_\alpha}\,\alpha_{trim}\right) - \frac{\rho\,S\,w_{trim}\,C_{x_\alpha}}{2mass} \tag{4.4.1.5}$$

$$X_w = -q_{trim} + \frac{w_{trim}\,\rho\,S}{mass}\left(C_{x_0} + C_{x_\alpha}\,\alpha_{trim}\right) + \frac{\rho\,S\,u_{trim}\,C_{x_\alpha}}{2\,mass} \tag{4.4.1.6}$$

$$X_q = -w_{trim} \tag{4.4.1.7}$$

$$X_{\delta_e} = 0 \tag{4.4.1.8}$$

$$X_{\delta_T} = \frac{1}{mass}\,T_{max}\,cos\,(\beta_{RH}) \tag{4.4.1.9}$$

The linearization of loads on the body Z-axis (Z_B), are evaluated according to:

$$Z_u = q_{trim} + \frac{u_{trim}\,\rho\,S}{mass}\left(C_{z_0} + C_{z_\alpha}\,\alpha_{trim}\right) - \frac{\rho\,S\,w_{trim}\,C_{z_\alpha}}{2\,mass} \tag{4.4.1.10}$$

$$Z_w = \frac{w_{trim}\,\rho\,S}{mass}\left(C_{z_0} + C_{z_\alpha}\,\alpha_{trim}\right) + \frac{\rho\,S\,u_{trim}\,C_{z_\alpha}}{2\,mass} \tag{4.4.1.11}$$

$$Z_q = u_{trim} \tag{4.4.1.12}$$

$$Z_{\delta_e} = 0 \tag{4.4.1.13}$$

$$Z_{\delta_T} = \frac{1}{mass}\,T_{max}\,sin\,(\beta_{RH}) \tag{4.4.1.14}$$

The linearization of the pitching moments (M) around the body Y-axis (Y_B), are evaluated according to:

$$M_u = \frac{u_{trim}\,\rho\,S\,c}{I_{YY}}\left(C_{m_0} + C_{m_\alpha}\,\alpha_{trim} + C_{m_\delta}\,\delta_{elev_{trim}}\right) - \frac{\rho\,S\,c\,C_{m_\alpha}\,w_{trim}}{2\,I_{YY}} \tag{4.4.1.15}$$

$$M_w = \frac{w_{trim}\,\rho\,S\,c}{I_{YY}}\left(C_{m_0} + C_{m_\alpha}\,\alpha_{trim} + C_{m_\delta}\,\delta_{elev_{trim}}\right) + \frac{\rho\,S\,c\,C_{m_\alpha}\,u_{trim}}{2\,I_{YY}} \tag{4.4.1.16}$$

$$M_q = 0 \tag{4.4.1.17}$$

$$M_{\delta_e} = \frac{2\,V_{a_{trim}}^2 S\,c\,C_{m_\delta}}{2\,I_{YY}} \tag{4.4.1.18}$$

$$M_{\delta_T} = 0 \tag{4.4.1.19}$$

The linearized plant and control matrices, A and B, provide a compact representation of the dynamics around each flight state. These matrices store the dimensional stability derivatives, which are then used to understand how the state vector evolves and how the control inputs affect the stability system. The state vector "x" the system matrix "A", and the input matrix "B" are defined as follows. The linearized dynamics state-space model can be presented in the form of $\dot{x} = Ax + Bu$.

$$x = \begin{bmatrix} u \\ w \\ q \\ \theta \end{bmatrix} \tag{4.4.1.20}$$

$$A = \begin{bmatrix} X_u & X_w & X_q & -g\ cos\ (\theta_{trim}) \\ Z_u & Z_w & Z_q & -g\ sin\ (\theta_{trim}) \\ M_u & M_w & M_q & 0 \\ 0 & 0 & 1 & 0 \end{bmatrix} \tag{4.4.1.21}$$

$$B = \begin{bmatrix} X_{\delta_e} & X_{\delta_T} \\ Z_{\delta_e} & Z_{\delta_T} \\ M_{\delta_e} & M_{\delta_T} \\ 0 & 0 \end{bmatrix} \tag{4.4.1.22}$$

The system's eigenvalues are analyzed since they provide information about the aircraft system's stability and response to disturbances or control inputs. The eigenvalues are obtained by solving the characteristic equation:

$$det(A - \lambda\, I) = 0 \tag{4.4.1.23}$$

Where I is the identity matrix. Solving this equation, the eigenvalues $\lambda_1, \lambda_2, \dots, \lambda_n$ are obtained, where n is the order of the system. The real parts of the eigenvalues $Re(\lambda)$ determine the stability of the system in the way that positive values are associated with stable systems, negative values with unstable systems, and equal to zero for neutrally stable systems. If the imaginary part of the eigenvalue $Im(\lambda)$ is not equal to zero, the system exhibits oscillatory behavior, and vice versa. Other stability parameters, such as the damping ratio (ξ) and the natural frequencies (ω_n) of the system are calculated.

$$\xi = -\frac{-Real(\lambda)}{|\lambda|} \tag{4.4.1.24}$$

$$\omega_n = \sqrt{Real(\lambda)^2 + Imagin(\lambda)^2} \tag{4.4.1.25}$$

Damping ratios between 0 and 1 lead to underdamped responses with oscillations, equal to 1 for critically damped responses and superior to 1 for overdamped responses without oscillations. The natural frequencies represent the rate at which the system oscillates and are calculated, similar to the damping ratios, for the short period and phugoid modes.

4.4.2. Handling Qualities Analysis

This section aims to analyze the longitudinal dynamics and control parameters of the specified ASD. The model is developed as a linearized model and analyzed around the calculated trim steady-state condition for straight and level flight. The longitudinal stability of the aircraft is then evaluated throughout the eigenvalues for each trim condition. The values from Fig. 35. are given for the multiple velocities samples, detailed further in §4.4.3.

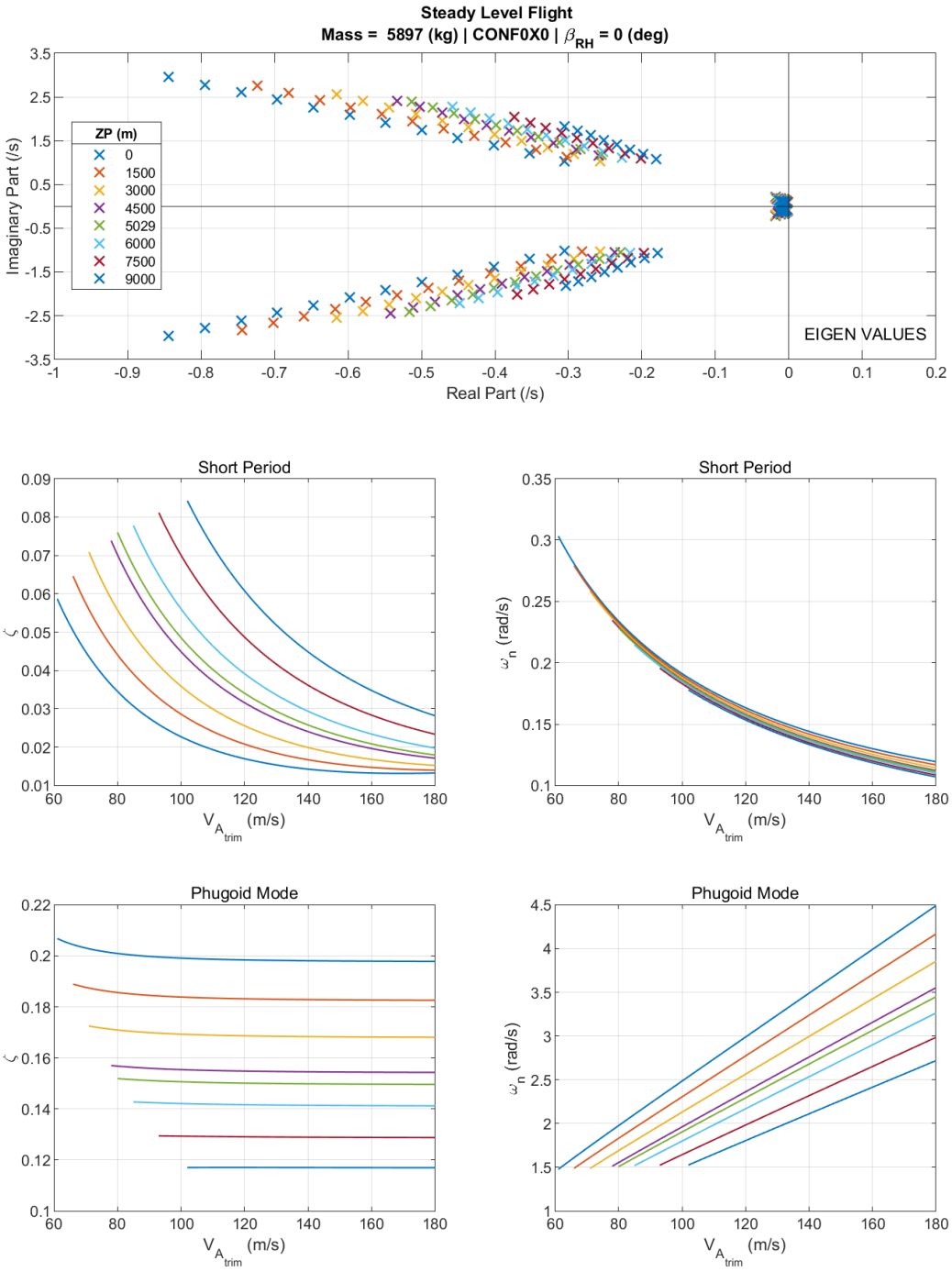

Fig. 35. Eigenvalues, natural frequencies (ξ), and damping ratios (ω) for steady-level flight at multiple ZPs

The short-period mode dominates the aircraft dynamics due to the significant imaginary parts. This behavior indicates that the aircraft exhibits a quick, short-period oscillation due to pitch changes from external disturbances or elevator control. The phugoid mode represents a slower, long-period oscillation associated with thrust control.

The damping ratios suggest that the overall oscillations tend to be weakly damped, especially at higher trim velocities. In the case of the phugoid mode, the damping ratio stabilizes at low velocities, whereas in the short period, it follows an exponential curve. The natural frequencies present similarly an exponential shape, which decreases with speed for a short period. However, in the phugoid mode, this one follows a linear trend, which increases with speed. In other words, high

velocities would lead to a more responsive but less stable aircraft, which is consistent with the nature of the aircraft model.

4.4.3. Helicopter Mode Performance Analysis

The initial validation of the proprotor performance is evaluated on the hovering condition. This flight condition is selected as the first validation loop, which integrates parameters of the ASD since the aircraft axis system does not experience any aerodynamic load from its movement. This condition simplified the model by not considering the aerodynamic forces and moments exerted by the wing, fuselage, and control surfaces. Only the proprotor wake interference and interaction with the wing are considered.

The hover characterization is evaluated by comparing the model with the Fig. 36 data at $UT/W = 1.0$ (net thrust per weight) for the weights 15000 (6804), 13000 (5897), and 10760 lb (4881 kg). The power mode used is the take-off rating, which is accordingly selected in the model. The $UT/W = 1.1$ points are not considered to be evaluated since the upper curve already represents the test itself. All the presented data is for OGE scenarios. In-ground-effect (IGE) scenarios and their performance values are not presented.

The model flight condition inputs are the correspondent reference weights, pressure altitude, and zero velocity. As described in previous sections of this document, the download is not directly imposed but is a product of the angular position of the rotor hub. The rotor hub angular position of 90° (helicopter mode) and the flap deflection, CONF75X47, are considered for the hovering case.

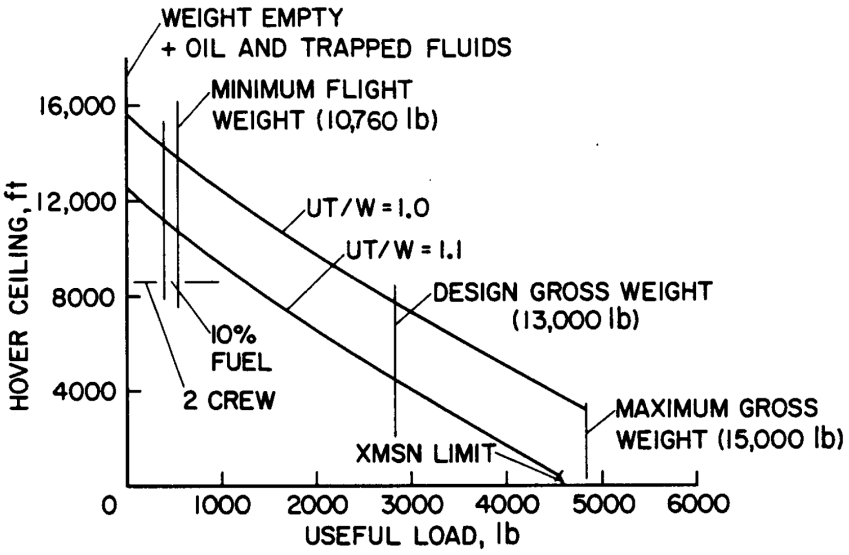

Fig. 36. Hover envelope at DISA = 0 (ºC) from OEM data [42]

A sweep in RPMs from 380 to 620 has been considered, corresponding to the lower reference RPM -10 % and the maximum reference RPM +10%. Steps of 10 have been considered in the nominal sweep. The collective/feathering angle is considered from 5 to 58° in steps of 0.2º. This sweep covers the whole operational range from hover to maximum speeds. The plots presented constitute some of the most iconic performance parameters, such as the FM, the $Power\ Required/Available$ or power ratio, and the T/W multiplied by two to account for both proprotors.

Ther results compilation of this section are post-processed as presented in Fig. 37. The right-side cut on the plot at high collective and RPM values represents the power limitation curve, where the power required becomes larger than the power available at the given flight conditions and power mode. Two reference lines, DSRH and DSRA, are plotted in the right-hand-side subplots, representing the dual-speed RPMs for helicopter and airplane modes from the original RGB. The maximum values of the T/W are automatically extracted for the reference RPMs, which are then compared against the OEM-reported value.

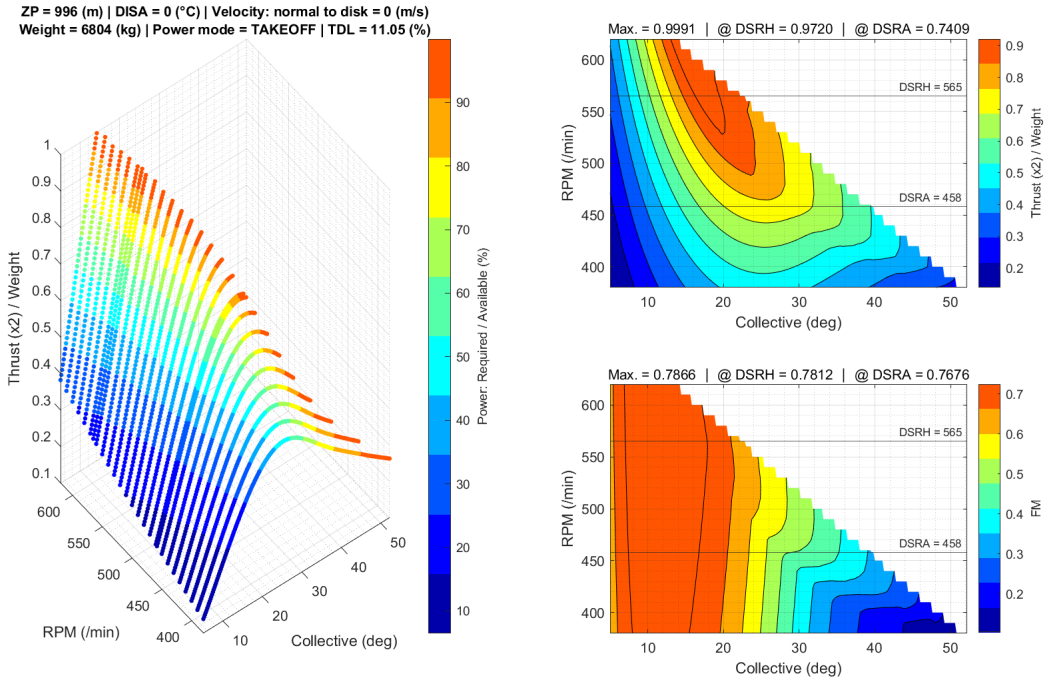

Fig. 37. Proprotor performance envelope at ZP = 996 m (3267 ft) and Maximum Gross Weight

It is observed that the highest T/W are achieved at relatively high RPMs, slightly above DSRH, for the hover flight condition while keeping the collective at a low-moderate level. The maximum peaks of aerodynamic efficiency show a significant dependency on the collective angle, while it is practically independent of the RPM value. The results show that primarily trimming the aircraft by RPM values in the low-speed section, instead of by collective, would increase the aerodynamic efficiency of the proprotor, especially when a CVT is used. Considering that hovering conditions are performed at the highest T/W and power ratios and generally last for relatively short periods, it is considered that the most representative gains of this trim would be in terms of TMM deterioration, which is mainly affected by high power ratios.

The hover performance has been validated with an error margin of 2.84, 1.62, and 2.18% for the maximum gross, design gross, and minimum flight weights, respectively. These deltas do not entirely represent the model accuracy since flight tests were performed with updated proprotor geometrical characteristics. The current model is on the conservative side for hovering analysis since lower C_T/C_P have been achieved.

4.4.4. Airplane Mode Performance Analysis

The aircraft performance model is validated at the OEM-reported flight state conditions for maximum speeds, as presented in Fig. 38. The reference cruise altitude and speeds are associated

with pressure altitude values equal to 5029 (m) and a velocity of 154 m/s. The power mode for the validation cycles is the "CONTINGENCY" for all engine operatives (AEO) or twin engines. Three particular points are extracted from the OEM flight envelope: the corner point between the dive torque limit and the dashed contingency power curve, the intersection between the contingency power and the maximum operating speed (VMO), and an intermediate point at 12000 ft or 3658 m of pressure altitude.

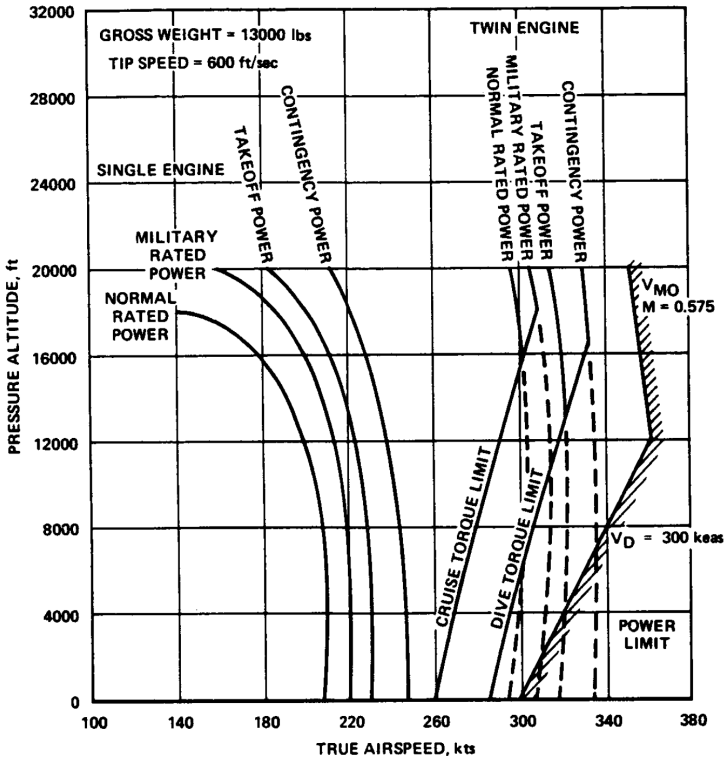

Fig. 38. Airplane mode flight envelope at DISA = 0 (ºC) from OEM data [42]

The maximum thrust available (T_A), considering both proprotors, is presented in Fig. 40 for the previously exposed conditions. The ZP range is displayed for general information purposes from 0 to 9000 in steps of 1500 m, including the altitude of 5029 m. Two plots are presented, one at an RPM of 458, the OEM RPM for airplane mode or DSRA, and another in which all the pre-computed RPM ranges are presented. The maximum thrust available is limited by the power available from the "CONTINGENCY" mode and a power limit of 705432 W, which is imposed by the structural limitations of the proprotor transmission system.

The allowance for switching between multiple RPMs gives substantial increases in the maximum T_A, especially in the low-speed region, as presented by comparing Fig. 39 and Fig. 40. However, in the high-speed region, the maximum achievable T_A are generally achieved at RPM settings close to the DSRA. This behavior is further explained in §4.5, where the optimization procedures of the proprotor control system are detailed.

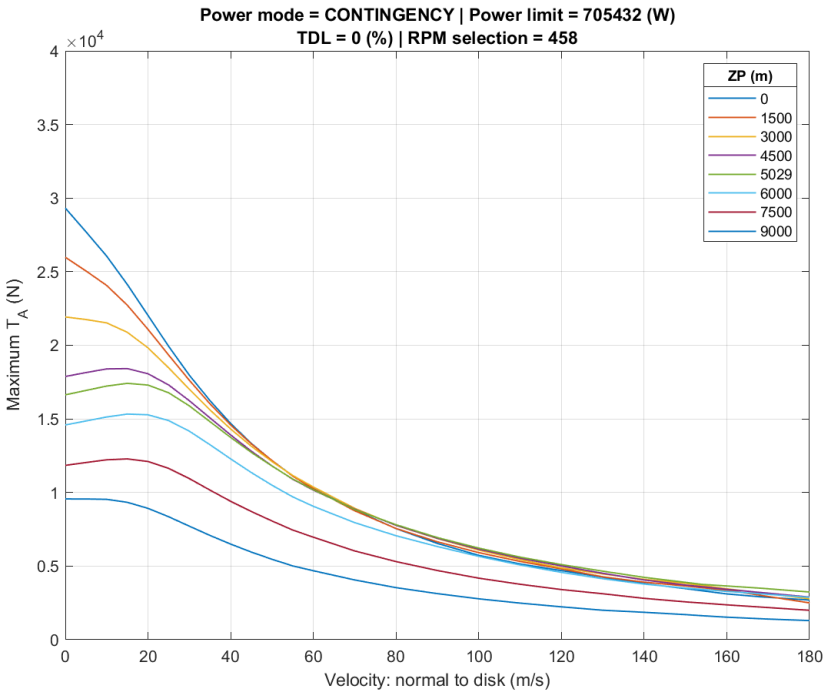

Fig. 39. Maximum thrust available envelope for CONTINGENCY power mode and RPM = 458

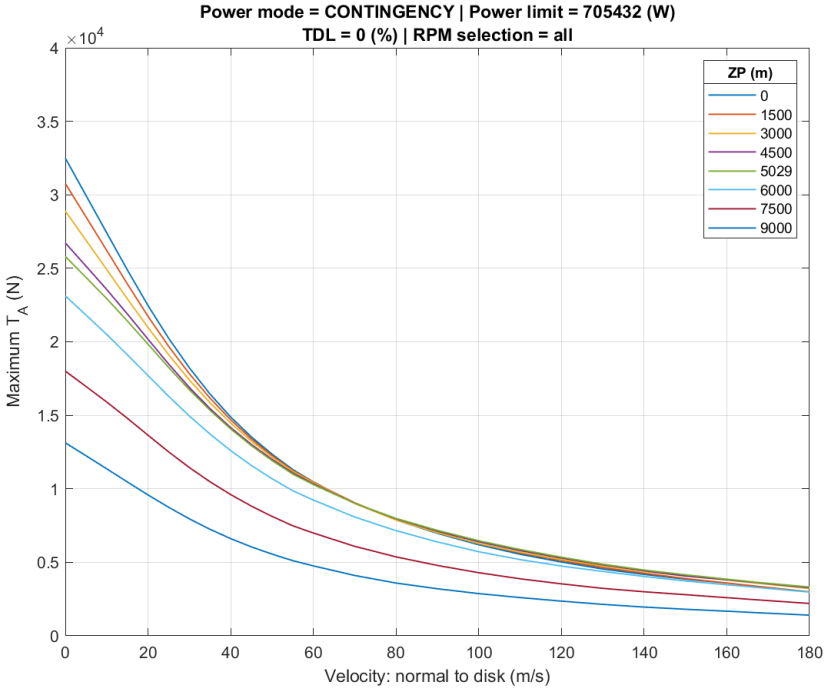

Fig. 40. Maximum thrust available envelope for CONTINGENCY power mode and all RPMs

The main trimming parameters for steady-level flight at the whole pressure altitude range previously referred to are given in Fig. 41. The parameters presented are the angle of attack α, the thrust required T_R, and the elevator deflection δ_{ELEV}, to achieve a zero pitch rate q and flight path angle γ, at each velocity V_A. The thrust required is presented as the net thrust value, i.e., after deducting the losses from the proprotor wake interference.

The thrust required for steady-level flight trim shows absolute minimums at the maximum speeds. At first glance, this behavior might seem counterproductive; however, the reason is that the lift generated by the aerodynamic surfaces softens the power requirements of the power plant, which consequently loses capabilities at high speeds, as previously presented at the maximum thrust available plots. At the low-speed region, peaks in the thrust required are found, especially at high altitudes, as the lift generated by the wing drops considerably, hence demanding higher thrust to maintain the level of flight condition. The necessary angle of attack decreases exponentially as the speed increases, from the near-stall values up to negative values at the maximum speed region. The progression behavior of the elevator trim is opposite to the angle of attack, with negative values being up-wards deflection of the elevator. The elevator deflection compensates for the pitching moment generated by the wing in order to have a zero pitch rate. The curves for each ZP are presented until the velocities at which the stall speed VS1G are found.

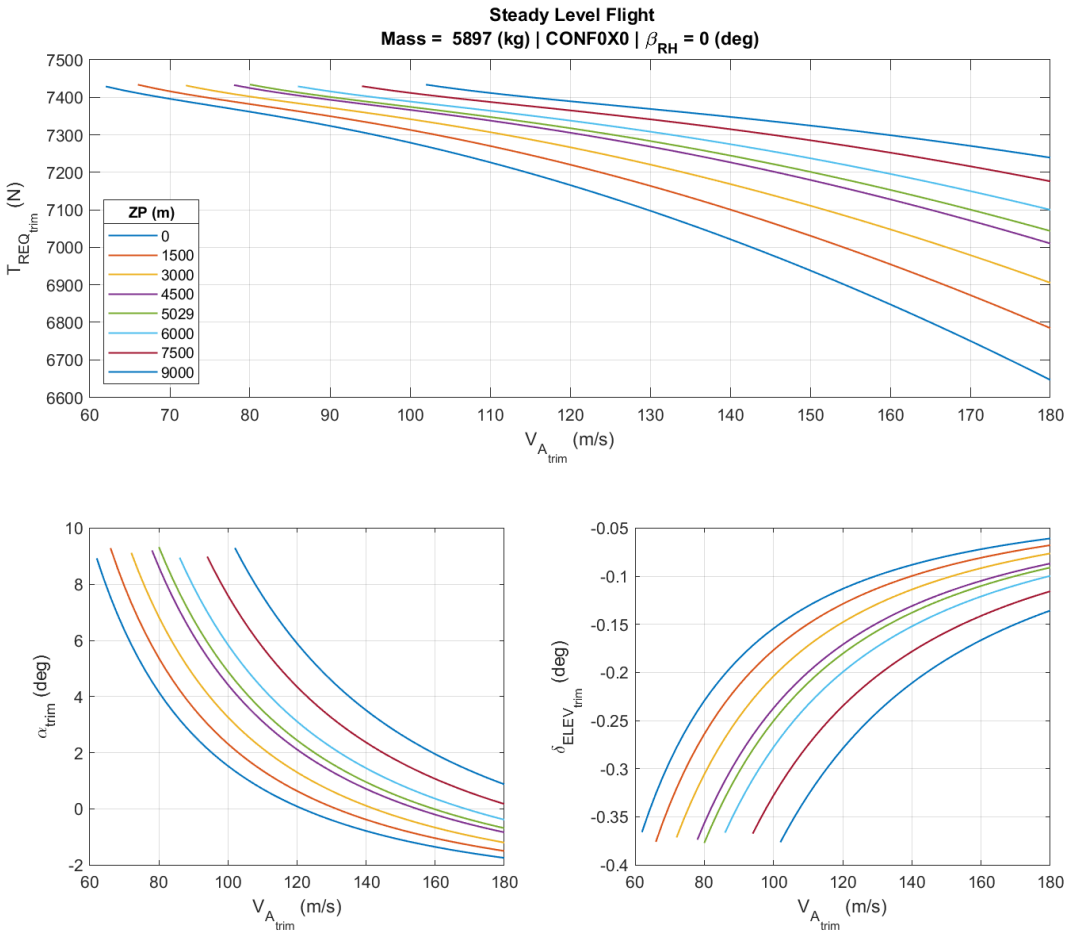

Fig. 41. Steady Level Flight trim parameters in airplane mode and CONF0X0 at multiple ZPs

The maximum rate of climb (ROC) at different speeds and altitudes is presented in Fig. 43. Analyzing the ROC under the different flight conditions, the aircraft ascent capabilities, and the maximum speed for steady-level flight, which happens to be at zero ROC, can be extracted. The maximum ROC plot gives insights into traffic and obstacle avoidance capabilities by maximizing the flight path angle. The ROC is computed according to the following formula.

$$ROC_{max} = V_{A_{trim}} \sin(\gamma) = V_{A_{trim}} \frac{T_{available_{max}} - T_{required_{trim}}}{Weight} \quad (4.4.4.1)$$

Common ROC calculation methodologies generally simplify the numerator component to the difference between thrust available and drag. This common assumption considers that the thrust vector is perfectly aligned with the drag vector, which is generally untrue. Following this assumption, the computation loop tends to lose reliability as the angle of attack increases, or more precisely, the orientation difference between the thrust and the drag vectors. This second factor accentuates if the thrust vector reorientation capabilities are considered. Other methodologies simplify the calculation process using empirical factors generally given by generic recommended values. The maximum ROCs achievable with allowance for switching between RPMs for maximum aerodynamic efficiency and for RPM = 458 are given in Fig. 42 and Fig. 43, respectively.

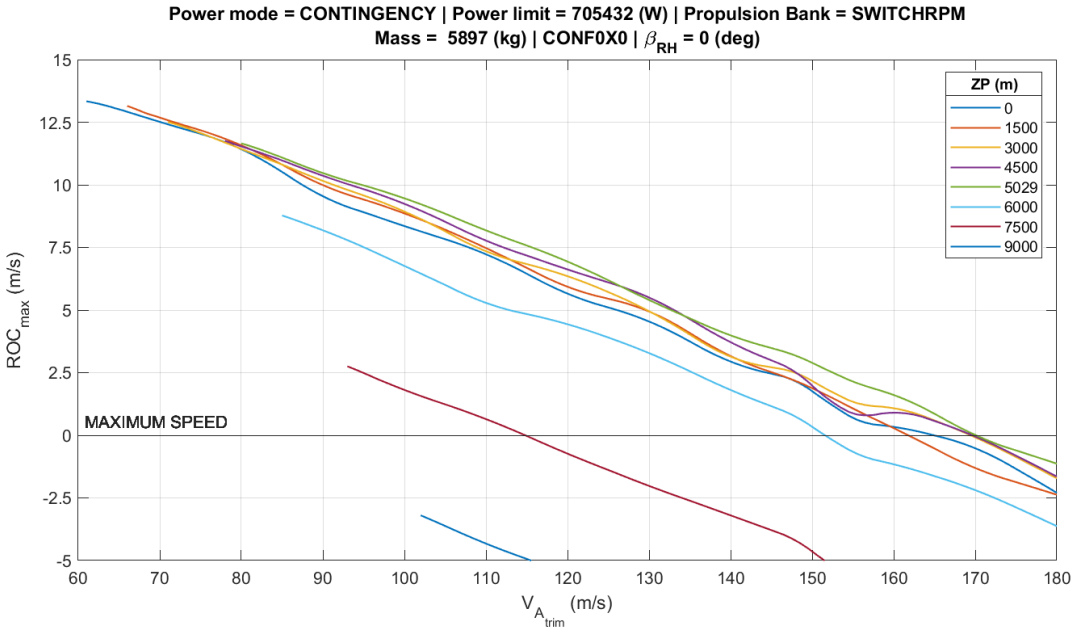

Fig. 42. Maximum ROC in airplane mode and CONF0X0 for CONTINGENCY and all RPMs

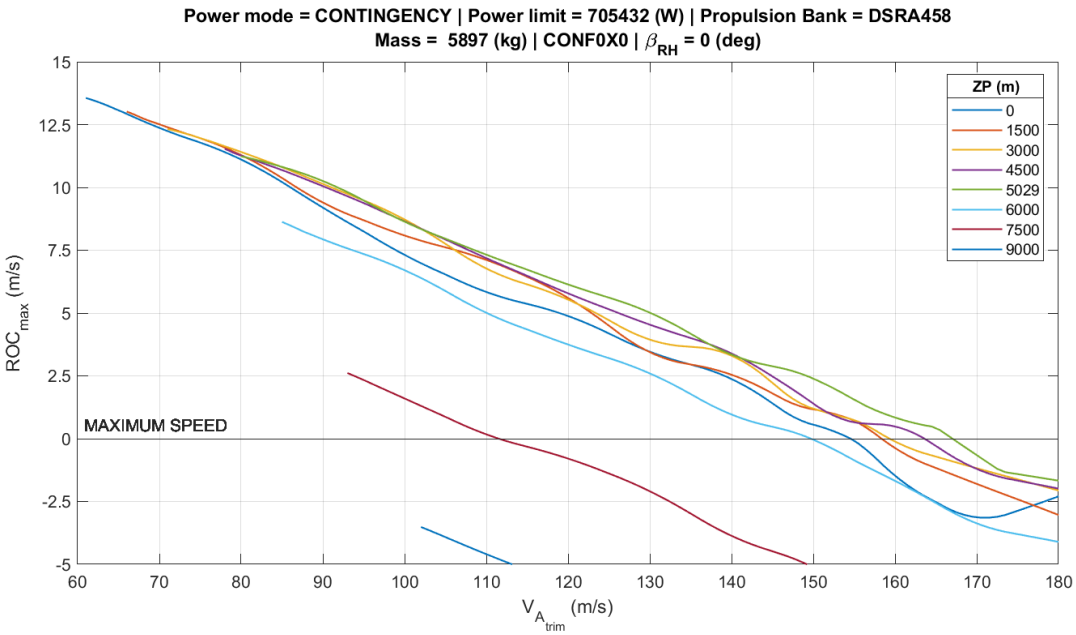

Fig. 43. Maximum ROC in airplane mode and CONF0X0 for CONTINGENCY and RPM = 458

The maximum ROC values evolve following a linear trend, giving maximums at the low-speed regime. The behavior presented, which differs from conventional parabolic behaviors that present maximums at speeds not so close to VS1G, is due to the high thrust capabilities of the studied aircraft, especially at low-speed regimes. The maximum values are consistent with aircraft of similar characteristics, whereas the zero ROC, or maximum speed, is validated in §4.5.2. Substantial ROC capabilities decrements are found at higher pressure altitudes than 6000 m, whereas the best ROC is found at 5029 m for practically the whole velocity range. This behavior is consistent with the fact that the reported cruise altitude is generally performed at the same flight level (FL 165). The irregularities in the ROC curves are due to the lack of further refinement of the maximum thrust available, especially in the case of RPM 458. It is recommended that further refinement is performed by reducing the step values between the collective sweeps.

The specific range (SR) is calculated since it represents the distance the aircraft can fly per unit of fuel or energy consumed. This parameter retrieves the most fuel efficiency altitude and speed for the trajectory executed. The speed at which the SR is maximum is commonly referred to as the optimum cruise speed or maximum endurance speed. It is worth mentioning that this parameter depends on the trim condition and the power mode selected, as the SFC is implemented into the calculation.

$$SR = \frac{V_{A_{trim}}}{\dot{m}_{fuel}} = \frac{V_{A_{trim}}}{(SFC)\, P_{required}} \tag{4.4.4.2}$$

The SR plots are presented for the allowance to switch between RPMs and RPM = 458 in Fig. 44 and Fig. 45, respectively. The plot for RPM = 458 presents the steadiest behavior at high speeds due to the resolution in power required achieved by increasing the resolution of the collective angle at the given RPM. The highest pressure altitudes, between 9000 and 6000 m, overshoot the SR value at high speeds as the ROC becomes zero. The couples of velocities and altitudes that give a negative ROC should not be considered, as they are associated with the dive-flight condition.

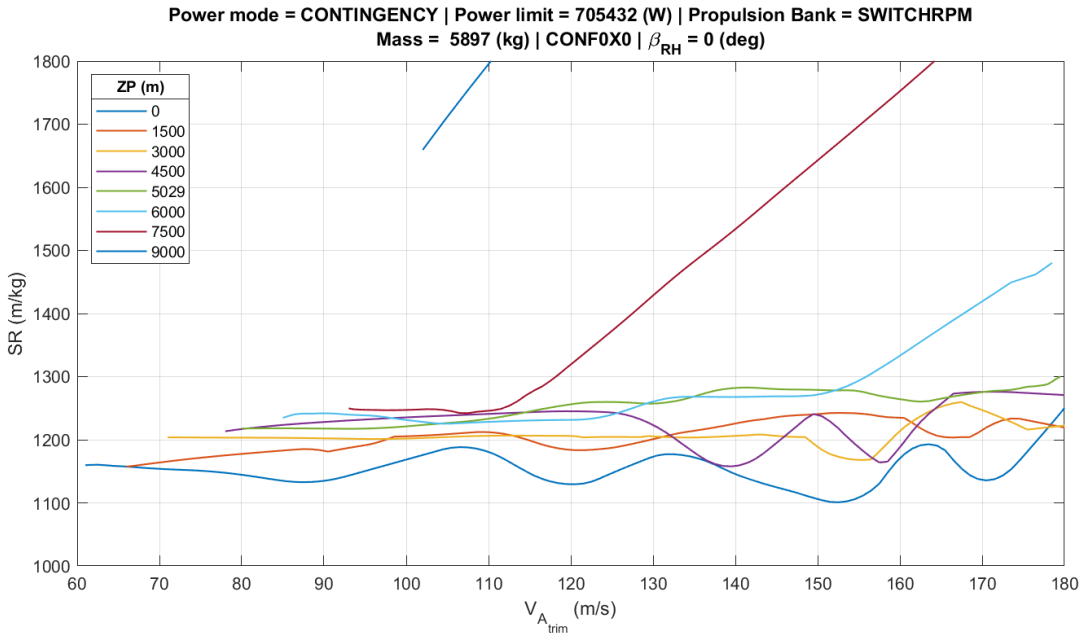

Fig. 44. SR in airplane mode and CONF0X0 for CONTINGENCY and all RPMs

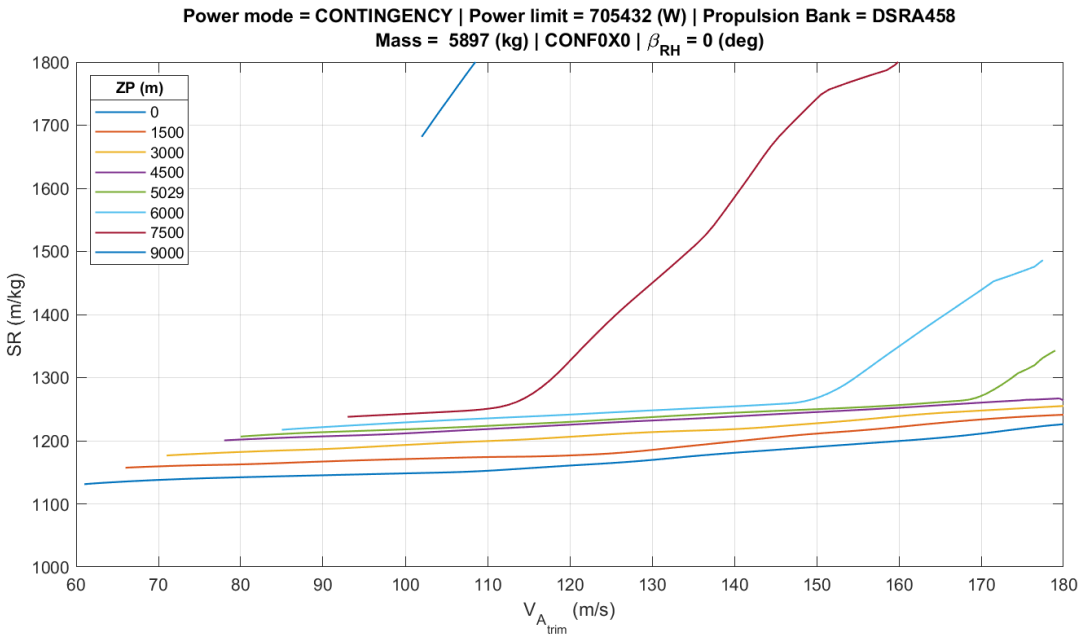

Fig. 45. SR in airplane mode and CONF0X0 for CONTINGENCY and RPM = 458

The performance parameters relevant to energy consumption management culminate with the endurance calculation. The endurance represents the maximum duration the aircraft can remain airborne for a given fuel amount. The endurance parameters are mainly used in flight missions such as surveillance, reconnaissance, and search and rescue.

$$Endurance = \frac{m_{fuel}}{\dot{m}_{fuel}} = \frac{m_{fuel}}{(SFC)\ P_{required}} \tag{4.4.4.3}$$

The SR plots are presented for the allowance to switch between RPMs and RPM = 458 in Fig. 46 and Fig. 47, respectively. Similarly, as for the SR plots, the case for RPM = 458 presents a steadier behavior due to the increased resolution in the collective angle and, hence, the power required for each flight condition. As for the SR, the gains in endurance are marginal when observing the whole envelope, between both RPM settings when observing the whole range. However, these become more apparent when the performance parameters are further refined and analyzed for specific envelope points. Further detail of these results is given in §4.5.2.

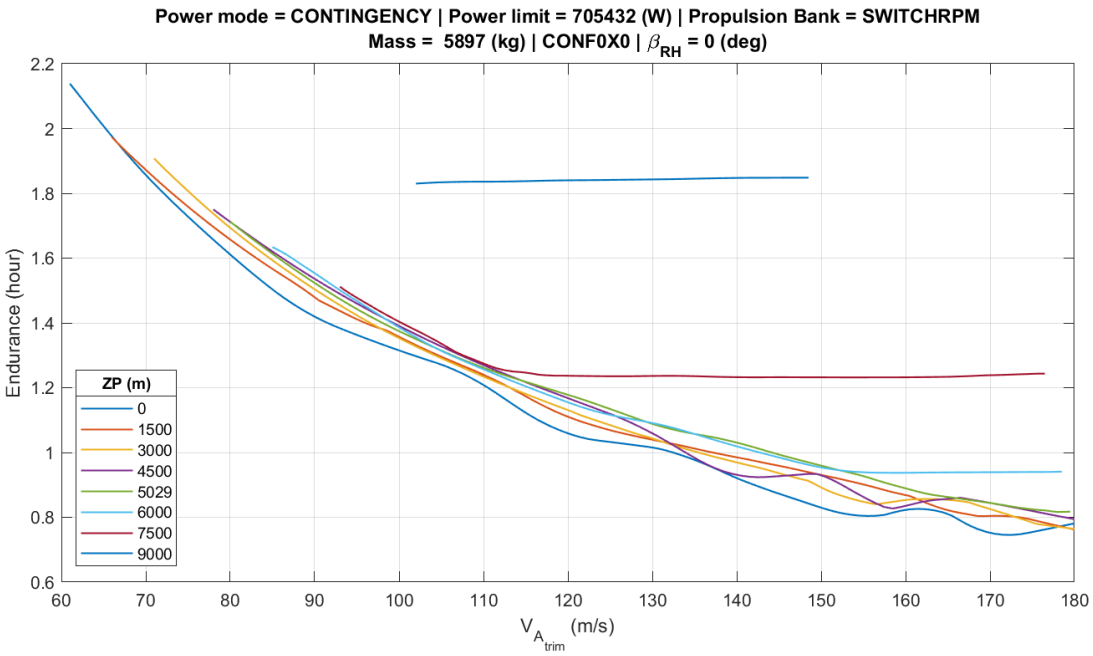

Fig. 46. Endurance in airplane mode and CONF0X0 for CONTINGENCY and all RPMs

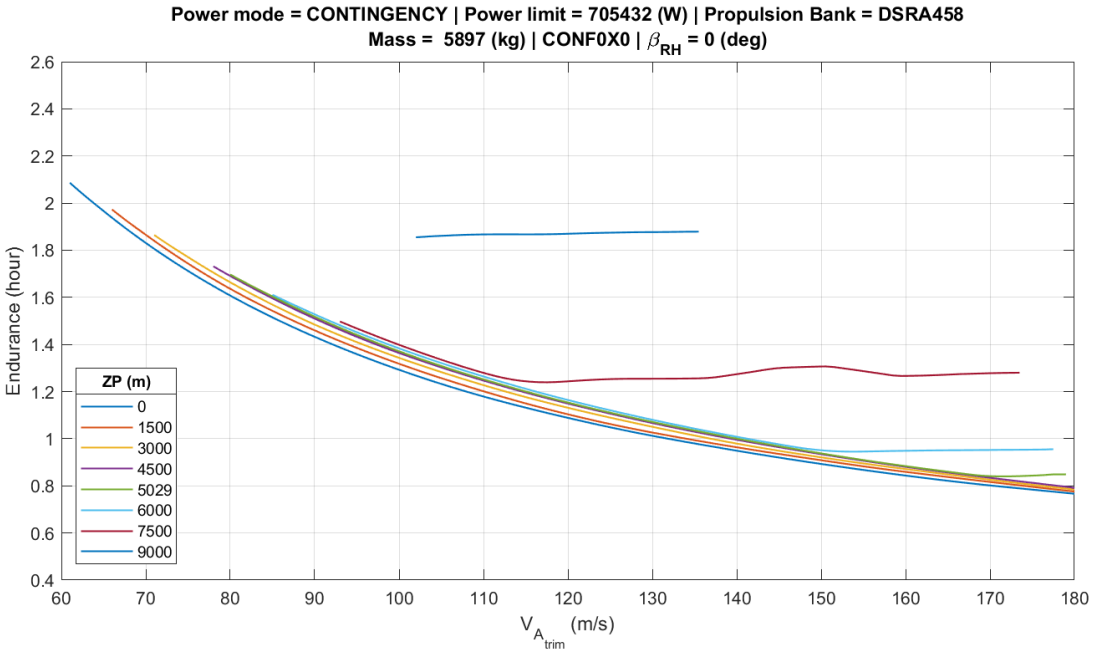

Fig. 47. Endurance in airplane mode and CONF0X0 for CONTINGENCY and RPM = 458

This project calculates the endurance using the maximum usable fuel on board, which equals 675 kg. Additionally, refined endurance plots would reduce from this fuel quantity the amount needed to climb or reach a specific altitude and speed, as well as a fuel reservoir. Since the actual code does not contemplate trajectory analysis, this process is simplified as explained.

4.5.Optimization of the Proprotor Control System

4.5.1. Systematization of the Computational Routine

The RPM and the collective are optimized throughout the whole operational envelope, from hover to maximum speed and from SL to maximum ceiling. These parameters are optimized for each

combination of the swept flight conditions, i.e., ZP, DISA, and velocity normal to the disk, such that the RPM and the collective are controlled by the Power Required/Available or power rating.

The algorithm identifies, for each pre-computed flight condition, the values of collective and RPM that maximize the FM, i.e., aerodynamic efficiency. The resulting optimal values are stored in a data frame and used as the training data of the Gaussian Process Regression Methodology (GPR) or "fitrgp" MATLAB tool. GPR models serve as a nonparametric approach in supervised learning, particularly adept at addressing regression and probabilistic classification challenges. This methodology has been chosen due to its potential to capture complex relationships without assuming a specific functional form and its ability to provide probabilistic predictions.

The uncertainty is primarily affected by the amount of training data and its distribution, and the prediction method ('PredictMethod') is selected, which in this case is selected as 'Exact'. The 'Exact' prediction method implies that the GPR model performs exact Gaussian process inference without approximations such as 'BCD' – Blockwise Coordinate Descent, or 'SD' – Subset of Data. The confidence interval is configured to 68% (1σ) instead of the conventional 95% (2σ) due to the desire for precise estimates, even though data scattering increases, especially at the high-speed regimes.

The velocity normal to the disk is evaluated from 0 to 60 in steps of 5 and from 60 to 180 in steps of 10 m/s. The greater input resolution at the low-velocity range is performed since the optimal RPM and collective values present a notorious non-linear behavior. The altitude or ZP sweep is evaluated from 0 to 9000 in steps of 1500 m, adding the 5029 m value corresponding to the reported OEM cruise condition. The power rating is generally cut in the plots from 40 to 100%, as values below 40% are not operational representative, and 100% is the capabilities limit of the TMM.

The optimized RPM and collective values for the low-speed regime are presented in this document for ZP = 996 m, which corresponds to the altitude reference for T/W=1.0 at the maximum gross weight, as presented in Fig. 37. The zero-velocity condition leads to optimized RPM values in the power rating range of 85-100% which are above the DSRH reference. However, for a velocity of 35 m/s, the optimized RPMs correlate well with the DSRH for the high power rating values, as given in Fig. 48.

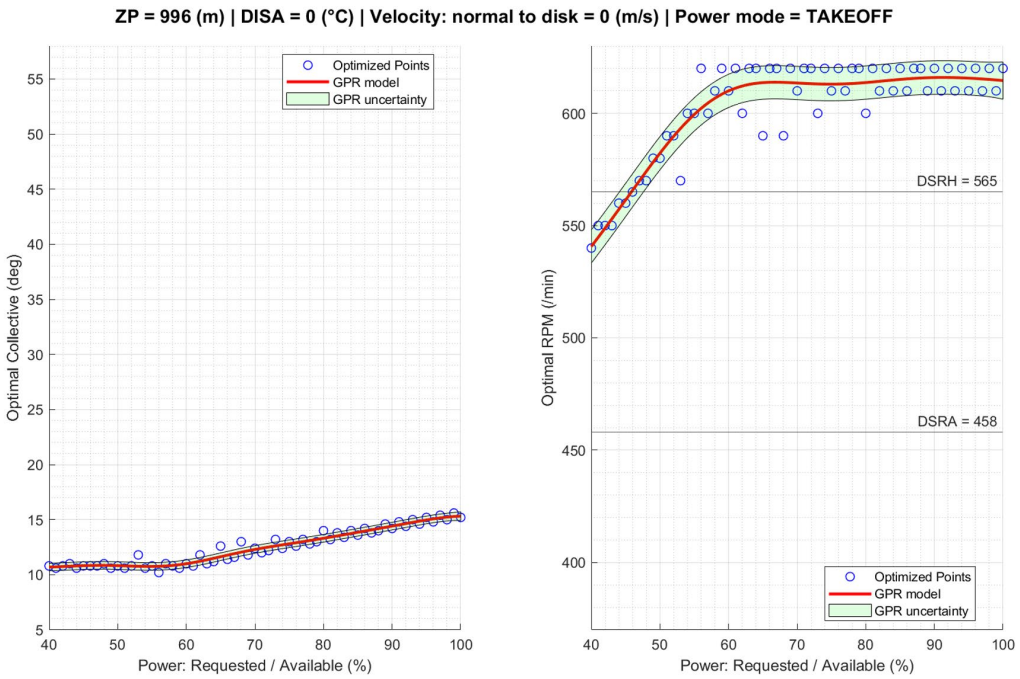

Fig. 48. Optimal collective and RPM settings at hover for ZP = 996 (m)

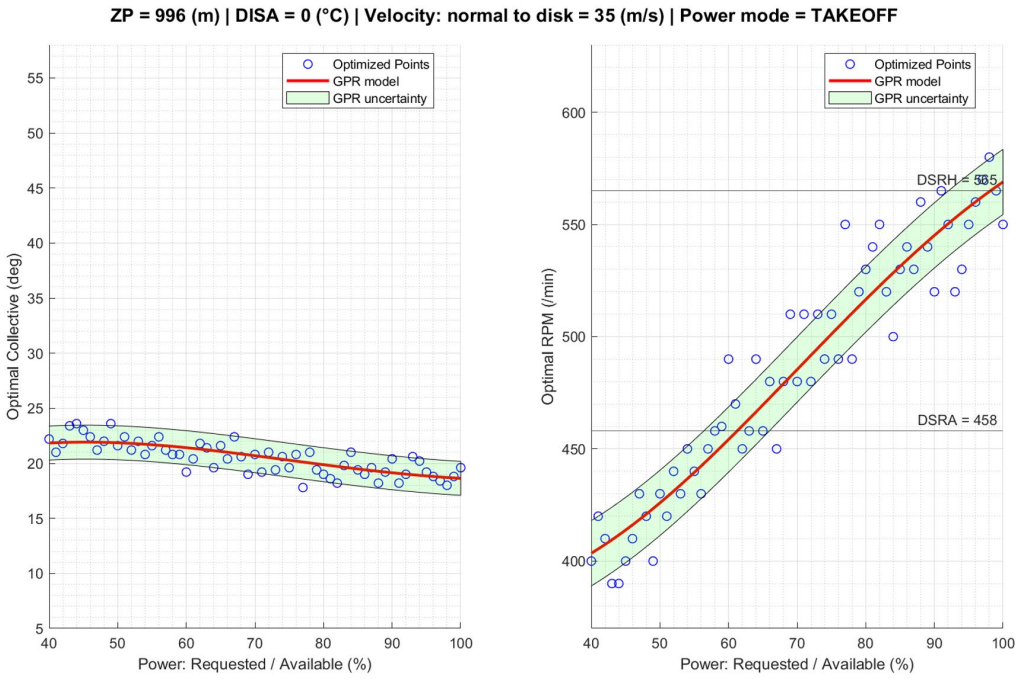

Fig. 49. Optimal collective and RPM settings at approach speed for ZP = 996 (m)

It can be assumed that the OEM RPM setting might not be optimized for pure hover conditions but instead for a low-speed regime, which might be found during the near helicopter mode transition phases. If the DSRH had been optimized for the pure hover condition at ZP = 996 m, a value of 615 should have been chosen instead of the original RPM of 565. It is to be noted, however, that higher ZP values lead to noticeably higher RPM values and slightly higher collective values.

The optimal collective and RPM values are given for the low-velocity envelope, i.e., from 0 to 40 m/s, in Fig. 50. The optimal collective angle shows a relatively constant evolution throughout the

velocity axis. In contrast, the optimal RPM follows a radical-type curve. The highest collective angles are naturally found at the highest speeds, with maximums in the 22° vicinity. The algorithm has chosen neither the minimum or the maximum computed collective and RPM values as optimum combinations.

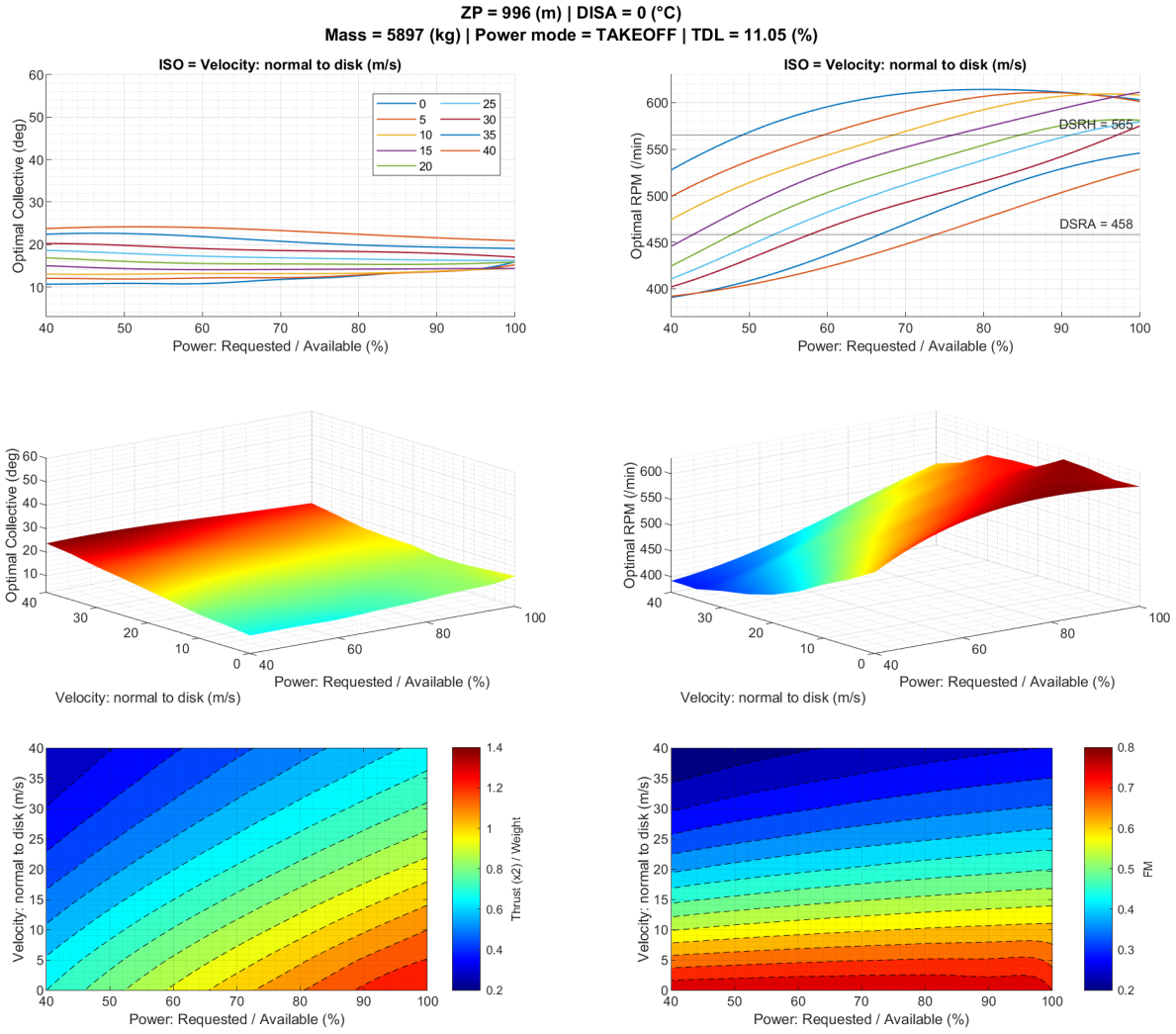

Fig. 50. Optimal collective and RPM settings characterization at low-speed-region for ZP = 996 (m)

The high-speed regimes present a more constant behavior on the optimized RPM and collective values than the low-speed regimes. The OEM-reported cruise altitude and speed case are presented in Fig. 51. In this flight condition, the power command has a practically null impact on the optimized parameters. The optimal collective optimized points are slightly more scattered than in the low-speed regimes. In the case of the RPM-optimized points, a significant scattering, or GPR uncertainty, is found. This behavior is found in high-speed regimes because similar high FM values are found for a more extended RPM range and power command than in low-speed regimes. In other words, the optimal RPM setting is not confined to a narrow range. Changes in optimized RPM settings would lead to different collective angles to match the power and thrust values; however, since collective changes have more impact on the performance parameters, these are not so scattered. Resolution in the precomputed collective values, in the order of 0.1º, and RPM steps of 5, is recommended to be done due to the high sensibility of this parameter on the performance values at high speeds.

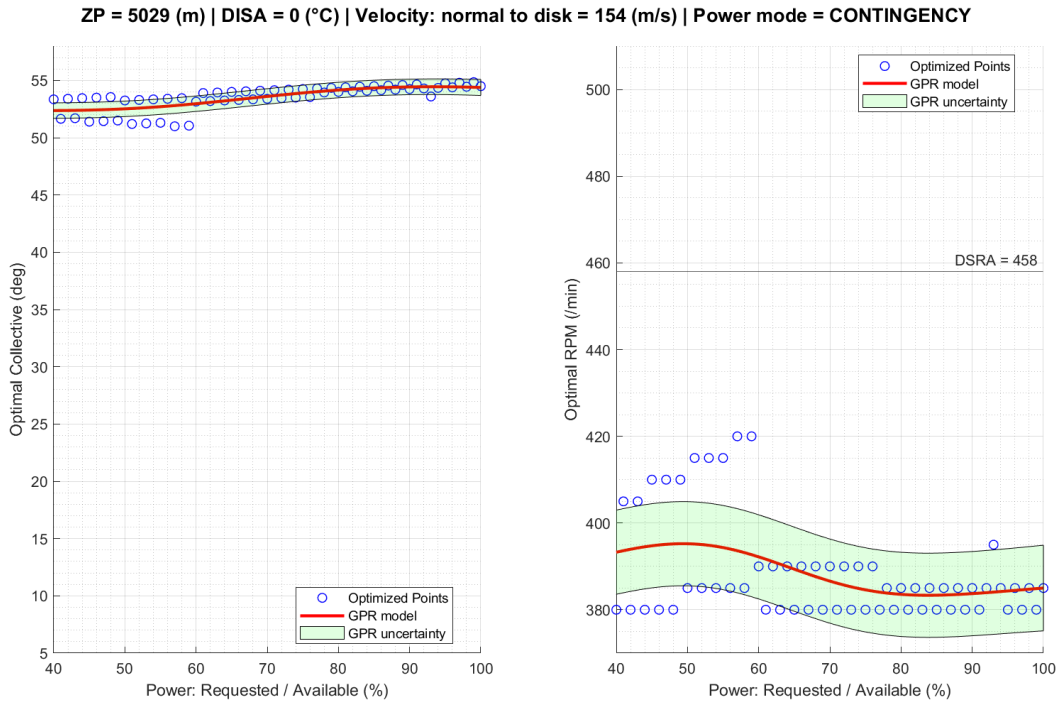

Fig. 51. Optimal collective and RPM settings at OEM cruise speed and altitude ZP = 5029 (m)

A more complex progression of the optimal values is found in the case of the RPM setting. Two main regions can be distinguished: a high RPM setting at velocities approximately inferior to 50m/s and a mild linear progression in the region from 50 m/s up to the maximum value of 180 m/s, as presented in Fig. 52. Similarly, as in the optimal collective setting, the power axis has almost no effect at velocities superior to 50 m/s. However, at lower velocities, the optimal RPM curve exponentially progresses from the lower power values to saturations at the maximum configured RPM setting of 630 rev/min.

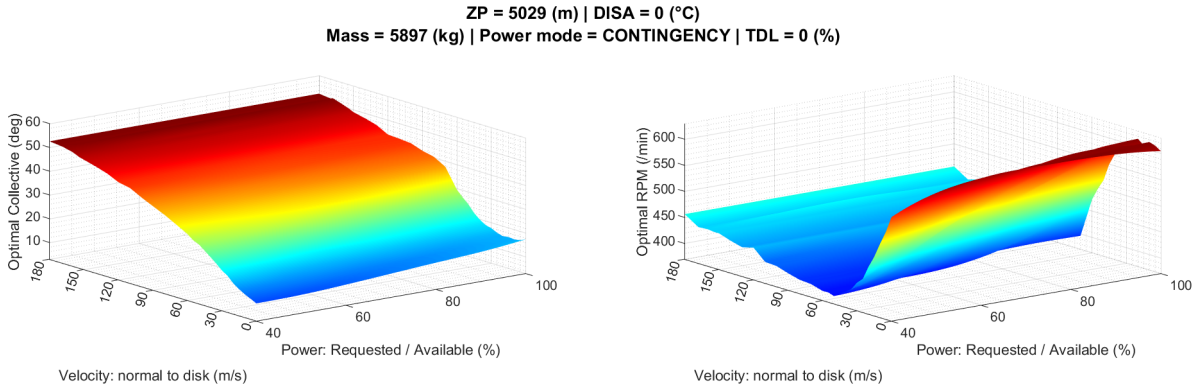

Fig. 52. Optimal collective and RPM settings characterization at all speeds for ZP = 5029 (m)

For the optimization loop at ZP = 5029 m, it can be assumed that even higher RPM values would be considered during the optimization process at the low speed and high power regimes if introduced in the pre-optimization process, i.e., during the computation-sweep. However, the maximum RPM value, which would be possible to implement into the developed aircraft, would be constrained by the transmission system's operative range. Recapitulating on the high-speed regime, higher

resolution in the collective or feathering angles is recommended to avoid the algorithm choosing a constant set of RPM and collective for the power axis.

4.5.2. Summary of Optimized Integrated Results for OEM Reported Flight Conditions

Recapitulating the results from sections §4.4.3 and §4.4.4, Table 3 shows the thrust, power requested, reference RPM, and necessary collective values for each flight case analyzed. These values are then compared with the proprotor trimming setting to minimize the power required at the same thrust of the reference case and the trimming setting to maximize the thrust at the same power required of the reference case. The setting for the minimum power required is extracted from the optimization process described in this section. In contrast, the maximum thrust is obtained by extracting the maximum singular thrust value for the given power required at the specified flight case.

It is to be considered that the T/W of the hovering flight cases does not match the exact value of the OEM (1.000). This mismatch is due to the resolution in the values of RPM and collective at which the sweep computations were launched and the fact that no interpolation of the results has been performed for this particular analysis. The PCS of the OEM references does not match the 100% value due to the lack of further resolution in the precomputed input parameters of the proprotor performance model. The performance values are the total for both proprotors, except for the induced velocity for each wake.

The optimization for minimum power required has led to a decrease in the PCS by increasing the RPM from the original value of 565. In this way, fuel consumption is reduced for all pressure altitudes. Considering that hovering scenarios are usually not maintained for long periods, the decrease in the PCS would be the main advantage of this optimization procedure. The decrease in PCS would increase the lifespan and time between maintenance inspections of the engines and the transmission systems. The optimization for maximum thrust has led to increases in the T/W ratio by increasing the RPM at even higher values than the optimization of minimum power required. These increases would lead to increases in the payload capabilities without additional power demands on the TMM with respect to the original configuration. The numerical values of these differences are given in Table 3.

Generally, higher RPMs in both optimization procedures have been achieved for all the hovering flight cases compared to the OEM reference value. Even though the collective has decreased, the induced velocity values for all the flight cases are slightly higher than in the OEM reference. Higher induced velocities might not be desired in cases where troops are located in the surroundings of the proprotor wake or if the aircraft is operated in dusty environments. Nevertheless, the increase in the induced velocity makes these possible adverse effects negligible. The increase in the optimized RPM values might tend to increase the noise emission levels of the proprotor. However, further detailed analysis would be needed to quantify these effects. From the perspective of structural analysis, higher RPMs increase the centrifugal forces on the proprotor system, which would need to be considered in the dimensioning and fatigue analysis of the structure and, more precisely, the attachment between the blades and the transmission hub.

Table 3. Optimization results of minimum power required and maximum thrust for hovering flight cases

	SCENARIO	MAXIMUM HOVER	MAXIMUM HOVER	MAXIMUM HOVER
FLIGHT CONDITION	ZP (M)	996	2354	4206
	DISA (ºC)	0	0	0
	V_A (M/S)	0	0	0
	MASS (KG)	6804	5897	4881
	POWER MODE	TAKEOFF	TAKEOFF	TAKEOFF
	CONF	75X47	75X47	75X47
	β_{RH} (DEG)	90	90	90
OEM REFERENCES	T/W	0.9720	0.9839	0.9784
	POWER REQ. * (W)	1892448	1712608	1473956
	PCS (%)	99.82	98.93	99.52
	M_FUEL (KG/MIN)	11.20	10.14	8.72
	PROPROTOR IND. VEL. (M/S)	17.52	17.54	17.49
	RPM (/MIN)	565	565	565
	COLLECTIVE (DEG) *	17.4	18	18.8
OPTIMIZED MINIMUM POWER REQ.	PCS (%)	94.15	92.77	91.56
	|DELTA| PCS (%)	5.67	6.16	7.96
	DELTA M_FUEL (%)	5.85	6.43	7.21
	PROPROTOR IND. VEL. (M/S)	17.96	18.00	17.98
	RPM (/MIN)	620	620	620
	COLLECTIVE (DEG)	13.8	14.2	14.6
OPTIMIZED MAXIMUM THRUST	T/W	0.9991	1.0233	1.0271
	|DELTA| T/W (%)	0.0271	0.0394	0.0487
	|DELTA| MASS (KG)	190	236	243
	PROPROTOR IND. VEL. (M/S)	18.08	18.26	18.29
	RPM (/MIN)	610	620	620
	COLLECTIVE (DEG)	14.8	14.8	15.4

	Error margin from the model deviations
	Error margin from the resolution in the computation inputs
	Improvement in the performance parameters after optimization

* Equivalent values to match OEM reference performance parameters

NOTE: All the numerical values are given per proprotor

The summary of the optimization results derived from the flight dynamic model for minimum power required and maximum speed at steady level flight have been recomputed with respect to the initial computational sweep to have a better resolution between the inputs of the proprotor performance algorithm. The main results from the validation loop are presented in Table 4. This methodology has been performed since, at high velocities, the proprotor performance is considerably sensible to changes in the trimming parameters. Iteration between the proprotor performance results and the aircraft trimming algorithm is necessary to find the maximum thrust available at each updated flight condition.

Contrary to the optimization results for the hovering phase, in this case, the RPM settings for the optimized minimum power required and maximum speeds are lower than for the OEM reference. In this case, the optimized RPM for minimum power required and maximum speed are the same.

During the optimization for minimum power required, the reductions in fuel consumption are noticeable, especially at medium and high altitudes. Lower PCS is needed to fly at the same speed as in the OEM reference, increasing the lifespan of the powerplant and the transmission system. For the maximum speed optimization, the improvements are similar for all the altitudes considered.

Considering that lower RPM settings than for the OEM reference are presented, additional system analysis would be recommended. A lower RPM would give less inertia to the proprotor, which would not be desired in case of engine failure, as this one would not be able to autorotate or windmill for such long periods. An analysis of vibrations on the airframe structure needs to be conducted to confirm that no resonance peaks are excited. It is to be expected that the new RPM setting might decrease the noise emissions in the cabin, as well as in the surrounding areas.

Table 4. Optimization results of minimum power required and maximum speed at steady-level flight

	SCENARIO	MAXIMUM SPEED	MAXIMUM SPEED	MAXIMUM SPEED
FLIGHT CONDITION	ZP (M)	5029	3658	2757
	DISA (ºC)	0	0	0
	V_A (M/S)	163.0	164.0	165.0
	MASS (KG)	5897	5897	5897
	POWER MODE	CONTINGENCY	CONTINGENCY	CONTINGENCY
	CONF	0X0	0X0	0X0
	β_{RH} (DEG)	0	0	0
OEM REFERENCES	T (N)	7542	7386	7178
	POWER REQ. * (W)	1422780	1430440	1422980
	PCS (%)	100.85	101.39	100.86
	M_FUEL (KG/MIN)	8.14	8.18	8.14
	α_{trim} (DEG)	-0.1367	-0.6096	-0.8830
	δT_{trim} (%)	0.94640	0.95585	0.97507
	RPM (/MIN)	458	458	458
	COLLECTIVE (DEG) *	50.7	50.6	50.6
OPTIMIZED MINIMUM POWER REQ.	PCS (%)	95.48	93.63	95.40
	|DELTA| PCS (%)	5.37	7.76	5.46
	M_FUEL (KG/MIN)	7.70	7.55	7.70
	DELTA M_FUEL (%)	5.56	5.27	5.56
	RPM (/MIN)	385	385	385
	COLLECTIVE (DEG)	57.6	57.1	56.8
OPTIMIZED MAXIMUM SPEED	T (N)	7411	7521	7326
	V_A (M/S)	170.0	169.5	168.5
	|DELTA| V_A (M/S)	7.0	5.5	3.5
	α_{trim} (DEG)	-0.3842	-0.7752	-0.9789
	RPM (/MIN)	385	385	385
	COLLECTIVE (DEG)	58.5	57.9	57.5
	Error margin from the model deviations			
	Error margin from the resolution in the computation inputs			
	Improvement in the performance parameters after optimization			
* Equivalent values to match OEM reference performance parameters				
NOTE: All the numerical values are given per proprotor				

4.5.3. Operational Implementation of the Optimized Control System

The proposed optimized control system differs from the conventional architecture of proprotorcrafts. The proposed system reduced pilot workload in the case that throttle input used to be performed in a conventional system and prevented overloading the TMM by current state feedback to the FMS. A diagram representing this system next to a generic conventional one is given in Fig. 53. Current fly-by-wire aircraft usually possess this capability; however, it is not the case on most current rotorcrafts, especially helicopters. The proposed system increases the aerodynamic efficiency of the rotor system in the case that a DS or a CVT gearbox is used. The system keeps the rotor's RPM at the optimum operating point by coupling the possible RGB ratios with the allowed TMM RPM range, defined by the intrinsic characteristics of the engine.

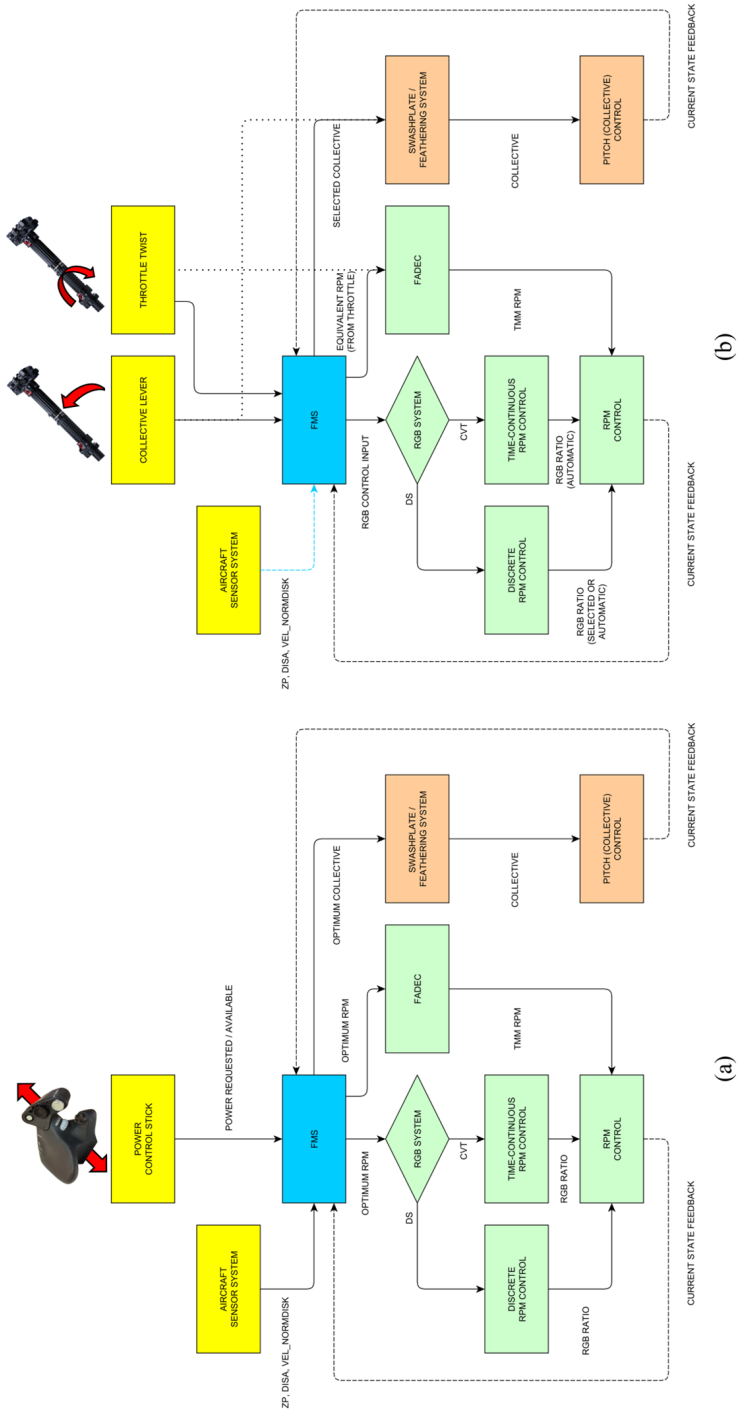

Fig. 53. Proposed optimized (a) and conventional (b) RPM and collective/feathering control systems

The RPM variations that the TMM might achieve are generally exceptionally reduced. For some engines, no variations would be allowed without sacrificing the thermodynamic efficiency or other design characteristics. The optimum operating point is defined such that the FM, i.e., the aerodynamic efficiency of the proprotor, is maximized for the given flight condition and pilot input. The flight condition is evaluated from the aircraft sensor system, such as the anemometric, barometric, and other angle measurement systems, such as the angular position of the proprotor-hub, cyclic angles, and aircraft angle of attack. The pilot input consists of a single Power Control Stick (PCS) interceptor, which demands a determined Power Requested/Available value, dependent on Power Available, at the actual flight condition.

Similar interceptor systems like the proposed PCS are already in operation, as in the case of the Bell V-22 Osprey. In this particular system, the pilot input is denominated as the Thrust Control Lever (TCL), which moves fore and aft, similar to a conventional airplane throttle, with a range of 4 inches. An image of this interceptor has been used for the PCS representation in Fig. 53. In the case of the XV-15 aircraft, a similar TCL was implemented in the last prototype versions. Once entering airplane mode, some pilots tended to pull up on the TCL when the nose was pitching down with the forward CG shift. This action caused acceleration because the pilot had not yet been familiarized with helicopter-to-airplane controls; however, they soon learned to move the stick aft to bring the nose up [54]. This movement type might seem counter-intuitive to helicopter pilots who are used to the rotation and vertical movement of the conventional collective lever cinematic.

Other control inputs are available in the TCL, such as a knurled rotary knob for controlling the rotor hub angle. It has not been disclosed how the V-22 Osprey TCL phases out the pilot input, trimming the powerplant and proprotor systems. For the XV-15, it has been stated that once fully converted to airplane mode, the TCL was a throttle only, and pulling it up increased thrust with all collective pitch control washed out [54]. For this reason, the proposed PCS system in this project might offer new alternatives to rotorcraft control systems by constructing the optimization procedure and by the control coupling of RPMs and collective/feathering angles.

5. Recommendations

As this project approaches the conclusion section, several recommendations for future research and refinement of the developed methodologies are drawn. The presented recommendations aim to enhance the comprehensiveness and applicability of the objectives and tasks treated in this project. The following recommendations outline the areas with the most relevant continuing research opportunities:

- To advance the applicability of the proprotor performance model, it is recommended to include non-axial flow components derived from the angle between the disk plane and V_∞. This becomes particularly relevant during transition phases in VTOLs, where the ability to account for non-axial flow can provide a more accurate representation of proprotor behavior. However, it is to be noted that up to incidence angles of 12-15º, no noticeable improvements in the proprotor performance modeling are expected to be found.
- Expanding the validation loops to encompass a broader range of proprotors' geometries is recommended. This would serve to verify the reliability and robustness of the proprotor performance tool across various geometrical configurations and operating regimes. Incorporating additional proprotors into the validation process would further enhance the tool's applicability and build confidence in its accuracy in architectures with not so accentuated pitch differences or greater RPMs.
- To achieve higher resolution results and thus soften undesired bumps in the performance results, it is suggested that the resolution be increased in the pre-computation sweep. This entails refining the sweep, especially regarding velocities, collective/feathering, and RPMs. Higher resolution in collective/feathering is especially recommended in the case of high-speed flight, higher resolution in the RPM sweep might be more recommended in the case of CVT transmission systems or electric powerplants, and the velocity sweep would generally be appropriate for any application.
- Future work should explore implementing a control system, such as a Total Energy Control System (TECS), to trim the elevator and thrust control for a given flight state or maneuver. This adaptive system would account for disturbances beyond the trim condition, facilitating altitude changes and accommodating variations in speed demand. Developing such a system, which might be approached from a trajectory optimization perspective, would cover the primary research and analysis sections of aircraft flight dynamics. Once this section is developed, further validation with in-house flight tests would become an attractive progression for the project.
- Including lateral dynamics in the flight dynamic model is recommended to provide a more comprehensive representation of the aircraft's behavior. Incorporating the lateral velocities, i.e., those on the Y-body axis, sideslip angles (β), and roll angles (ϕ), as well as their corresponding rates, would offer more complete aircraft performance modeling capabilities. Further input data would be necessary as the aerodynamic coefficients of the rudder and vertical stabilizer, as well as ailerons or flaperons, control surfaces. The values of the inertial tensor besides I_{YY} would be integrated into the dynamic model.

These recommendations aim to propel the project's findings into new realms of accuracy, versatility, and practical applicability, paving the way for advancements in proprotor performance modeling, control systems, and general flight dynamic modeling.

Conclusions

1. The allowance for the large inflow angles gives a steep improvement in the error margins between model and experimental results, with error margins of -3 to 4%, against the 20 to 88% of the small inflow angle approach. Thanks to this accuracy and precision improvement with respect to conventional modeling theories, the analytical-numerical Stahlhut solver can further be used in the development process of proprotors, especially those with great pitch changes throughout the blade span, leading to lower computational costs with respect to other approaches, such as FVM or CFD.
2. The results from the proprotor performance tool have been integrated into the developed longitudinal flight dynamic model fed by data frames of the aerodynamic coefficients of the main aerodynamic aircraft surfaces, a powerplant module, and a relatively simple geometrical definition of the aircraft. The results of the overall flight dynamics have led to error margins between 1.6 and 2.8% for the hovering scenarios and between 2.5 and 5.4% for the maximum speed scenarios. The OGE hovering modeled scenarios have been more challenging due to the proprotor wake interference and interaction with the wing.
3. The proposed control optimization system is able to find the combination of RPM and collective or feathering, which gives the highest aerodynamic efficiency, given by the FM, for a particular flight condition and power demand. This methodology alleviates the pilots' workload with respect to conventional helicopter cockpits in which throttle and collective levers are used by coupling these two into a single lever, denominated as the PCS or Power Control Stick. In the case of conventional propeller aircraft or some VTOL configurations, the pilot workload is not affected as the thrust or power control system is unchanged.
4. The performance capabilities of the optimized control system have been compared with the original flight test and performance charts of the Bell XV-15. When the system is configured to minimize the power required, improvements of approximately 7-8% and 5-8% have been achieved for the hovering and the maximum speed flight scenarios, respectively. On the other hand, once the system is configured to maximize the generated thrust at the original power required, an average payload increase of 220 kg and an average velocity increase of 5 m/s have been achieved for the hovering and the maximum speed flight scenarios, respectively.

List of references

1. Courtin C., Hansman R.J. Model Development for a Comparison of VTOL and STOL Electric Aircraft Using Geometric Programming. *AIAA Aviat 2019 Forum*. 2019;(June):1-18. doi:10.2514/6.2019-3477
2. Board D.S., Force T. Future Need for VTOL/STOL Aircraft. 2007;(July):155.
3. Darvishpoor S., Roshanian J., Raissi A., Hassanalian M. Configurations, flight mechanisms, and applications of unmanned aerial systems: A review. *Prog Aerosp Sci*. 2020;121(February):100694. doi:10.1016/j.paerosci.2020.100694
4. Zhou Y., Zhao H., Liu Y. An Evaluative Review of the VTOL Technologies for Unmanned and Manned Aerial Vehicles. *Comput Commun*. 2020;149(October 2019):356-369. doi:10.1016/j.comcom.2019.10.016
5. Trail S.B. Evaluation of V-22 Tiltrotor Handling Qualities in the Instrument Meteorological Environment. Published online 2006.
6. Padfield G.D. *Helicopter Flight Dynamics Including a Treatment of Tiltrotor Aircraft*. 3rd ed. Wiley; 2018.
7. P. Raymer D. *Aircraft Design: A Conceptual Approach*. Fifth Edit. AIAA Education Series; 2012. doi:https://doi.org/10.2514/4.869112
8. Droandi G., Gibertini G., Grassi D., Campanardi G., Liprino C. Proprotor–wing aerodynamic interaction in the first stages of conversion from helicopter to aeroplane mode. *Aerosp Sci Technol*. 2016;58:116-133. doi:10.1016/j.ast.2016.08.013
9. Ducard G.J.J., Allenspach M. Review of designs and flight control techniques of hybrid and convertible VTOL UAVs. *Aerosp Sci Technol*. 2021;118:107035. doi:10.1016/j.ast.2021.107035
10. Saeed A.S., Younes A.B., Islam S., Dias J., Seneviratne L., Cai G. A review on the platform design, dynamic modeling and control of hybrid UAVs. *2015 Int Conf Unmanned Aircr Syst ICUAS 2015*. 2015;(June):806-815. doi:10.1109/ICUAS.2015.7152365
11. Nathen P. Architectural performance assessment of an electric vertical take-off and landing (e-VTOL) aircraft based on a ducted vectored thrust concept. *Lilium*. Published online 2021:1-35.
12. PTERODYNAMICS. https://pterodynamics.com/
13. Maurya S., Gessow A. In Search of Extreme Limits of a Compound Helicopter in High Speed Flight In Search of Extreme Limits of a Compound Helicopter in High Speed Flight. 2021;(May). doi:10.4050/F-0077-2021-16763
14. Qiu Y., Li Y., Lang J., Wang Z. Dynamics Analysis and Control of Coaxial High-Speed Helicopter in Transition Flight. *Aerosp Sci Technol*. 2023;137:108278. doi:10.1016/j.ast.2023.108278
15. Wagter D., Hecke V., Tienen V., Horst V. Der., Hecke K.G. Van., Horst E. Van. Der.. Design, Control, and Visual Navigation of the DelftaCoper VTOL Tail-sitter UAV. Published online 2018. doi:10.1002/rob.21789
16. Zhong J., Wang C.. Transition characteristics for a small tail-sitter unmanned aerial vehicle. *Chinese J Aeronaut*. 2021;34(10):220-236. doi:10.1016/j.cja.2020.12.021
17. Airenthusiast. Upwardly Mobile Ryan X-13 Vertijet. *No 100*. Published online 2002.
18. Congressional Research Service. *F-35 Joint Strike Fighter (JSF) Program*.; 2022.

19. Ferguson S.W.. A Mathematical Model for Real Time Flight Simulation of a Generic Tilt-Proprotor Aircraft. *Nasa CR 166536*. Published online 1988:533.
20. Alli P., Nannoni F., Cicale M. ERICA: The European Tiltrotor. Design and Critical Technology Projects. In: *AIAA*. ; 2014. doi:https://doi.org/10.2514/6.2003-2515
21. Beaumier P., Decours J., Lefebvre T. Aerodynamic and Aero-acostuic Design of Modern Tilt-rotors: The ONERA Experience. *ICAS Secr - 26th Congr Int Counc Aeronaut Sci 2008, ICAS 2008*. 2008;4:1669-1679.
22. Airbus. Airbus lays the foundations for future urban air mobility in Germany with the Air Mobility Initiative. 2022;(May). https://www.airbus.com/en/newsroom/press-releases/2022-05-airbus-lays-the-foundations-for-future-urban-air-mobility-in
23. NATO. *Next Generation Rotorcraft Capability (NGRC)*.; 2022. www.nato.int/factsheets
24. European Commission. *Advanced Testbed for TILtrotor Aeroelastics*.; 2023. doi:10.3030/863418
25. Appleton W., Filippone A., Bojdo N. Interaction effects on the conversion corridor of tiltrotor aircraft. *Aeronaut J*. 2021;125(1294):2065-2086. doi:10.1017/aer.2021.33
26. Stahlhut C.W., Leishman J. G. *Aerodynamic Design Optimization of Proprotors for Convertible-Rotor Concepts*.; 2012.
27. Dekker H.N.J., Ragni D., Baars W.J., Scarano F., Tuinstra M. Aerodynamic Interactions of Side-by-Side Rotors in Ground Proximity. *AIAA J*. 2022;60(7):4267-4277. doi:10.2514/1.J061105
28. Boatto U., Bonnet P., Avallone F., Ragni D. Assessment of a BEMT-based rotor aerodynamic model under uniform aligned steady inflow. Published online 2023. doi:10.2514/6.2023-0609
29. Chen R., Yuan Y., Thomson D. A review of mathematical modeling techniques for advanced rotorcraft configurations. *Prog Aerosp Sci*. 2021;120(June 2020):100681. doi:10.1016/j.paerosci.2020.100681
30. Zawodny N.S., Pascioni K.A., Thurman C.S. An Overview of the Proprotor Performance Test in the 14 by 22 Foot Subsonic Tunnel. *FORUM 2023 - Vert Flight Soc 79th Annu Forum Technol Disp*. Published online 2023. doi:10.4050/f-0079-2023-18054
31. Sun Z., Feng L., Mao Y., et al. Investigation of Hydrodynamic Performance and Evolution of the near Wake on a Horizontal Axis Tidal Turbine. *Machines*. 2022;10(4):1-16. doi:10.3390/machines10040234
32. Martín-San-Román R., Benito-Cia P., Azcona-Armendáriz J., Cuerva-Tejero A. Validation of a free vortex filament wake module for the integrated simulation of multi-rotor wind turbines. *Renew Energy*. 2021;179:1706-1718. doi:10.1016/j.renene.2021.07.147
33. Suarez J.M., Doerffer P., Szulc O., Tejero F. Aerodynamic analysis of wind turbine rotor blades. *Task Q*. 2015;19(2):129-140. doi:10.17466/tq2015/19.2/g
34. Misté G.A., Benini E., Garavello A., Gonzalez-Alcoy M. A New Methodology for Determining the Optimal Rotational Speed of a Variable RPM Main RotorTurboshaft Engine System. *J Am Helicopter Soc*. 2015;60(3). doi:10.4050/JAHS.60.032009
35. Smith H.R. (2015). Engineering Models of Aircraft Propellers at Incidence. Published online 2015.
36. Garre W., Amri H., Pflumm T., et al. Helicopter Configurations and Drive Train Concepts for Optimal Variable Rotor-Speed Utilization. *Dtsch Luft- und Raumfahrtkongress*. 2016;49(0).

37. Gu N., Wang X., Lin F. Design of disturbance extended state observer (D-ESO)-based constrained full-state model predictive controller for the integrated turbo-shaft engine/rotor system. *Energies*. 2019;12(23):1-24. doi:10.3390/en12234496
38. EUROCOPTER. *Eurocopter EC145 UH-72 Lakota Helicopter Flight Manual*.; 2008.
39. Amri H., Feil R., Hajek M., Weigand M. Possibilities and difficulties for rotorcraft using variable transmission drive trains. *CEAS Aeronaut J*. 2016;7(2):333-344. doi:10.1007/s13272-016-0191-6
40. Garre W., Pflumm T., Hajek M. Enhanced Efficiency and Flight Envelope by Variable Main Rotor Speed for Different Helicopter Configurations. *42nd Eur Rotorcr Forum 2016*. 2016;1(July 2018):717-721.
41. Federal Aviation Administration (FAA). https://www.faa.gov/
42. Maisel M.D., Borgman DC, Few DD. *Tilt Rotor Research Aircraft Familiarization Document*.; 1975. http://hdl.handle.net/2060/19750016648
43. Ferguson S. *Development and Validation of a Simulation For Generic Tilt-Rotor Aircraft*.; 1989. https://rotorcraft.arc.nasa.gov/Publications/files/CR-166537_883.pdf
44. Churchill G.B., Dugan DC. Simulation of the XV-15 Tilt Rotor Research Aircraft. Published online 1982.
45. Maisel M.D., Giulianetti DJ, Dugan DC. The History of The XV-15 Tilt Rotor Research Aircraft: From Concept to Flight. *NASA Spec Publ 4517*. 2000;(May):194.
46. Jordon D.E., Patterson W, Sandlin DR. *An Experimental and Analytical Method for Approximate Determination of the Tilt Rotor Research Aircraft Rotor Wing Download*.
47. Diaz S., Mouterde E., Desopper A. Performance code for take-off and landing tilt-rotor procedures study. *30th Eur Rotorcr Forum*. 2005;2005:699-711.
48. Drela M. XFOIL: An Analysis and Design System for Low Reynolds Number Airfoils. In: *Conference on Low Reynolds Number Airfoil Aerodynamics, University of Notre Dame*. ; 1989. doi:10.1007/978-3-642-84010-4_1
49. Zhong W., Shen W.Z., Wang T., Li Y. A tip loss correction model for wind turbine aerodynamic performance prediction. *Renew Energy*. 2020;147:223-238. doi:10.1016/j.renene.2019.08.125
50. Peter B. S. Lissaman P.D. Wind turbine airfoils and rotor wakes. In: *Wind Turbine Technology: Fundamental Concepts in Wind Turbine Engineering, Second Edition*. ; 2009. doi:https://doi.org/10.1115/1.802601
51. Tangier J.L., Selig M.S. An Evaluation of an Empirical Model for Stall Delay Due to Rotation for HAWTs. *Nrel/Cp-440-23258*. 1997;(July):1-12.
52. Felker F.F., Young L.A., Signor D.B. *Performance and Loads Data from a Hover Test of a Full-Scale XV-15 Rotor*.; 1986.
53. Saias C.A., Goulos I., Roumeliotis I., Pachidis V. Preliminary Design of Hybrid-Electric Propulsion Systems for Emerging Urban Air Mobility Rotorcraft Architectures. *J Eng Gas Turbines Power 143*. Published online 2021. doi:10.1115/1.4052057
54. Dugan D. A Survey of Thrust Control Inceptors for VTOL Aircraft. *Ames Res Cent*. Published online 2017. http://www.sti.nasa.gov

Appendices

Appendix 1. Extended proprotor aerodynamic and performance coefficients results

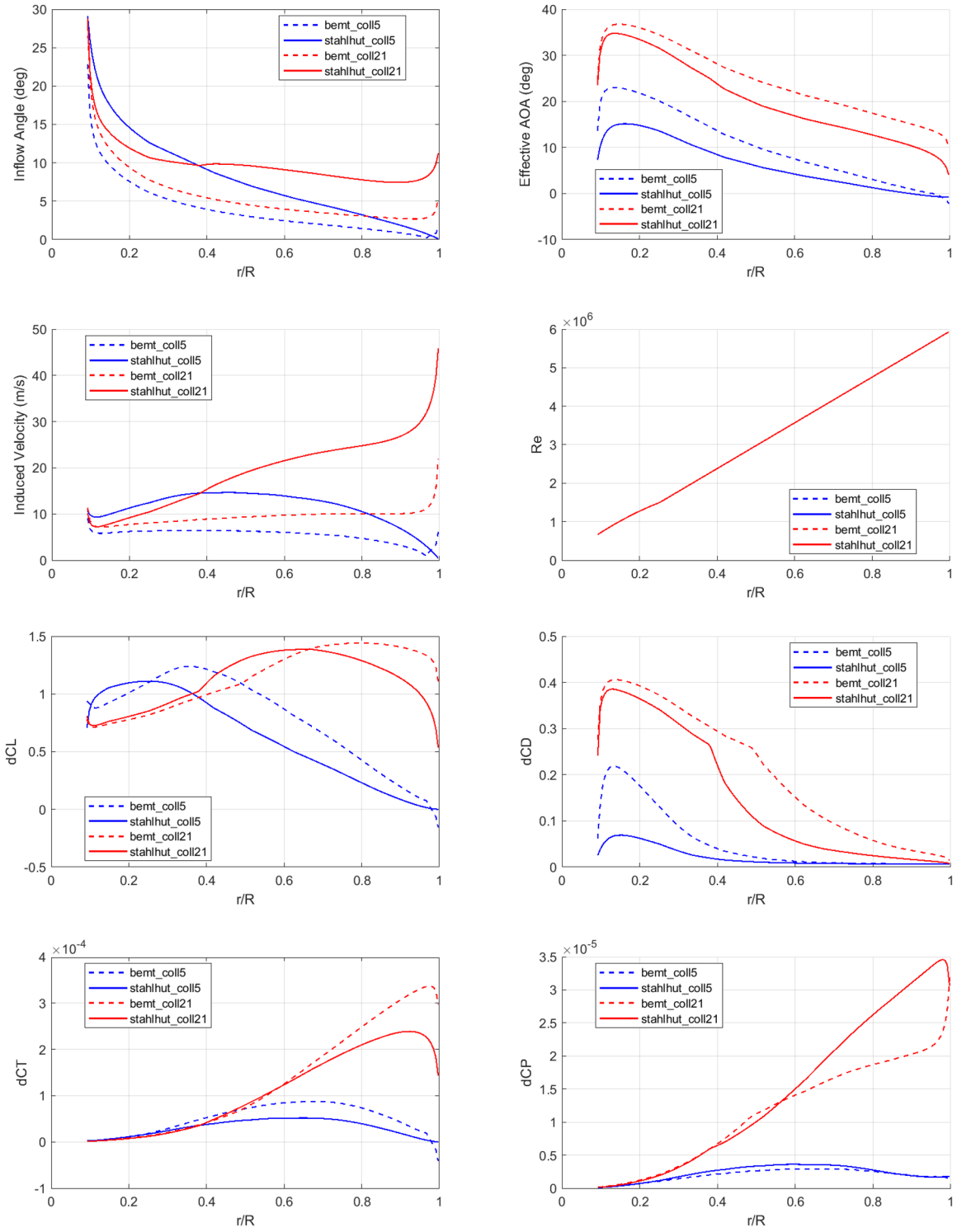

Fig. 54. Aerodynamic and performance coefficients comparison throughout the blade span